

**ELECTROMAGNETIC SIMULATION OF PARALLEL TRANSMIT
RADIOFREQUENCY COILS AND HIGH PERMITTIVITY MATERIALS
USING CIRCUIT-SPATIAL OPTIMIZATION WITH VIRTUAL
OBSERVATION POINTS**

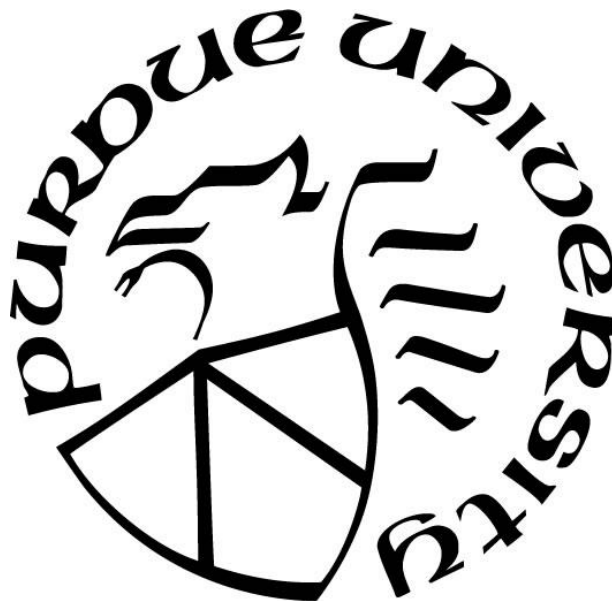
by
Xin (Jack) Li

A Dissertation

Submitted to the Faculty of Purdue University

In Partial Fulfillment of the Requirements for the degree of

Doctor of Philosophy



Weldon School of Biomedical Engineering

West Lafayette, Indiana

August 2020

THE PURDUE UNIVERSITY GRADUATE SCHOOL
STATEMENT OF COMMITTEE APPROVAL

Dr. Joseph V Rispoli, Chair

Weldon School of Biomedical Engineering

Dr. Jullie W Pan

Department of Radiology, University of Pittsburgh

Dr. Jiao Dan

School of Electrical and Computer Engineering

Dr. Thomas Talavage

Weldon School of Biomedical Engineering

Dr. John Nyenhuis

School of Electrical and Computer Engineering

Approved by:

Dr. George R. Wodicka

TABLE OF CONTENTS

TABLE OF CONTENTS.....	3
LIST OF FIGURES	6
LIST OF TABLES	11
LIST OF ABBREVIATIONS.....	12
ABSTRACT.....	13
1. INTRODUCTION	14
2. EM SIMULATION OF LOOP COILS AND BENCH MEASUREMENT.....	17
2.1 The effects of matching and tuning on loop coil currents in FDTD simulation	17
2.1.1 Simulation of a loop coil.....	17
Coil tuning approaches.....	19
Coil matching approaches	19
Tuning and matching.....	20
2.1.2 Matching and tuning effect on the coil currents and RF efficiency	21
Coil currents	21
The transmit efficiency.....	24
Conclusion.....	25
2.2 A comparison of FDTD and FEM solvers for simulating a surface loop coil with tissue phantom.....	26
2.2.1 Background of HFSS and XFDTD.....	27
2.2.2 Comparison of E and B fields.....	27
2.3 Bench measurement of S parameters of two loop coils.....	29
2.3.1 Measuring coil input impedance.....	30
2.3.2 Circuit simulation of the RID decoupling	31
3. SIMULATION OF HETEROGENEOUS BREAST MODELS IN RF EXPOSURE	33
3.1 Background.....	33
3.1.1 Breast MRI.....	33
3.1.2 SAR measuring and simulation	34
3.2 Breast Modeling.....	36
3.2.1 Model Fusion Algorithm	37

Morphological Filtering	37
Affine transformation	37
Level set method of mean curvature motion	37
Implementation.....	38
3.3 Electromagnetic and thermal simulations	39
3.3.1 Breast RF coil modeling	39
3.3.2 Simulation parameters	42
3.3.3 SAR calculation	42
3.3.4 Thermal simulation	43
3.4 EM simulation results	43
3.4.1 Modeled breast fused on human models	43
3.4.2 SAR and temperature rise in breast	45
3.4.3 Power deposition in various tissue	49
3.4.4 FGT % increases SAR and temperature rise	51
3.5 Role of FGT % and various tissue on SAR and temperature	55
3.5.1 FGT % increase SAR level.....	55
3.5.2 Maximum tissue temperature rise.....	56
3.5.3 Additional considerations on breast morphology	56
4. EM SIMULATION OF A 16-CHANNEL HEAD TRANSCEIVER AT 7 T USING CIRCUIT-SPATIAL OPTIMIZATION	58
4.1 Method	59
4.1.1 Simulation set-up	59
4.1.2 S-parameters relationship	62
4.1.3 Decoupling circuits	65
4.1.4 Optimization	66
ADMM Optimization implementation.....	68
4.1.5 Reconstruction of B_1^+ profiles and RF shimming	70
4.2 Results.....	72
4.2.1 Defining the fixed transceiver T_0	72
4.2.2 Simulated and experimental B_1^+ maps	73
4.2.3 With and without a homogeneity cost function	79

4.3	Discussion	79
4.3.1	Co-simulation and S-parameters optimization	79
4.3.2	Cost function: hybrid circuit-spatial domain optimization	80
4.3.3	Simulating the transceiver and experimental B_1^+ maps	80
4.3.4	Additional considerations	83
4.4	Conclusions	83
5.	VIRTUAL OBSERVATION POINTS AND HIGH PERMITTIVITY MATERIAL	85
5.1	Local SAR and VOP:	85
5.1.1	10-gram averaged Q matrices	86
5.1.2	Worst-case SAR	87
5.1.3	VOP compression	88
5.1.4	The compression method	88
5.1.5	VOP on human heads	90
5.2	HPM head former enhancing coil performance	93
5.2.1	HPM head former with single coil	93
5.2.2	HPM head former with simultaneous transmission	94
5.2.3	VOP on human heads with HPM head former	99
	APPENDIX A. S-MATRICES CALCULATION	101
	APPENDIX B. BREAST MODEL	106
	REFERENCES	118

LIST OF FIGURES

Figure 2-1. The balanced L-network (a) is made by an inductor of 19.2 nH and two 18.8 pF capacitors. The unbalanced L-network (b) is made by an inductor of 19.2 nH and one 9.4 pF capacitor. (c) For the loop coil with 12 gaps, the current source is inserted in the feed.....	18
Figure 2-2. The S_{11} evaluated at the feed gap plotted in the Smith chart. (a) This coil is not well tuned and the 298 MHz point is off the horizontal line ($x = 0$) in the Smith chart. (b) This coil is well tuned and the 298 MHz point is on the horizontal line ($x = 0$).	20
Figure 2-3. The magnitude of S_{11} is plotted against the frequency. (a) The S_{11} plot using the balanced L-network or the unbalanced L-network. (b) The S_{11} plot when the capacitor (C2) in the unbalanced L-network is increased from 9.4 pF to 16.3 pF.	21
Figure 2-4. The current distributions in the 12 lumped elements of the coil, plotted from 290 MHz to 308 MHz. The current source is 1 A and 50 Ω for all cases. The first row from the top is the tuned but unmatched loop coil and its current magnitude distribution within the lumped elements (a) and the phase distributions (b) . The middle row is the coil tuned and matched with the balanced L network, and the current magnitude distribution shows in (c) , and the phase distribution shows in (d) . The bottom row is the coil tuned and matched with the balanced L-network, and (e) is the current magnitude distribution; (f) is the current phase distribution.	22
Figure 2-5. Transmit efficiency and phase maps in the sagittal plane (YZ plane) within the slab phantom. The first row illustrates the (a) transmit efficiency ($\mu T/W$) and (b) B_I^+ phase map of the tuned, not matched coil. The second row shows (c) the percentage ratio of transmit efficiency of the tuned, not matched coil to the transmit efficiency of (a) , and (d) the phase map. The third row similarly shows (e) the difference ratio and (f) the phase map for the coil tuned and matched with the balanced L-network. The fourth row shows the (g) difference ratio and (h) the phase map for the coil tuned and matched with unbalanced L-network. The fifth row shows (i) the difference ratio and (j) the phase map for the coil tuned, but not well matched.....	25
Figure 2-6. Simulation setup of a surface loop coil over a tissue phantom.	26
Figure 2-7. Meshed coil and phantom in XFDTD and HFSS.....	27
Figure 2-8. E and B_I^+ field strength in a cross section of the muscle slab.	28
Figure 2-9. E and B_I^+ field strength in a cross section of the fat slab.	29
Figure 2-10. Bench Measurement of two coils decoupled by Resonant inductive decoupling (RID) (A) , the S_{12} coefficient without RID (B) , and S_{12} coefficient with RID (C)	30
Figure 2-11. Input Impedance plotted in a Smith chart (Auto wave 50 - 650 MHz) for XFDTD (A) and Network Analyzer (B)	31
Figure 2-12. A: circuit simulation of the two coils shown in Figure 2-10. B: S parameter plots of the two coils (the top row is with RID, the bottom row is without RID).	32
Figure 3-1. B_I^+ spatial profile of a loaded breast coil in the sagittal (a) , coronal (b) , and axial (c) planes. The coil-encompassed volume accessible by the subject, with 1-cm spacing to adjacent	

coil boundary, is outlined by the black dashed line; this volume is defined as the coil effective volume and used for averaging B_1^+ . Breast and chest are outlined by the red long-dashed line. Local discontinuity of B_1^+ appears at the skin-to-air boundary. **(d)** Right breast of prone position Ella model is positioned inside breast coil for unilateral RF excitation, with the coil boundaries at least 1 cm to skin..... 41

Figure 3-2. Bilateral breasts (0.5 mm resolution) fused to whole-body models. Sagittal **(a)** and axial **(b)** view of bilateral breasts fused to Ella (0.5 mm resolution); **(c,d)** the same set of bilateral breasts are fused to Hanako (2 mm resolution). The modified breast models are assigned a higher meshing priority and consequently overwrite the chest region of the whole-body models. Tissue added by the level-set method is designated Level-set subcutaneous adipose tissue (SAT) and colored blue..... 44

Figure 3-3. Sagittal plots of raw SAR and temperature rise with four BI-RADS-categorized breasts fused to Ella **(A)** and Hanako **(B)**. Raw SAR and temperature rise when tissue temperature reaches the steady-state are quantified at mean $B_1^+ = 1.5 \mu\text{T}$ within breast tissue at 7 T. Each row represents a simulation case of one BI-RADS category, and corresponding FGT% is reported. All plots are taken from the sagittal plane across the coil center in a field of view of 22 cm (height) by 19 cm (width). Raw SAR 0 dB = 1.3 W/kg..... 46

Figure 3-4. Sagittal plots of raw SAR, 10-g averaged SAR, and temperature rise with the same set of bilateral breasts, but of different voxel resolution, fused to Ella and Hanako. SAR and temperature rise when tissue temperature reaches the steady-state are quantified at mean $B_1^+ = 1.5 \mu\text{T}$ within breast tissue at 7 T. Both the top and bottom rows include breast models with 0.5-mm resolution, while the middle row includes the same breast models at 2-mm resolution. This breast was categorized as BI-RADS d, and the FGT% is 47.6 for Ella and 50.4 for Hanako. All plots are taken from the sagittal plane across the coil center in the same field of view of 22 cm (height) by 19 cm (width). SAR 0 dB = 1.3 W/kg. Internal air in the large intestine of Hanako results in the blank internal regions of raw SAR..... 48

Figure 3-5. Mean power deposition percentage in tissues with the same net power dissipated under RF exposure in Ella (top) and Hanako (bottom). The same sample size of 0.5-mm and 2-mm resolution breasts are plotted in the bottom bar graph. Error bars demonstrate data distributed within one standard deviation. 50

Figure 3-6. Plots illustrating correlations between FGT%, SAR, and temperature rise for Ella and Hanako breasts. Top plot shows the maximum 10-g averaged SAR values versus FGT%. Middle plot shows the partial body SAR versus FGT%. Bottom plot shows maximum local tissue temperature rise (at steady state) versus maximum 10-g averaged SAR values. All breast phantoms are in 0.5-mm resolution. Linear regression is used to fit Ella and Hanako breasts data separately; the blue regression line is for Ella, and the black line is for Hanako. The R^2 values for 10-g averaged SAR as a function of FGT%, partial body SAR as a function of FGT%, and temperature rise as a function of 10-g averaged SAR are 0.61, 0.70, and 0.49 for Ella, and 0.63, 0.86, and 0.85 for Hanako, respectively. All breast models are color-labeled according to their BI-RADS category. 53

Figure 4-1. **A:** The coil set up. A slotted RF shield is placed outside the array coil. The dual-row coil is made with a former and covered with copper clad board. The simulated human models are positioned in the coil center, with the eyes aligned with the eye portals on the coil former,

mimicking the real scanning scenario. **B**: The 1-V, 50- Ω voltage feeds orientations in the XFDTD setup for the 208×208 S-parameters calculation. The arrow points to the current flowing direction. The circuit diagrams of the top and bottom row loop coils are shown in **C**. The RID and TD circuits are shown in **D**. There are 16 RID circuits applied to decouple neighboring coils in the horizontal direction, 8 vertical TD circuits applied to decouple neighboring coils in the vertical direction, and 16 diagonal TD circuits applied to decouple neighboring coils in the diagonal direction. 61

Figure 4-2. The 208-port coil as a network system. The 16 channels coming from the splitter are connected to matching circuits which are connected to the dual-row coil. The dual-row coil elements are also connected with lumped capacitors and transformers decoupling circuits. 63

Figure 4-3. Magnitude (dB) and phase of S-parameter matrix at 298 MHz, and frequency sweep determined from cost function Eq. 4-11 (with B_I^+ homogeneity optimization) for Duke (**A**), Ella (**B**), Hanako (**C**), and Louis (**D**). Panel **E** shows these equivalent data for Louis but determined with Eq. 4-15, without B_I^+ homogeneity optimization. 67

Figure 4-4. **A**: Four optimization solvers, with the objective function evaluations plotted with normalized iterations. The SAMO optimization took 11 hours to converge. **B**: The ADMM solver is able to converge when the difference between vector x and v becomes negligible. 70

Figure 4-5. **A**: B_I^+ field magnitude for 16 channels, and each coil is fed with 65.5 V forward voltage. The field maps are taken in the axial plane at the center of each surface coil. The channel index is labeled in Figure 4-1-B. **B**: The standard deviation over mean (B_I^+ inhomogeneity) over the inter-row coil phase shift from 0 to 80°. 71

Figure 4-6. B_I^+ phase and magnitude profiles of eight channels on five axial slices (**A-E**) evenly spaced across the simulated and in vivo heads. Within the same row, from left to right order, are the simulated magnitude, in vivo magnitude, simulated phase, and in vivo phase. The phase map of each channel is relative to the 1st channel. In both simulation and experiment, each coil is fed with 65.5 V forward voltage. 74

Figure 4-7. **A**: The sagittal B_I^+ profiles of the RF shimmed homogeneous distributions for Ella (top left), Louis (top right), Hanako (bottom left), and Duke (bottom right). The nine ROI slices indicated with dashed red lines are evenly spaced across the head, and the axial views are shown in Supporting Figure A-2 for four simulation heads. **B**: The corresponding coronal B_I^+ profiles for the four head models. 78

Figure 4-8. **A**: The RF shimmed B_I^+ profiles of in vivo scan compared with one simulation head. **B**: The tissue contrast image of simulated head (contrast provided solely based on tissue conductivity). 82

Figure 5-1. the magnitude map of the $Q_{3,4}$ element of the Q matrix. **A**: the axial view before and after the 10-gram average. **B**: the sagittal view before and after the 10-gram average. 86

Figure 5-2. the phase map of the $Q_{3,4}$ element of the Q matrix. **A**: the axial view before and after the 10-gram average. **B**: the sagittal view before and after the 10-gram average. 87

Figure 5-3. **A**: The VOP locations on the worst-case local SAR (10g-SAR) maps in sagittal views within the heads of realistic human models: of Ella, Hanako, Duke, Louis head in coil center, Louis head posterior shift, and Louis head superior shift. The SAR scale bar (0 – 1000 W/kg) are based

on $\|U\| = 1$. **B**: 2000 random RF excitations were used to validate the VOP matrix with the uncompressed Q matrix at 5% over-estimation rate for heads in **A**. The maximum local SAR for both cases at all 2000 random RF excitations is plotted. 91

Figure 5-4. Louis VOP core matrices locations on the worst-case SAR map, for $\epsilon = 5\%$ and 10% ; and Duke VOP core matrixes for $\epsilon = 10\%$. Bottom row figures are the sagittal view of head tissue contrast maps, pTx coil former and RF shield. 92

Figure 5-5. RF efficiency in the head when single port of the coil is activated when a 5-mm thickness HPM head former (green) covers the upper head. The RF efficiency increased as the relative permittivity increased. 94

Figure 5-6. Comparisons of direct simulation and circuit-domain co-simulation. **A**: the S parameters for single coil activation, calculated separately using the circuit-domain co-simulation (left column) and direct XFDTD simulation (right column). **B**: the B_I^+ magnitude and phase map for single coil activation. 95

Figure 5-7. Head former with simultaneous transmission. **A**: the sagittal view and 3D view of the HPM head former, head tissue and coil structure. **B**: The B_I^+ statistics (mean, standard deviation, power, and RF efficiency) in the brain tissue for various ϵ_r of the HPM head former. 96

Figure 5-8. The S-parameters of the 16 channels head coil wearing HPM head former at various ϵ_r 97

Figure 5-9. The sagittal view (top row) and coronal views (bottom row) of the Louis head when wearing HPM head former ($\epsilon_r = 120$) in **A**, and not wearing the HPM head former in **B**. 98

Figure 5-10. The locations of VOP cluster core matrices on the worst-case SAR map for Louis without HPM head former (**A**) and wearing HPM head former (**B**). The sagittal view of head tissue and coil structure without HPM is in **C**, and with HPM is in **D**. 99

Figure A-1. Comparison of co-simulation with direct XFDTD simulation. The voltage feed for the direct simulation is 150 V, 50Ω at 90° phase shift; and the a_{in} for the co-simulation is 75 V; this value is $V_+ = V_L / (1 + S_{11})$, where V_L is the load voltage and S_{11} is the reflection coefficient seen at the voltage feed in the direct simulation. **A** displays the S-parameters of one channel (S_{ii} red, S_{ij} blue), and **B** shows the corresponding E_x and B_I^+ phase and magnitude maps. 104

Figure A-2. The ROI selections for the Homogeneous distribution. The ROIs are overlaid on the head in the axial view. 105

Figure B-1. Sagittal plots of raw SAR in 7 T at mean $B_I^+ = 1.5 \mu T$ within breast tissue for 0.5-mm resolution breast models derived from the BI-RADS categorized CT (triangles) and MRI (squares) images fused with Ella (stars) and Hanako (diamonds). The same breast models from Ella (upper row) are down-sampled to fuse with Hanako (lower row). The FGT%, in ascending order, is quantified below the marker lines. The FGT% values on the left and right side of the forward slash correspond to Ella and Hanako breasts, respectively. Raw SAR of 0 dB = 1.3 W/kg. All images are taken from the axial plane across the coil center in the same field of view. The blank raw SAR in the Hanako model corresponds to internal air in the large intestine. 106

Figure B-2. Sagittal plots of 10-g averaged SAR in 7 T at mean $B_I^+ = 1.5 \mu T$ within breast tissue for 0.5-mm resolution breast models derived from the BI-RADS categorized CT (triangles) and

MRI (squares) images fused with Ella (stars) and Hanako (diamonds). The same breast models from Ella (upper row) are down-sampled to fuse with Hanako (lower row). The FGT%, in ascending order, is quantified below the marker lines. The FGT% values on the left and right side of the forward slash correspond to Ella and Hanako breasts, respectively. 10-g SAR of 0 dB = 1.3 W/kg. All images are taken from the axial plane across the coil center in the same field of view. 108

Figure B-3. Sagittal plots of temperature rise when tissue temperature reaches the steady-state in 7 T at mean $B_1^+ = 1.5 \mu\text{T}$ within tissue for 0.5-mm resolution breast models derived from the BI-RADS-categorized CT (triangles) and MRI (squares) images fused with Ella (stars) and Hanako (diamonds). The same breast models from Ella (upper row) are down-sampled to fuse with Hanako (lower row). The FGT%, in ascending order, is quantified below the marker lines. The FGT% values on the left and right of the forward slash correspond to Ella and Hanako breasts, respectively. All images are taken from the sagittal plane across the coil center in the same field of view. .. 110

Figure B-4. Axial plots of raw SAR in 7 T at mean $B_1^+ = 1.5 \mu\text{T}$ within breast tissue for 0.5-mm resolution breast models derived from the BI-RADS categorized CT (triangles) and MRI (squares) images fused with Ella (stars) and Hanako (diamonds). The same breast models from Ella (upper row) are down-sampled to fuse with Hanako (lower row). The FGT%, in ascending order, is quantified below the marker lines. The FGT% values on the left and right side of the forward slash correspond to Ella and Hanako breasts, respectively. Raw SAR of 0 dB = 1.3 W/kg. All images are taken from the axial plane across the coil center in the same field of view..... 112

Figure B-5. Axial plots of 10-g averaged SAR in 7 T at mean $B_1^+ = 1.5 \mu\text{T}$ within breast tissue for 0.5-mm resolution breast models derived from the BI-RADS categorized CT (triangles) and MRI (squares) images fused with Ella (stars) and Hanako (diamonds). The same breast models from Ella (upper row) are down-sampled to fuse with Hanako (lower row). The FGT%, in ascending order, is quantified below the marker lines. The FGT% values on the left and right side of the forward slash correspond to Ella and Hanako breasts, respectively. 10-g SAR of 0 dB = 1.3 W/kg. All images are taken from the axial plane across the coil center in the same field of view. 114

Figure B-6. Axial plots of temperature rise when tissue temperature reaches the steady-state in 7 T at mean $B_1^+ = 1.5 \mu\text{T}$ within tissue for 0.5-mm resolution breast models derived from the BI-RADS categorized CT (triangles) and MRI (squares) images fused with Ella (stars) and Hanako (diamonds). The same breast models from Ella (upper row) are down-sampled to fuse with Hanako (lower row). The FGT%, in ascending order, is quantified below the marker lines. The FGT% values on the left and right side of the forward slash correspond to Ella and Hanako breasts, respectively. All images are taken from the axial plane across the coil center in the same field of view..... 116

LIST OF TABLES

Table 3-1. Attributes of Selected Adult Female Whole-Body Voxel Models.....	35
Table 3-2. Transmit efficiency for each breast phantom simulation case	52
Table 4-1. Mean \pm standard deviation of key components of the 296 optimized parameters.	62
Table 4-2. The mean and standard deviations of B_I^+ in the intracerebral tissue, and the total peak forward power of RF amplifier for homogeneous distribution. (A) Including homogeneity weighting (Eq. 4-11), (B) excluding homogeneity weighting (Eq. 4-17). (A, B) perform the transceiver T optimization individually over the four models, optimizing full set of parameter x. (C) Using the fixed transceiver T_0 as determined from the homogeneity weighted optimization.	76
Table 5-1. VOP matrices comparison for Louis and Duke.....	93
Table 5-2. The VOP matrices and worst-case SAR for Louis without and with HPM.	100

LIST OF ABBREVIATIONS

Abbreviation	Full description
B_I^+	Transmit magnetic field
BI-RADS	Breast Imaging, Reporting & Data System
DC	Decoupling circuit
EM	Electromagnetic
FGT	Fibroglandular tissue
FGT%	Fibroglandular tissue percentage
FDTD	Finite difference time domain
FEM	Finite element method
HPM	High permittivity material
pTx	Parallel transmission
RID	Resonant Inductive Decoupling
RF	Radiofrequency
SNR	Signal-to-noise ratio
S matrix	Scattering matrix
S-matrices	Spatial matrices
S-parameter	Scattering parameters
Std	Standard deviation
SAR	Specific Absorption Rate
TD	Transformer decoupling
VOP	Virtual Observation Points
ϵ_r	Relative permittivity
σ	Conductivity

ABSTRACT

The recent FDA regulatory clearance for the 7 tesla Magnetic Resonance Imaging (MRI) system has led to increased interest in clinical ultra-high field (UHF) applications. However, to robustly achieve the expected increase in signal-to-noise ratio (SNR) at UHF, the radiofrequency (RF) challenges need to be met, namely, problems with higher RF power, worse B_1^+ inhomogeneity (signal voids) and increased tissue dielectric properties at higher frequency, all of which usually results in increased specific absorption rate (SAR). The parallel transmission (pTx) techniques are generally accepted as a realistic solution, providing improvement in the B_1^+ homogeneity with good RF efficiency while reducing peak local SAR. We designed a hybrid circuit-spatial domain optimization to accelerate the design of a double row pTx head coil. The method predicted consistent coil scattering parameters, component values and B_1^+ field. RF shimming of the calculated field maps matched in vivo performance. To further increase the B_1^+ homogeneity in tissue, we added high dielectric material (HPM) pads near the coil, as the displacement currents in the HPM induced secondary B_1^+ in tissue. This raises a RF safety question of how to monitor millions of local SAR (complex valued Q-matrix) in the tissue voxels, for any weightings (forward voltages) applied to the pTx system. We implemented VOPs based on singular value decomposition to compress the Q-matrices with a compression ratio >100 , effectively monitoring the maximum peak local SAR values at given weighting amplitudes.

1. INTRODUCTION

There are around 60 ultra-high field human magnetic resonance imaging (MRI) scanners installed worldwide, with static magnetic field strengths of 7 to 12 tesla (1). At present, the highest resolution for brain imaging at 7T is about 200 μm . In the near future, ultra-high field MRI is expected to improve the resolution of in vivo imaging to less than 100 μm with 14 tesla scanners, and this will largely enhance human brain structure and functional research. For example, the specificity, sensitivity, and contrast of blood oxygenation level dependent (BOLD) signal from the human visual cortex using an echo planar imaging (EPI) sequence at 7 tesla is improved compared to 4 tesla, because the shorter T_2^* in cortex can be approached at high static B_0 field (2). However, in ultra-high magnetic field, the radiofrequency (RF) magnetic field B_1 wavelengths in tissue are reduced to 9 cm, which causes destructive interference and leads to inhomogeneity in the B_1 field (3,4). From a hardware perspective, to move beyond 12 tesla brain scanning, efforts are necessary to develop better superconductors that can carry supercurrents for high field, gradient coils that can operate at high gradient strength, high-order spatial B_0 shim coils, and transmit/receive coil arrays that minimize the specific absorption rate (SAR) at ultra-high field strengths. Loop coils are fundamental to most RF coil designs used for MRI, including parallel array coils. The desired configuration of loop coils can be explored through computational modeling, such as full-wave electromagnetic (EM) simulation. While EM simulation is a powerful tool for refining a coil design, it is also the basis for ensuring transmit coils meets safety requirements, presently controlled by limits on SAR (5,6). The frequency tuning makes the coil resonant at the Larmor frequency and provides uniform current in magnitude and phase around the loop. Impedance matching provides the minimum reflection loss and delivers the maximum power possible to the resonant coil. Both tuning and matching are instrumental for the physical operation of transmit RF coils, but their role in coil modeling is not as well established. We will discuss EM simulation of loop coil using standard matching and tuning procedures in Chapter 2.

The application of EM simulations using realistic breast models to facilitate breast MRI imaging will be discussed in Chapter 3. Breast cancer is the most diagnosed cancer and leads to the highest death rate among women in the United States. In 2016, roughly 246,660 new incidences of breast cancer were diagnosed, corresponding to 29% of all new cancer cases, while breast cancer caused 40,450 deaths, equaling 14% of all cancers deaths (7). Compared to other imaging

modalities, MRI offers high sensitivity for breast cancer detection (8,9) and is commonly indicated for screening high-risk subjects, e.g., women with familial history, genetic predisposition, significant chest radiation history, or lobular cancer (10–13). Furthermore, owing to superior contrast between tumor and fibroglandular tissue, MRI has been reported to improve sensitivity within dense breasts (14,15), i.e., those clinically classified as heterogeneous or extreme fibroglandular tissue according to the American College of Radiology Breast Imaging Reporting and Data System (BI-RADS) Atlas (16). The increased signal-to-noise ratio at 7 T enhances both temporal and spatial resolutions of dynamic contrast-enhanced breast MRI, thus improving sensitivity; the diagnostic specificity of breast MRI may be extended by using supplementary techniques including diffusion-weighted MRI and magnetic resonance spectroscopy, which also have improved performance at 7 T (17–19). However, RF power deposition—quantified with respect to tissue mass as SAR—must be well characterized, particularly at high fields. Both the U.S. Food and Drug Administration (FDA) and the International Electrotechnical Commission (IEC) include SAR as a criterion for assessing significant risk in MRI devices (20,21). The IEC60601-2-33 standard specifies SAR limits and temperature limits at normal operating mode and first-level controlled operating modes, while second-level controlled operating mode requires SAR limits be specifically approved by an appropriate investigational review board. For a volume transmit coil at normal operating mode, the partial body SAR limit is 2-10 W/kg (determined by the ratio of exposed patient mass to patient mass), and the maximum local temperature limit is 39 °C. For a local transmit coil at normal operating mode, the local SAR (10-g averaged SAR) limit is 10 W/kg for trunk and 20 W/kg for extremities, and temperature constraints are the same as for a volume transmit coil.

The parallel transmission (pTx) coils, made by individually voltage-driving loops, are generally accepted as a realistic solution (5,22–25), providing improvement in the B_1^+ spatial homogeneity with good RF efficiency while reducing peak local SAR (26,27). In the development of such pTx coils, the need for accurate EM simulations for RF safety and performance design is evident. Over the past several years, the state-of-the-art for design and simulation of such coil arrays has advanced, e.g., Kozlov and Turner (28) described the circuit-domain co-simulation strategy to use the S-parameters from a single EM simulation with RF circuit analysis for coil tuning and matching thereby saving significant time. More specifically, Zhang (29) and Lemdiasov (30) described calculation of a closed-form S-parameter matrix to accomplish these simulations.

These methods have been used to improve the prediction of local SAR in pTx coils (26,31) at 3 T, 7 T (32) and 10.5 T (33). We will discuss the EM simulation of a pTx head coil at 7T using a novel co-simulation method in Chapter 4.

Monitoring the global SAR is important for multi-channel transceivers that are tailored via RF shimming to increase RF homogeneity over regions of interest (ROIs). To meet the IEC (International Electrotechnical Commission) standards, the VOPs (Virtual Observation Points) compress the local SAR matrices (10-g average Q matrices) to a smaller set of data that ensures all the local SAR values are upper bounded by the IEC local SAR limits. The ability to generate differing transmit RF distributions is an important aspect of multi-coil arrays. At ultra-high field, such distributions have been developed for RF-based selective regional excitation (5), which has been particularly relevant for MR spectroscopic imaging and the needed suppression of extracranial signal. Relatively small set of VOPs are used to upper bound the 10-g Q matrices to compliance with the IEC local SAR limits. The upper bound is the VOP matrices' magnitude, and it is controlled by user-input overestimation rate. In Chapter 5, we will show the effectiveness of VOPs implemented with different human models and user-input overestimation. In addition, we will investigate the VOP loci spatial locations relative to the local SAR distribution. High permittivity materials (HPM) have high relative permittivity ($\epsilon_r > 100$) and have been shown in applications of human body or head imaging to increase the RF efficiency when used in combination with single loop or birdcage RF coils (34–36). The HPM applications in pTx coil usage is rare, and the S parameters and VOPs of HPM are not well studied. In Chapter 5, we present an EM simulation study of the pTx coil performance on human model wearing a HPM head former.

2. EM SIMULATION OF LOOP COILS AND BENCH MEASUREMENT

2.1 The effects of matching and tuning on loop coil currents in FDTD simulation

In coil simulations, matching is often considered a tedious effort and deemed unnecessary (37). Normally the physical matching circuit is boxed or placed orthogonal to the coil planar surface, and its EM coupling with the coil can be neglected (38). In this study we find the matching circuit can affect the current's phase and magnitude in the coil, and a well-matched coil can also increase the spatial focus of transmit efficiency distribution. Transmit B_1^+ phase maps are coupled with the current phase in the coil. In parallel transmit array coils, B_1^+ shimming of the phase of individual coils can create desired B_1^+ interference in the imaging subjects (5). Neglecting to model the matching circuit can lead to incorrect B_1^+ phase maps of individual coils, and thus cause incorrect distribution of the transmitted B_1^+ map superimposed from all coil elements. This issue is more critical in ultra-high field simulation, due to the shorter wavelength of the B_1^+ field. Modeling a coil transmit efficiency ($B_1^+/\sqrt{P_{in}}$) distribution close to the empirical coil transmit efficiency is important (39). Transmit B_1^+ produces a tip angle, and it is proportional to the SNR for small tip angle. More importantly, the SAR is proportional to E^2 and B_1^2 . At a given input power (P_{in}), a realistic transmit efficiency improves the safety characterization of the SAR in tissue.

2.1.1 Simulation of a loop coil

We used a commercial full-wave EM simulation software package (XFDTD 7.7.0, Remcom, State College, PA) running on two NVIDIA Quadro K5200 GPU cards. A primary consideration in a conventional RF coil design is the quantity of breaks for discretely distributing capacitance. The value of each discrete capacitor is chosen to optimize the uniformity of the current distribution around the coil, facilitating a uniform B_1^+ field. The inductive reactance of each coil segment should be offset by the reactance of the adjoining discrete capacitor (40). Unnecessarily short segmentation decreases the coil Q-factor owing to the increased equivalent series resistance of additional capacitors and the relatively higher resistivity of solder compared to the primary coil conductor. In contrast, excessively long segments produce phase shifts that lead to destructive B_1^+ interferences and undesired radiation losses. The coil used in this study is a 12-break loop coil, shown in Figure 2-1-(c); limiting each coil segment length to roughly $\lambda/16$ has been shown

effective at minimizing phase shifts (41) and is generally considered a rule-of-thumb. This length translates to about 6 cm at 7T. A phantom slab with conductivity of 0.55 S/m and relative permittivity of 80 is placed 1 cm away from the coil surface. A PEC (perfect electrical conductor) sheet is placed 4.5 cm away from the coil, acting as an RF shield.

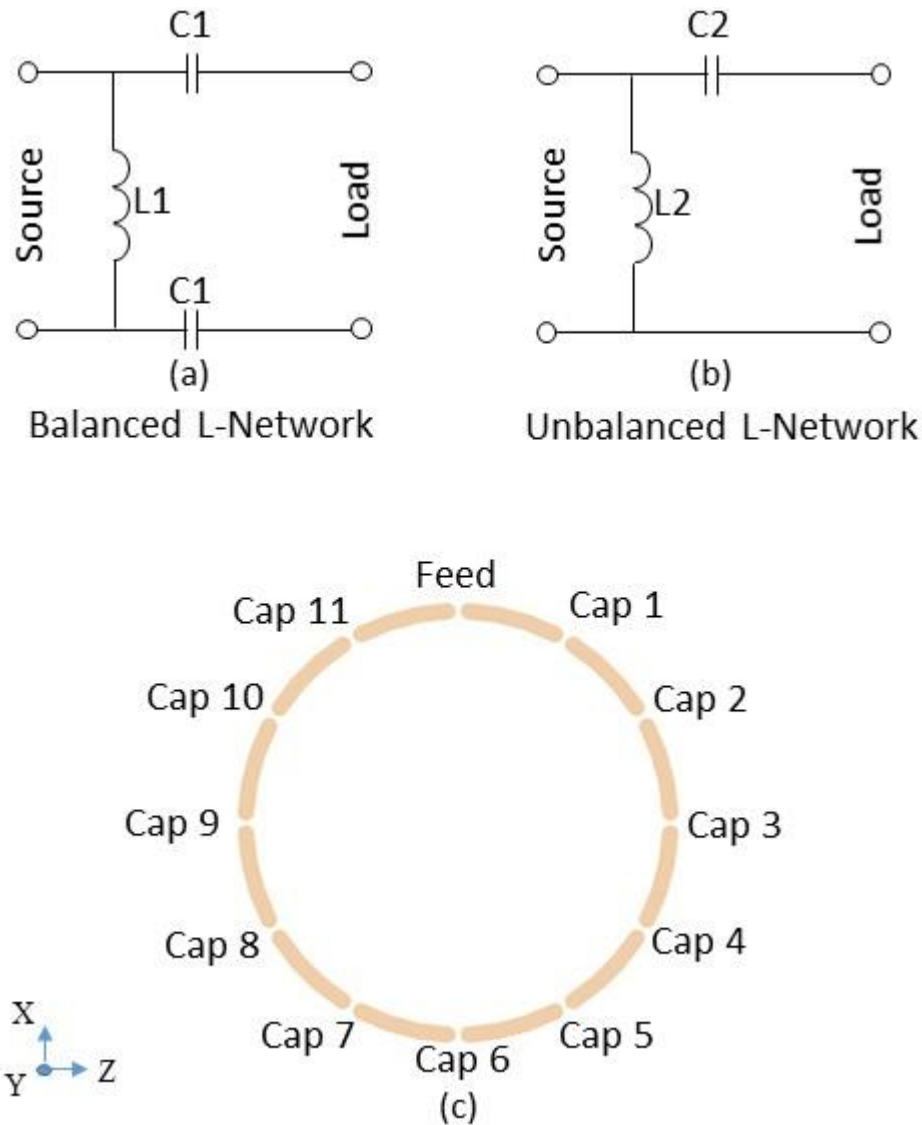


Figure 2-1. The balanced L-network (a) is made by an inductor of 19.2 nH and two 18.8 pF capacitors. The unbalanced L-network (b) is made by an inductor of 19.2 nH and one 9.4 pF capacitor. (c) For the loop coil with 12 gaps, the current source is inserted in the feed.

Coil tuning approaches

For simulating 7T MRI, the goal is to tune the 12-break loop coil to 298 MHz. Current sources are first connected across all 12 gaps. The current source impedance is set to two values for evaluation: $0\ \Omega$ and $50\ \Omega$; both settings result in the same input reactance, but the latter facilitates a greater than three-fold acceleration in simulation time. Accordingly, the $50\text{-}\Omega$ current source is used as the feed for the remainder of this study. We tune the coil using the ideal drive method first mention in (42). We use the 298 MHz sinusoidal wave as the excitation wave to find the input reactance seen from each currents feed. The current feed in each of the 12 gaps is replaced by the capacitor calculated from the input reactance. Across the feed gap, a $50\text{-}\Omega$ current source is also inserted, in parallel to the capacitor. The sources are excited by a modulated Gaussian with magnitude -20 dB at the frequency range limits.

Coil matching approaches

The FDTD method can be linked with the popular circuit-modeling tool SPICE (43). The balanced L-network in Figure 2-1-(a) is made by one 19.2 nH inductor and two 18.8 pF capacitors. The unbalanced L-network Figure 2-1-(b) is made by one 19.2 nH inductor and one 9.4 pF capacitor. From the vantage point of the $50\text{-}\Omega$ current source looking into the coil, the coil input impedance is $22.14 - j45.07$, which can be normalized to $0.4428 - j0.9014$. This point can be placed on a standard Smith-Chart with characteristic impedance of $50\ \Omega$. Going from the load to the current source, we can draw two curves to move the input impedance point inward as close as possible to the center of the Smith chart (i.e., $50\ \Omega$). For the unbalanced L-type matching circuit, the two components of the L-type matching circuit are selected based on the corresponding curves that are drawn on the Smith chart (44). For the balanced L-network in Figure 2-1-(a), the capacitor in series to the load can be replaced by two capacitors, each with double the capacitance. In the matching process, the excitation wave form is the modulated Gaussian.

The L-type matching circuits are modeled in SPICE. The matching circuit is embedded in the edge of the FDTD Yee cell. The interface between FDTD and SPICE is the time-stepping E and H fields and the V and I of scalar voltages and currents. It is possible to develop the Norton or Thevenin equivalent circuits for placement on the local FDTD grid edge, and the resulting port

voltage and current is interpreted as the E or H field at the local FDTD cell edge. We found the complexity of the matching circuit increases the simulation execution time.

Tuning and matching

In the ideal drive method, each of the 12 current feeds have an input reactance of about 54Ω , and they are summed up and divide by 12 to have the averaged reactance. This gives a capacitor value of 9.8578 pF. The frequency response of input impedance seen at the feed gap is plotted in the Smith chart and shown in Figure 2-2-(b). The crossing the horizontal line in the Smith chart ($x = 0$ line) is the resonant frequency 298 MHz. If the value of the 12 capacitors decreased from 9.8578 pF to 9 pF, the coil is not on the resonant frequency; this case is shown in Figure 2-2-(a). Without the matching circuit, the tuned coil has stronger and more spatially focused transmit efficiency as compared to the not well tuned coil (Fig. 1-5-(a)(c)), but the phase maps of the B_I^+ fields are the same.

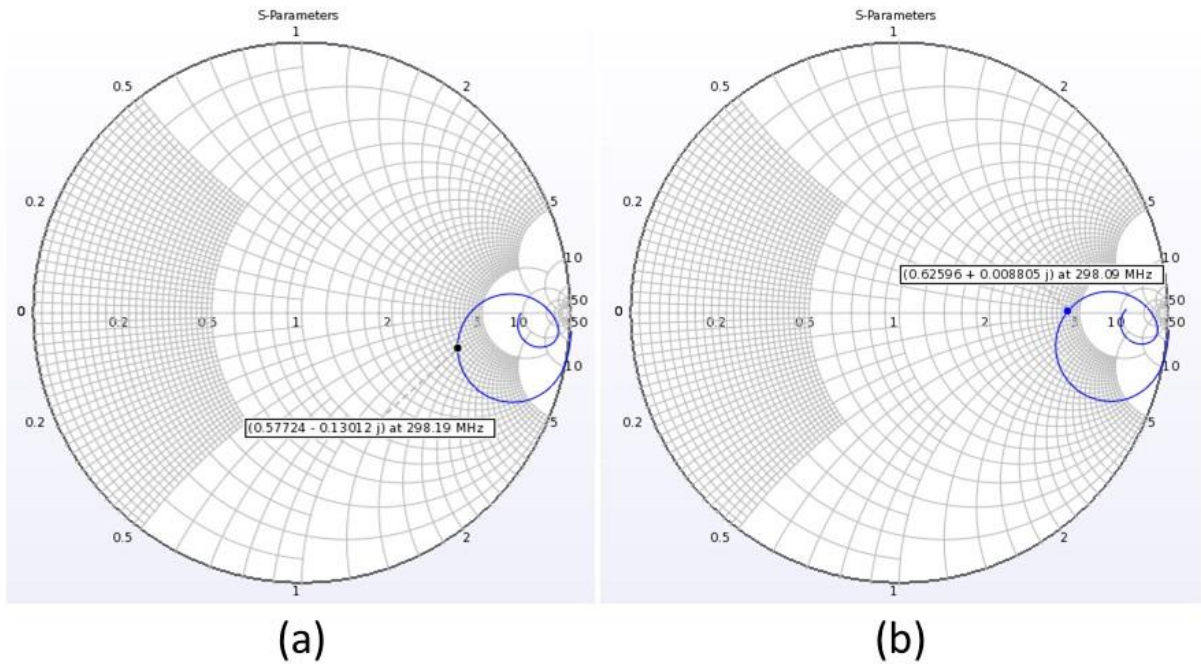


Figure 2-2. The S_{11} evaluated at the feed gap plotted in the Smith chart. (a) This coil is not well tuned and the 298 MHz point is off the horizontal line ($x = 0$) in the Smith chart. (b) This coil is well tuned and the 298 MHz point is on the horizontal line ($x = 0$).

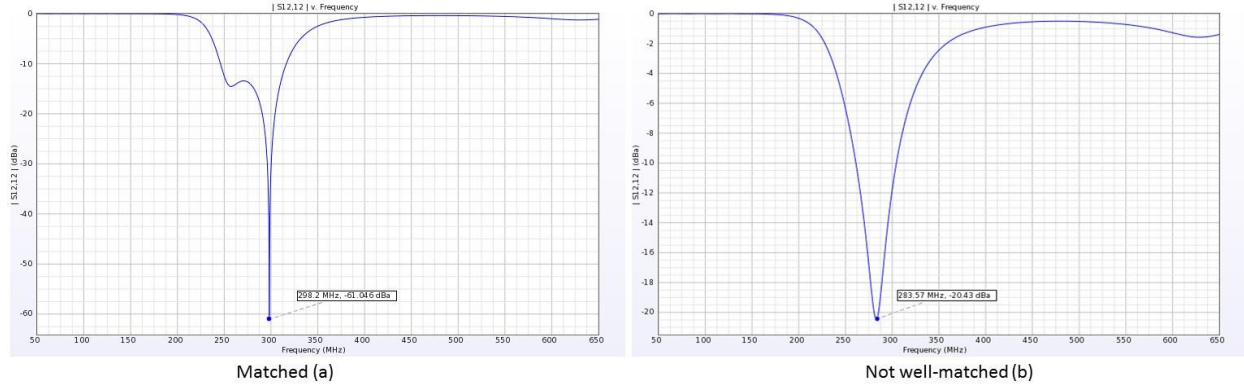


Figure 2-3. The magnitude of S_{11} is plotted against the frequency. **(a)** The S_{11} plot using the balanced L-network or the unbalanced L-network. **(b)** The S_{11} plot when the capacitor (C_2) in the unbalanced L-network is increased from 9.4 pF to 16.3 pF.

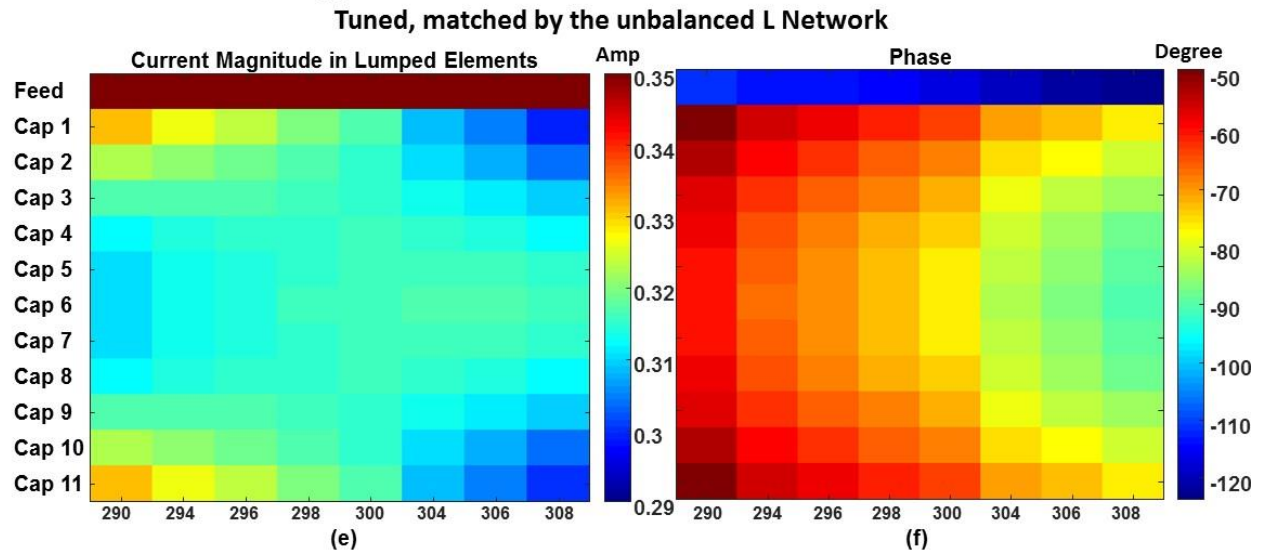
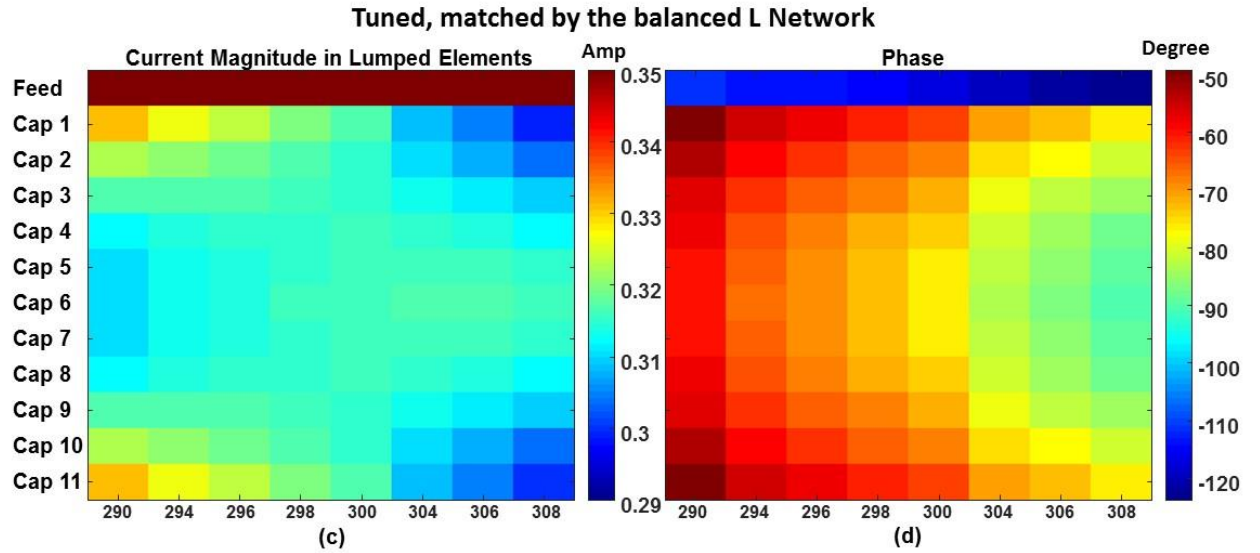
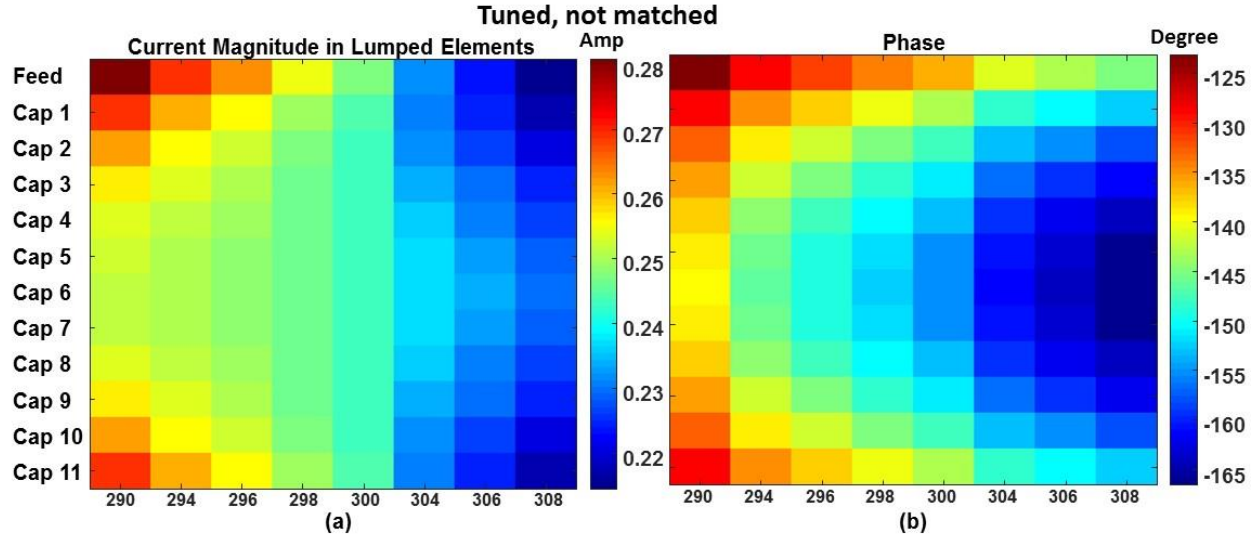
Fig. 1-3(a) shows the reflection coefficient (S_{11}) of the coil after adding the matching circuits. A coefficient of -61 dB is reached at 298 MHz using either the balanced or the unbalanced L network. Fig. 1-3(b) shows the S_{11} plot when the capacitor (C_2) in the unbalanced L-network increased and the circuit is at lower S_{11} value. In this case, the best S_{11} is -20.43 dB at 284 MHz.

2.1.2 Matching and tuning effect on the coil currents and RF efficiency

Coil currents

The total current in each coil segment is reported as the current going through the adjacent lumped element. Figure 2-4 shows the current phase and magnitude going through the gaps of the coils from 290 to 308 MHz. All coils are tuned to 298 MHz, so the current distribution is ideally uniform around the resonant frequency, from 298 to 300 MHz. The matched coils have currents of higher magnitude as compare to the unmatched coil. The input power is proportional to the square of current in the loop. At the same coil input impedance, there is more input power in the impedance-matched coil. Given the added reactive components in the matching circuit, there is a phase increment of roughly 75° in the currents from the unmatched to the matched coils.

Figure 2-4. The current distributions in the 12 lumped elements of the coil, plotted from 290 MHz to 308 MHz. The current source is 1 A and $50\ \Omega$ for all cases. The first row from the top is the tuned but unmatched loop coil and its current magnitude distribution within the lumped elements **(a)** and the phase distributions **(b)**. The middle row is the coil tuned and matched with the balanced L network, and the current magnitude distribution shows in **(c)**, and the phase distribution shows in **(d)**. The bottom row is the coil tuned and matched with the balanced L-network, and **(e)** is the current magnitude distribution; **(f)** is the current phase distribution.



The transmit efficiency

The transmit efficiency ($\mu T/\sqrt{W}$) is defined as the transmit B_I^+ magnitude normalized by the square root of the input power. The transmit efficiency and phase maps are shown in Figure 2-5. The transmit efficiency is the highest in the tuned and un-matched coil as shown in Figure 2-5-(a). Fig. 1-5(c), (e), (g) and (i) show the percentage difference from the transmit efficiency in Figure 2-5-(a), and in all cases the transmit efficiency decreased. If the coil is well tuned, adding the matching circuits changes the transmit efficiency spatial pattern. Additionally, adding the matching circuits changes the phase in B_I^+ field. The phase maps are the same for all the matched coils. The B_I^+ phase increases roughly 60° from the unmatched to the matched coils. This phase increment is close to the phase increment in the currents. Finally, both the balanced and the unbalanced L-networks produced the same transmit efficiency and phase maps.

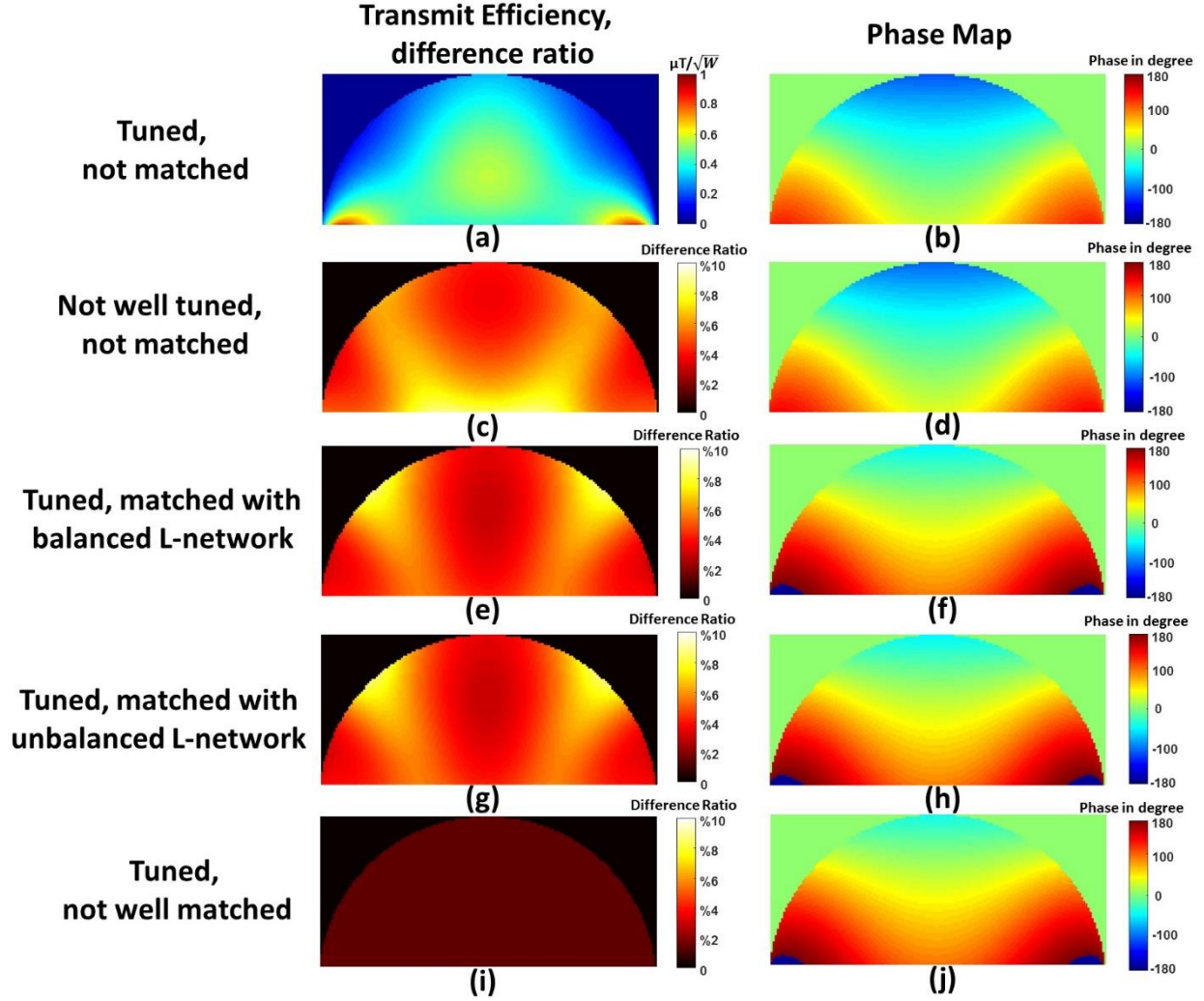


Figure 2-5. Transmit efficiency and phase maps in the sagittal plane (YZ plane) within the slab phantom. The first row illustrates the (a) transmit efficiency ($\mu T/\sqrt{W}$) and (b) B_1^+ phase map of the tuned, not matched coil. The second row shows (c) the percentage ratio of transmit efficiency of the tuned, not matched coil to the transmit efficiency of (a), and (d) the phase map. The third row similarly shows (e) the difference ratio and (f) the phase map for the coil tuned and matched with the balanced L-network. The fourth row shows the (g) difference ratio and (h) the phase map for the coil tuned and matched with unbalanced L-network. The fifth row shows (i) the difference ratio and (j) the phase map for the coil tuned, but not well matched.

Conclusion

This work demonstrates the tuning and matching approaches for modeling RF coils, and how each may affect the magnitude and phase of the resulting currents, the transmit efficiency and the phase of the complex maps. The tuned coil has a greater transmit efficiency compared to the

untuned coil. Adding a matching circuit can result in spatially focusing the transmit efficiency map. Furthermore, adding the matching circuit will add a phase shift to the B_1^+ complex map, which is determined by the current phase around the coil loop. Therefore, to validate a coil modeling with empirical model design, it is necessary to have the coil tuned, and matched to the experimental resonant frequency.

2.2 A comparison of FDTD and FEM solvers for simulating a surface loop coil with tissue phantom

Two popular electromagnetic (EM) simulation methods used in MRI RF coil simulations are the frequency-domain finite element method (FEM) and the finite-difference time-domain (FDTD) method, and both provide powerful capability for meshing detailed body and surface. There are several popular solvers: the frequency-domain HFSS (ANSYS, PA, USA), the time-domain XFDTD (Remcom, PA, USA) and the time-domain Sim4Life (Zurich MedTech AG, Zurich, Switzerland) solvers (we used Sim4Life in section 1.3.1.). In this section we use both methods to simulate a surface loop coil in 7T at a very fine level of mesh resolution, transmitting the RF coil on a muscle and a fat phantom, at 1 cm and 0.5 cm gap distance from the coil to phantom surface as shown in Figure 2-6.

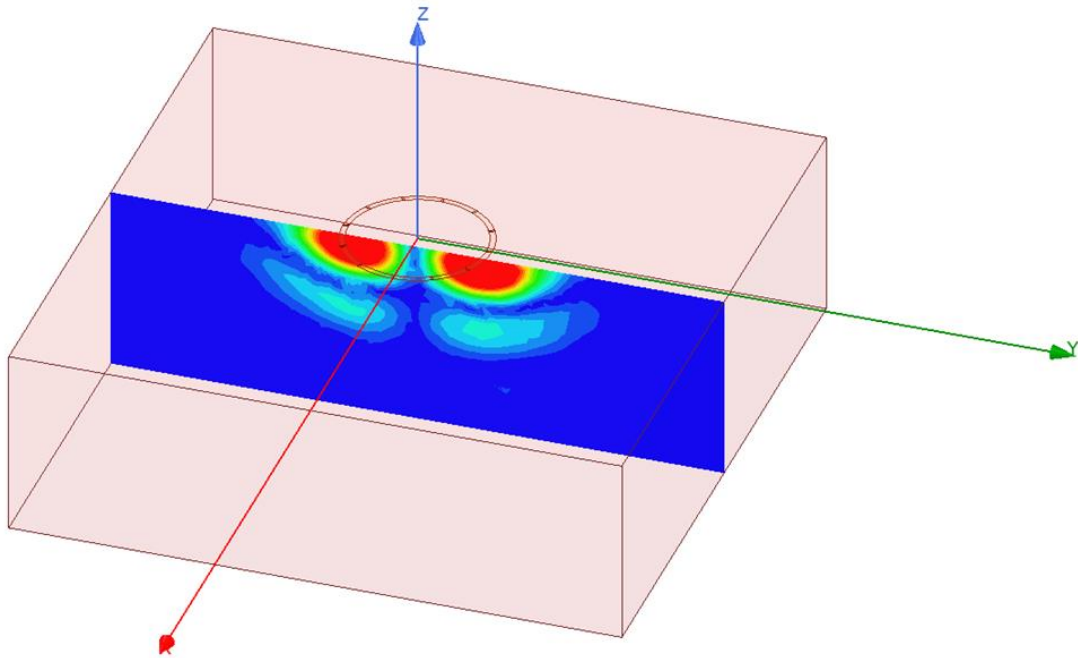


Figure 2-6. Simulation setup of a surface loop coil over a tissue phantom.

2.2.1 Background of HFSS and XFDTD

Electromagnetic (EM) simulation of MRI RF coils can facilitate RF coil design and validate patient safety due to RF heating. The finite-difference time-domain (FDTD) and finite element method (FEM) solvers are general methods to solve Maxwell's equations to derive the electric and magnetic fields. HFSS has a reliable adaptive meshing algorithm for curved surfaces. Additionally, the ANSYS Circuit module is used for the circuit domain co-simulation. XFDTD offers XACT meshing capability for curved body, and the circuit components are meshed within the 3D simulation gridding. The mesh of the two solvers are shown in Figure 2-7. This study compares the performance of these two solvers at simulating a RF transmit coil in 7T, oriented above a fat and muscle phantom, at 1 cm and 0.5 cm gap distance from the coil to phantom.

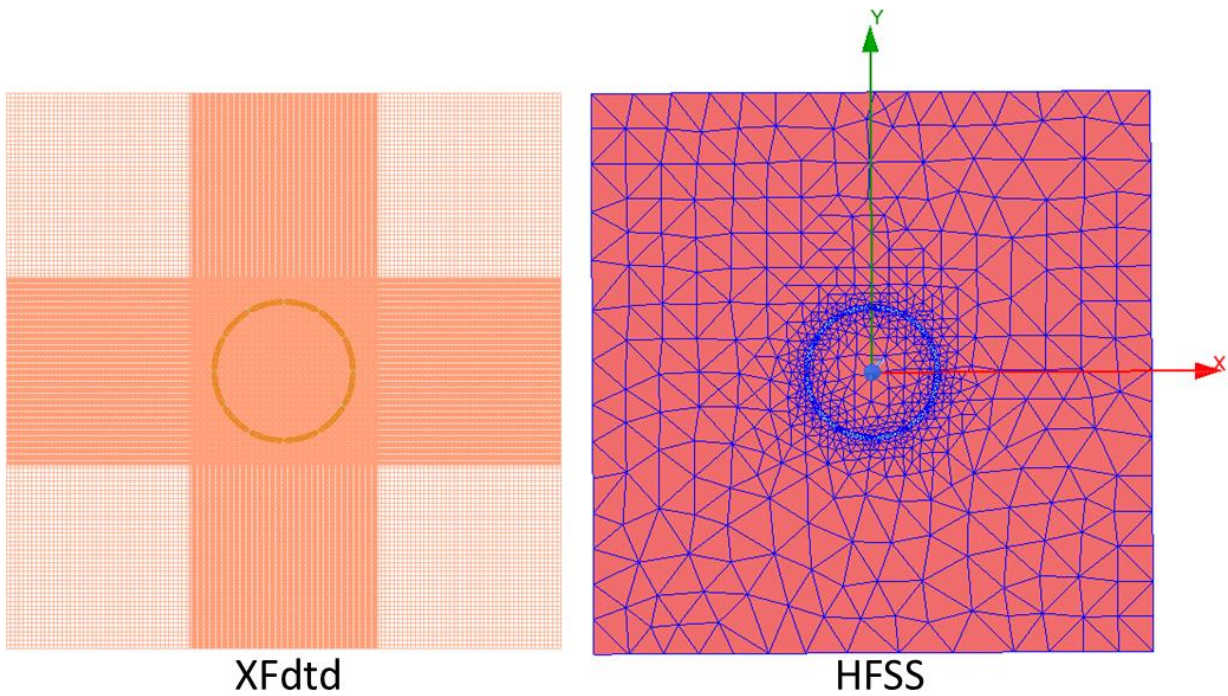


Figure 2-7. Meshed coil and phantom in XFDTD and HFSS.

2.2.2 Comparison of E and B fields

Figure 2-8 shows the E and B_1^+ maps in the muscle phantom in the sagittal view at gaps of 1 cm and 0.5 cm, respectively. Figure 2-9 shows the E and B_1^+ maps in the fat phantom in the sagittal view at gaps 1 cm and 0.5 cm respectively. The E and B_1^+ maps have distinct distribution

in fat and muscle. Different gap distance (in the range of 0.5 cm to 1 cm) has a subtle influence on the field distributions.

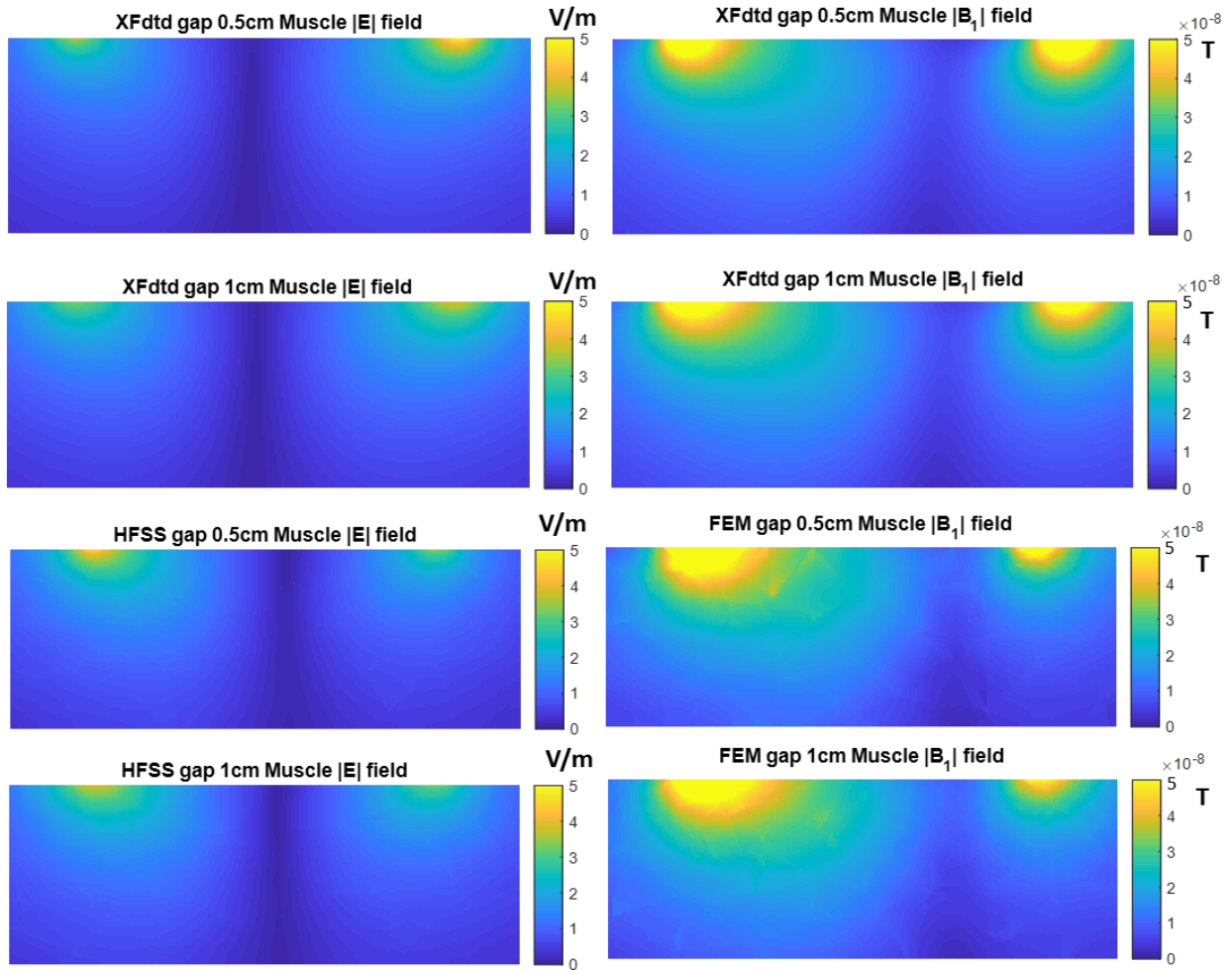


Figure 2-8. E and B_1^+ field strength in a cross section of the muscle slab.

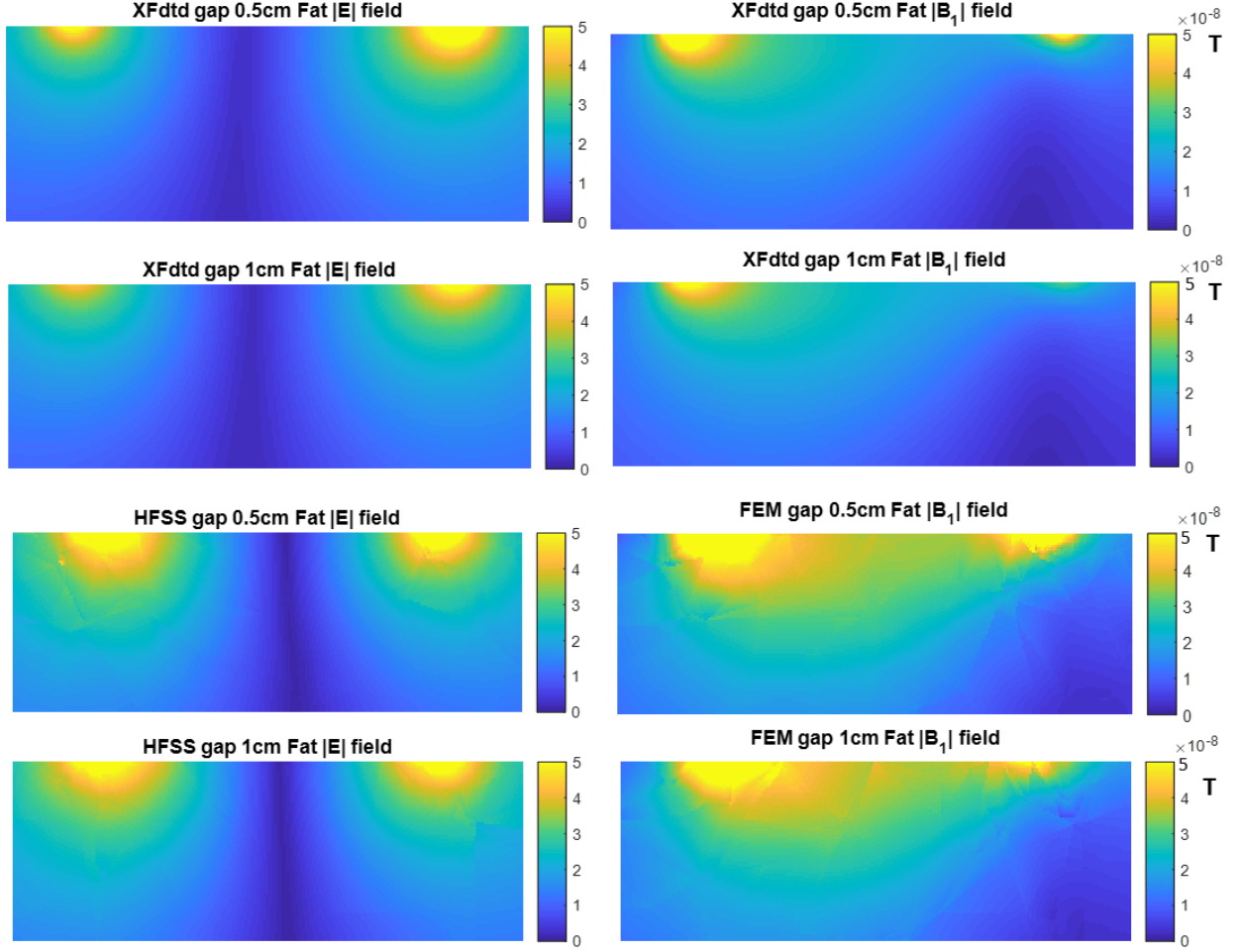


Figure 2-9. E and B_{I^+} field strength in a cross section of the fat slab.

This study investigates the difference in the E and B_{I^+} distribution using the HFSS and XFDTD solvers for RF coil simulation at a very fine level of mesh resolution. When the simulating parameters are carefully selected, both simulation solvers present similar results. In a close look, FDTD produce slightly finer and smoother field data.

2.3 Bench measurement of S parameters of two loop coils

The two coils decoupled by the Resonant inductive decoupling (RID)(45) circuit is shown in Figure 2-10-A. Each feed port of the coil is connected to a vector network analyzer (E5071C, Keysight Technologies, Santa Rosa, CA, USA). The RID decoupling theory is described by the colored arrows in Figure 2-10-A. The red arrow denotes the induced current by current in loop 1,

and the induced current (red arrow) flows in the opposite direction of the current induced by the RID in loop 2 (green arrow). The S_{12} measurement of the network analyzer is shown in Figure 2-10-B (without RID) and Figure 2-10-C (with RID).

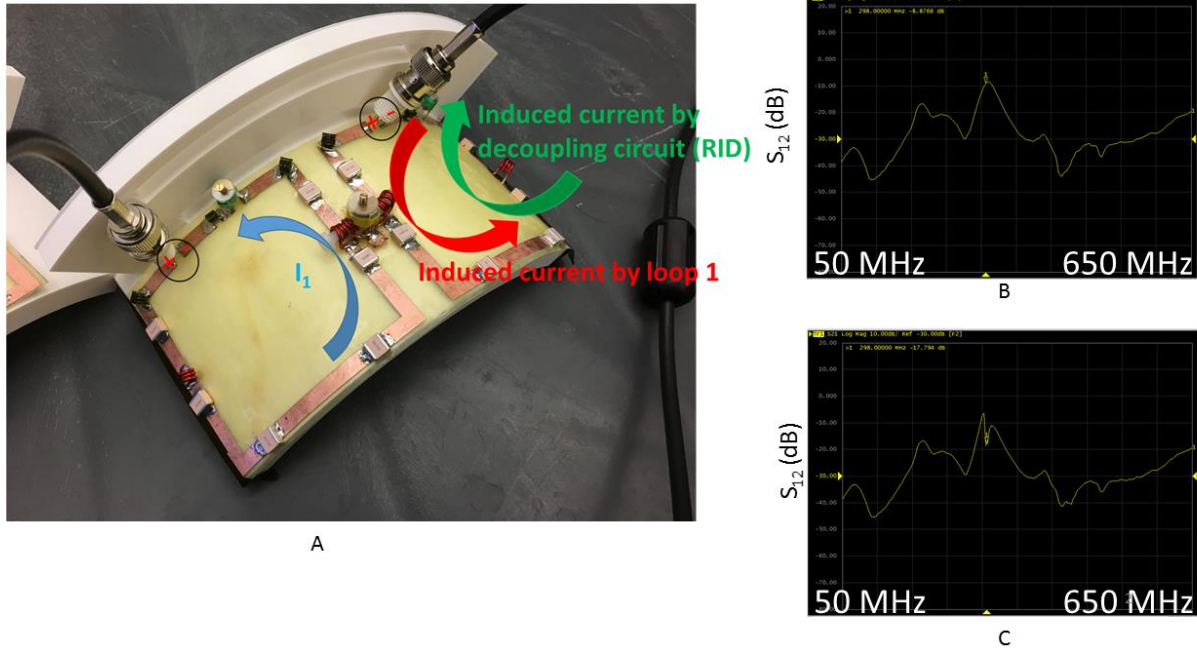


Figure 2-10. Bench Measurement of two coils decoupled by Resonant inductive decoupling (RID) (A), the S_{12} coefficient without RID (B), and S_{12} coefficient with RID (C).

2.3.1 Measuring coil input impedance

We employ bench measurements to confirm the simulated coil and in vivo coils have similar input impedances in the unloaded condition, for a single loop coil of the two coils shown in Figure 2-10-A. During measurement of the input impedances, we did not include a matching circuit at the simulation or physical coil inputs as doing so would prevent validation of the standalone coil structures. The input impedance plotted in a Smith chart is shown in Figure 2-10. Using a vector network analyzer, the measured single coil input impedance is $6.4 + j145.0 \, \Omega$. In XFDTD the input impedance is $4.7 + j194 \, \Omega$, and $3.3 + j164.2 \, \Omega$ in Sim4Life. Comparing the bench measurement

and simulation measurement, there are 19.0% difference in magnitude and 1.4 % difference in phase.

2.3.2 Circuit simulation of the RID decoupling

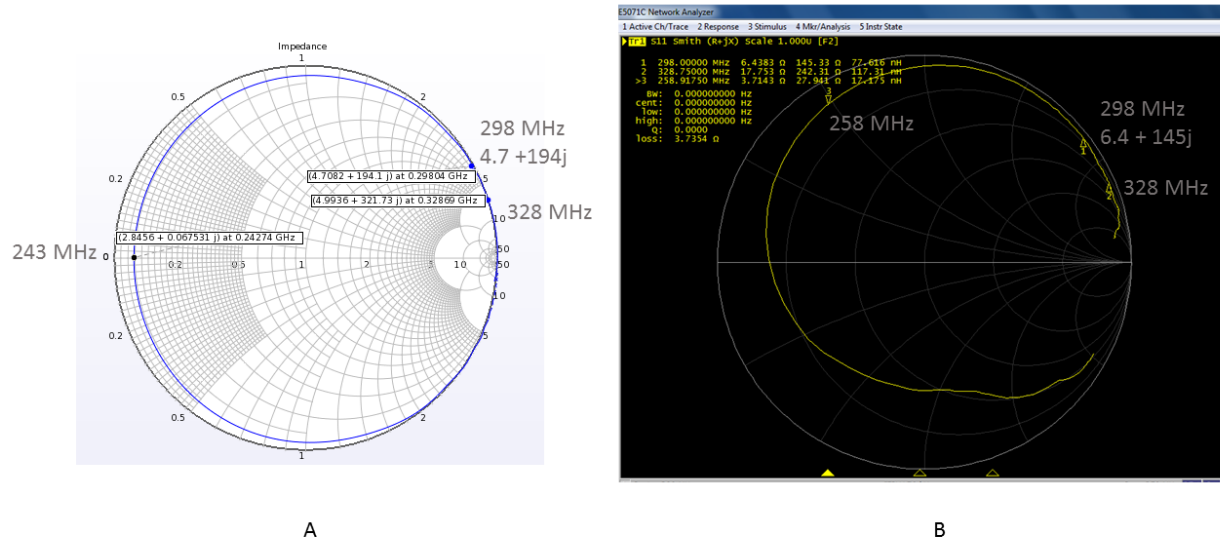


Figure 2-11. Input Impedance plotted in a Smith chart (Auto wave 50 - 650 MHz) for XFDTD (A) and Network Analyzer (B).

We used ADS 2020 (company, city, state, USA) to create the circuit schematic shown in Figure 2-12-A, to represent the two coils shown in Figure 2-10-A. The coil S parameters with and without RID are shown in Figure 2-10-B. A dip at 298 MHz is shown in the S_{12} , when the two coils are decoupled by RID, while the S_{11} and S_{22} are not affected by the RID.

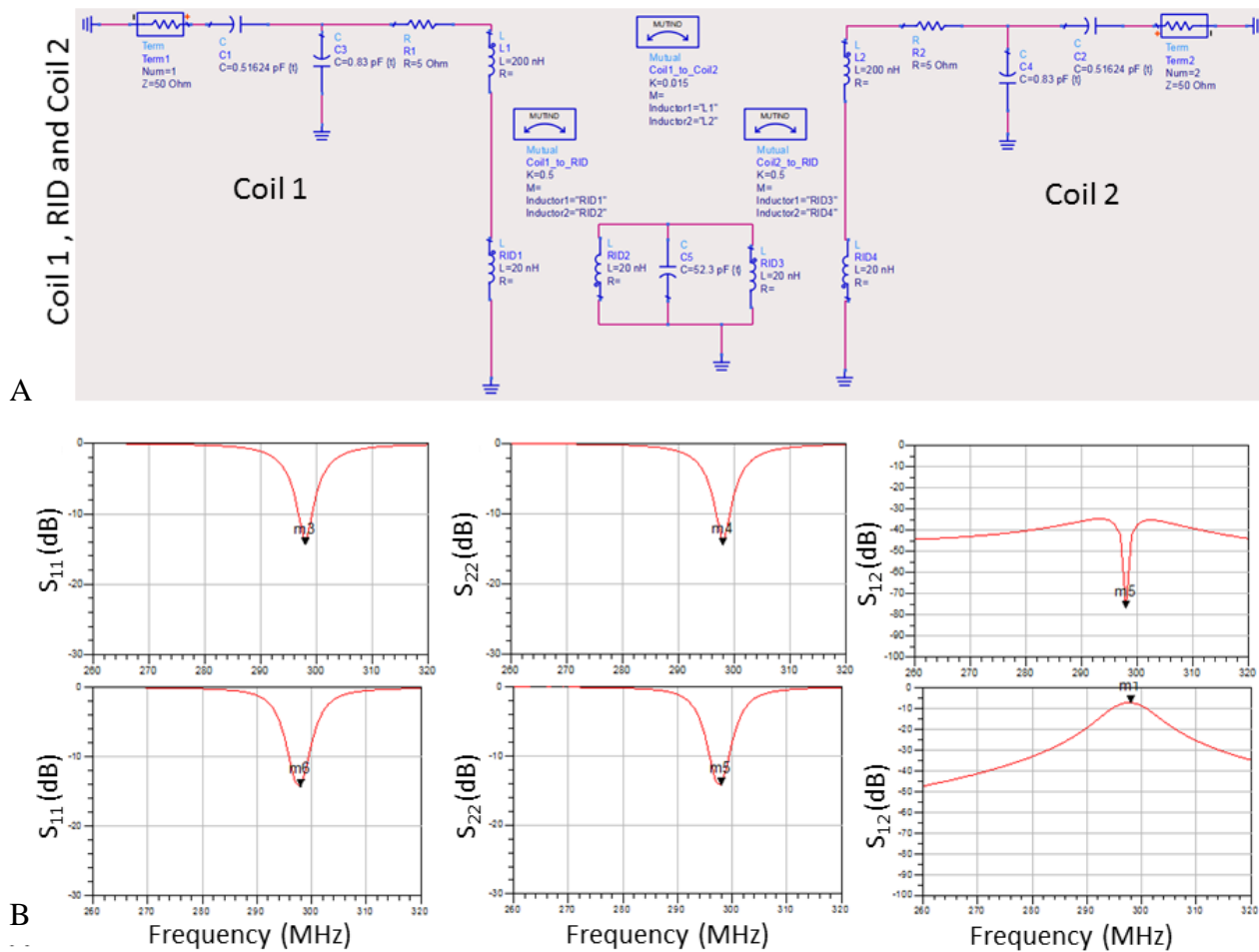


Figure 2-12. A: circuit simulation of the two coils shown in Figure 2-10. B: S parameter plots of the two coils (the top row is with RID, the bottom row is without RID).

3. SIMULATION OF HETEROGENEOUS BREAST MODELS IN RF EXPOSURE

This chapter is reprinted with permission from Li & Rispoli (2); ©2019 Wiley Periodicals, Inc.

To facilitate assessment of RF power deposition and temperature rise within the breast, we present a method to seamlessly join heterogeneous breast models with standard whole-body models and demonstrate simulations at 7 T. Finite-difference time-domain electromagnetic and bioheat simulations are performed to analyze specific absorption rate (SAR) and temperature rise distributions in 36 BI-RADS-categorized breast models fused to two female whole-body models while transmitting from a 7T breast volume coil. The breast models are uncompressed in the prone position and feature heterogeneous tissue contents; fusion with human models utilizes affine transformation and the level-set method. The fusion method produces a continuous transition from the chest region to the posterior portion of breast models while preserving the original volume and shape of breast models. Simulation results of both Ella and Hanako models indicate the maximum local SAR, partial body SAR, and local tissue temperature rise are positively correlated with both breast density and the highest BI-RADS density classification. Additionally, maximum local tissue temperature rise is positively correlated with maximum 10-g SAR values. Fibroglandular tissue content plays an important role in the distribution of SAR and temperature rise within breast tissue. The combined body-breast models preserve the integrity of breast models while concurrently exhibiting the loading of whole-body human models. The procedures presented in this simulation study facilitate safety assessments for breast MRI across the population at both clinical and ultra-high field strengths.

3.1 Background

3.1.1 Breast MRI

Breast cancer is the most commonly diagnosed cancer and leads to the highest death rate among women in the United States. In 2016, roughly 246,660 new incidences of breast cancer were diagnosed, corresponding to 29% of all new cancer cases, while breast cancer caused 40,450 deaths, equaling 14% of all cancers deaths (7). Compared to other imaging modalities, MRI offers

high sensitivity for breast cancer detection (8,9) and is commonly indicated for screening high-risk subjects, e.g., women with familial history, genetic predisposition, significant chest radiation history, or lobular cancer (10,11,46,47). Furthermore, owing to superior contrast between tumor and fibroglandular tissue, MRI has been reported to improve sensitivity within dense breasts (14,15), i.e., those clinically classified as heterogeneous or extreme fibroglandular tissue according to the American College of Radiology Breast Imaging Reporting and Data System (BI-RADS) Atlas (48). The increased signal-to-noise ratio at 7 T enhances both temporal and spatial resolutions of dynamic contrast-enhanced breast MRI, thus improving sensitivity; the diagnostic specificity of breast MRI may be extended by using supplementary techniques including diffusion-weighted MRI and magnetic resonance spectroscopy, which also have improved performance at 7 T (17–19). However, radiofrequency (RF) power deposition—quantified as specific absorption rate (SAR)—must be well characterized, particularly at high fields. Both the U.S. Food and Drug Administration (FDA) and the International Electrotechnical Commission (IEC) include SAR as a criterion for assessing significant risk in MRI devices (20,21). The IEC60601-2-33 standard specifies SAR limits and temperature limits at normal operating mode and first-level controlled operating modes, while second-level controlled operating mode requires SAR limits be specifically approved by an appropriate investigational review board. For a volume transmit coil at normal operating mode, the partial body SAR limit is 2-10 W/kg (determined by the ratio of exposed patient mass to patient mass), and the maximum local temperature limit is 39 °C. For a local transmit coil at normal operating mode, the local SAR (10-g averaged SAR) limit is 10 W/kg for trunk and 20 W/kg for extremities, and temperature constraints are the same as for a volume transmit coil.

3.1.2 SAR measuring and simulation

Experimental methods to determine SAR values in tissue rely on either measuring the temperature rise of a loaded phantom or by measuring the energy per pulse delivered by RF coils (49). At present, the real-time in vivo determination of regional SAR values in tissue is unfeasible. The finite-difference time-domain method (FDTD) simulation method for electromagnetics (EM) utilizes a simple numerical integration algorithm and facilitates SAR calculation in human body models of different resolution (50–53). While the FDTD method is robust for whole-body simulation, caution must be undertaken if simulating cropped regions of the body (e.g., head only).

Wolf et al. showed that adjoining body parts outside the coil affect the resulting EM fields inside the coil, and a cropped body part alone will exaggerate the resulting SAR values (54).

Researchers have access to a limited number of noncommercial adult female whole-body models for SAR simulations; four prominent examples are detailed in Table 3-1.

Table 3-1. Attributes of Selected Adult Female Whole-Body Voxel Models

Name	Resolution [mm]	Height [cm]	Tissue Types	Year Released
Ella	0.5	160	76	2013
Hanako	2	159	51	2004
Naomi	2	163	41	2005
High Fidelity Female Body Mesh	5	165	36	2005

All four models are oriented in the standing or supine positions (55–58), where breasts are flattened with suboptimal visualization, thus requiring adaptation to accurately simulate breast MRI in the prone position. Prone position breast imaging provides separation of deep breast structures from the heart, liver and pectoral muscles, offering greater resolution of small lesions in deep breasts (59) and avoiding respiratory and potential cardiac artifacts (60–62). Most recently, Kim et al. studied the SAR and B_1^+ field in various types of breast models (63), however, there was no discussion on the method of fusion of the breast models to human voxel models and the influence on SAR from the chest region of the body model was unknown. Van der Velden et al. combined 2-mm resolution unilateral breast models generated from segmented MRI images of five study volunteers—a personalized modeling paradigm requiring a priori 3D image sets—with a whole-body model for FDTD simulations (64); however, the overlap-fusion method is susceptible to producing embedded skin layers, and the study participants did not represent all BI-RADS breast composition categories.

To accurately assess and quantify the breast regional 10-g SAR, partial body SAR and tissue temperature values, we propose EM and thermal simulations of patient-based breast models covering all BI-RADS breast composition categories— designated a, b, c, and d—in a breast-specific volume transmit coil (38). In this work, the patient-based breast models are created from segmented MRI and CT images of uncompressed (i.e., free of compression plates) breasts of human subjects in the prone position. Our fusion technique then joins the breast models with a

human model by applying: 1) affine transformation to create a curved breast posterior portion to be positioned on the top of the chest of human models; 2) the level-set method of mean curvature motion, a general method in the computer vision community to seamlessly fuse joints or reconstruct surfaces (65–67). Our simulations illustrate homogenous B_1^+ field distributions in the coil effective volume; and the 10-g SAR, partial body SAR and tissue temperature values are quantified at a mean B_1^+ within the coil effective volume, based on the TR-averaged B_1^+ used in practical breast MRI scans at 7 T (38,68–70).

3.2 Breast Modeling

We adapted nine MRI image-derived breast models (0.5-mm isotropic resolution) made available by the University of Wisconsin Cross-Disciplinary Electromagnetics Laboratory (71), and nine CT image-derived breast models (0.35-mm isotropic resolution) from the Carl E. Ravin Advanced Imaging Laboratories at Duke University (72). All breast models were uncompressed and in the prone position; the set included models from all four BI-RADS classifications: a, b, c, and d. Dielectric properties were assigned from the IT'IS Foundation Database (73). For quantitative analysis, we labeled the breast models by the volumetric fibroglandular tissue (FGT) percentage (FGT%).

Tissue types in each breast model included skin, breast adipose, FGT, and three (intravoxel) FGT-adipose combinations of varying FGT makeup, by volume percentage: 25%, 50%, and 75%. FGT-adipose tissue with higher proportions of FGT border the densest regions, which are typically in the center of the breast. We linearly distributed the dielectric properties at 298 MHz for the three FGT-adipose mixture definitions (i.e., 75%, 50% and 25 % FGT-adipose mixture) between that of 100% FGT ($\epsilon_r = 62.5$, $\sigma = 851$ mS/m) and adipose tissue ($\epsilon_r = 5.54$, $\sigma = 32.7$ mS/m). Our motivation to define the above tissue types derives from Zastrow et al., who showed linearly decreasing dielectric properties between 0-5 GHz for four tissue types dubbed “glandular/fibroconnective-1”, “glandular/fibroconnective-2”, “glandular/fibroconnective-3”, and “transitional” (74). Likewise, for the CT image-derived breast models, Erickson et al. defined adipose tissue, four heterogeneous proportions of FGT and adipose mixtures, and skin based on linearly increasing voxel intensities in breast computed tomography (bCT) data (72).

For this study, we employed two adult female models with superior tissue counts and relatively high resolution: Ella and Hanako. The 0.5-mm isotropic Ella model is part of The Virtual

Family 1.2 and represents a 26-year-old female of height 160 cm and mass 58 kg (58). The 2-mm isotropic Hanako model is from Japan's National Institute of Information and Communications Technology (NICT) and represents an average 18- to 30-year-old Japanese female of height 159 cm and mass 52.6 kg (55).

3.2.1 Model Fusion Algorithm

Morphological Filtering

Closing and opening morphological operators (75) are applied to smooth the pectoral muscle wall. Firstly, the pectoral muscle wall is converted to a binary image volume, with ones representing the pectoral muscle and bones, and zeros representing empty space. Next, we smooth the binary image volume by a three-dimensional image-closing morphological operator; the kernel is a 5-voxel diameter solid sphere for the Hanako model and a 15-voxel diameter solid sphere for the Ella model. Subsequently, we fill empty voxels inside the pectoral muscle wall with a voxel value of one. Finally, we smooth the binary image volume with a three-dimensional image-opening morphological operator, using the same kernel sizes defined previously.

Affine transformation

The posterior portion of the breast model is projected on top of the smoothed pectoral muscle wall surface using affine transformation. N voxels from location $[x, y, z]$ are transformed to $[x, y, z - d_i]$, where $i = 1, 2, 3 \dots N$, and d_i is the z projection values of the pectoral muscle wall surface. Our initial implementation of this method was previously described in (76,77).

Level set method of mean curvature motion

The fusion of the posterior portion of the breast model to the subcutaneous adipose of the chest region is achieved via a mean-curvatures regularized level-set motion algorithm (67). A minimal amount of subcutaneous adipose is added. Consider the common level set function

$$\frac{\partial \Phi}{\partial t} = -b\kappa|\nabla \Phi| \quad [3-1]$$

where Φ is the time dependent level set function that determines a dynamic contour when $\Phi(x, y, z, t) = 0$, b is a constant that controls the speed of the active contour, $\nabla\Phi$ is the inward vector normal at the dynamic contour, and κ is the mean curvature. Eq. 3-1 can be decomposed to

$$\frac{\partial\Phi}{\partial t} = -\frac{b}{2}(\kappa_1 + \kappa_2)|\nabla\Phi| \quad [3-2]$$

where κ_1 and κ_2 are the maximal and minimal curvatures, i.e., the principle curvatures, derived from the mean curvatures (κ_M) and Gaussian curvature (κ_G) equations in (78):

$$\kappa_1, \kappa_2 = \kappa_M \pm \sqrt{\kappa_M^2 - \kappa_G} \quad [3-3]$$

where

$$\kappa_M = (\Phi_x^2\Phi_{yy} - 2\Phi_x\Phi_y\Phi_{xy} + \Phi_y^2\Phi_{xx} + \Phi_x^2\Phi_{zz} - 2\Phi_x\Phi_z\Phi_{xz} + \Phi_z^2\Phi_{xx} + \Phi_y^2\Phi_{zz} - 2\Phi_y\Phi_z\Phi_{yz} + \Phi_z^2\Phi_{yy})/|\nabla\Phi|^3 \quad [3-4]$$

and

$$\kappa_G = -\frac{\begin{vmatrix} \Phi_{xx} & \Phi_{xy} & \Phi_{xz} & \Phi_x \\ \Phi_{xy} & \Phi_{yy} & \Phi_{yz} & \Phi_y \\ \Phi_{xz} & \Phi_{yz} & \Phi_{zz} & \Phi_z \\ \Phi_x & \Phi_y & \Phi_z & 0 \end{vmatrix}}{|\nabla\Phi|^4}. \quad [3-5]$$

To consider the outward motions for both concave and saddle surfaces, we take the positive components of the principle curvatures and denote them by κ_1^+ and κ_2^+ . Thus Eq. 3-2 becomes

$$\frac{\partial\Phi}{\partial t} = -b(\kappa_1^+ + \kappa_2^+)|\nabla\Phi|. \quad [3-6]$$

Implementation

The model fusion software is implemented in MATLAB (MathWorks, Natick, Massachusetts, USA), and the source code is publicly available (<https://github.com/rispoli-lab/Bilateral-Breast-Fusion->). The implementation of the fusion scheme for bilateral breasts consists of the following steps:

1. Unilateral breast models are scaled to the desired size, with aspect ratio using a 3D nearest-neighbor interpolation. The scaling factor is approximately the ratio of breast model voxel length to the human model voxel length. In our simulation study, the breast models are resized to cover all breast tissue contained in Ella and Hanako models. Unilateral breast models are mirrored referring to the center sagittal plane of human models to generate bilateral breast models. Circular rings representing a breast RF coil

are positioned outside of the scaled breast models to ensure the tissue-to-coil spacing is at least 1 cm, and the coil's coordinates relative to the human model are saved for positioning the breast coil in the EM simulation software in step 4. Notably, the breast coil will be fixed at the same location with respect to the human model (e.g., Ella and Hanako).

2. In preparation for becoming the interface between the breast and body models, the pectoral muscle and bone volumes in the female body model are extracted and smoothed by morphological filtering. Affine transformation is applied on the breast model to create a curved posterior portion that fits on the surface of the smoothed pectoral muscle and bone.
3. A 3D region is selected, containing the joints of the posterior portion of the breast model and the chest of the human model. The level-set method is applied on the selected region to smooth the sharp joints and edges at the outer layer of the integrated model. Extra tissue added by the level-set method is labeled as subcutaneous adipose tissue (SAT). A skin layer of fixed depth is sequentially added on the top of the SAT layer. The smoothed 3D region is then merged with the breast-chest model to create the modified breast model. The modified breast's coordinates relative to the human model are saved for positioning the breast model in the EM simulation software in step 4.
4. The modified breast model is saved, imported into EM simulation software and positioned at the desired location based on location coordinates generated from step 3. Breast models are assigned an elevated meshing priority to overwrite breast tissues contained in Ella and Hanako. The breast RF coil is positioned based on the location saved in step 1.

3.3 Electromagnetic and thermal simulations

3.3.1 Breast RF coil modeling

We use a commercial full-wave simulation software package (XFDTD® 7.7, Remcom, State College, Pennsylvania, USA) for electromagnetic and thermal simulation. For this study, the modified breast models are saved in the voxel file (.vox) to facilitate importing into XFDTD. Following successful voxel file import, the modified breast models are assigned a high mesh

priority and consequently overwrite the breast regions of the body models; notably, the body model is never explicitly modified and saved, facilitating compliance with common licensing terms that prohibit truncating or segmenting the models. To mitigate potential discretization effects from combining multiple gridded objects, mesh cells were created with averaged dielectric properties.

A previously-reported quadrature breast coil (Figure 3-1) composed of orthogonal Helmholtz and saddle pairs (38) is modeled by copper sheet of conductivity 5.96×10^7 S/m. The contour path method is utilized to mesh curved coil conductor geometries (79). All coil elements are segmented by capacitors, and fined-tuned using the ideal drive method to match input impedances from bench measurements (37). The two coil pairs are in quadrature operation and driven by 298-MHz sinusoidal current feeds with appropriate 90° phase separation to achieve equal input power for both pairs.

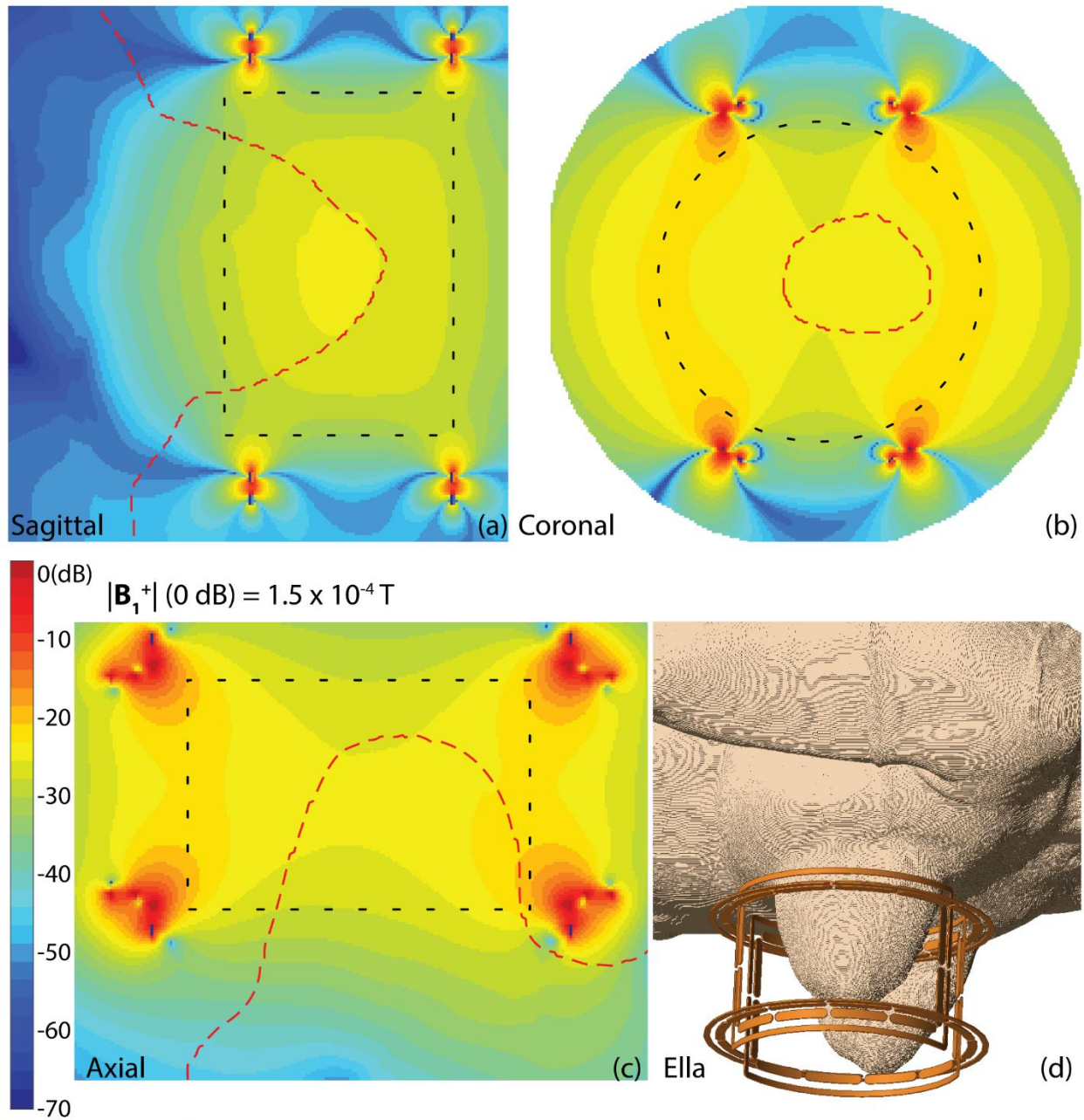


Figure 3-1. B_1^+ spatial profile of a loaded breast coil in the sagittal (a), coronal (b), and axial (c) planes. The coil-encompassed volume accessible by the subject, with 1-cm spacing to adjacent coil boundary, is outlined by the black dashed line; this volume is defined as the coil effective volume and used for averaging B_1^+ . Breast and chest are outlined by the red long-dashed line. Local discontinuity of B_1^+ appears at the skin-to-air boundary. (d) Right breast of prone position Ella model is positioned inside breast coil for unilateral RF excitation, with the coil boundaries at least 1 cm to skin.

3.3.2 Simulation parameters

The RF coil is positioned around the right breast, with a minimum spacing of 1 cm from adjacent tissue, at a fixed height of approximately 1 cm above the chest wall of Hanako or Ella. Detailed Yee cells, set from 0.5 to 1 mm, surround the RF coil and are edge-aligned with geometric extents of the coil conductors; these detailed cells extend in three dimensions throughout the mesh and include parts of the human body. The Yee cell size for other regions is set to a maximum of 20 mm. The coil effective volume is outlined by the black dashed line in Figure 3-1; less than 95% of total RF power is absorbed in a homogeneous adipose phantom filling this volume. Thirteen 20-mm cells, approximating one quarter wavelength in free space, are included for padding. The boundary condition for the far field is set to seven perfectly matched layers. Tissue properties at 298 MHz for the Ella model and imported breast models are assigned according to the IT'IS foundation database (73), and properties of remaining tissue types unique to Hanako are assigned to source tissues as detailed by Nagaoka (55). The EM simulation convergence criterion for a sinusoidal current feed is set to -50 dB (or 0.316%), based on the dissipation of additional frequencies introduced during the ramp-up period of the sinusoidal wave.

3.3.3 SAR calculation

The 10-g SAR Sensor is enabled in XFDTD for calculating the 10-g averaged SAR values within tissue utilizing the methods outlined by IEEE standard C95.3-2002 (80). Following successful completion of the simulation, steady-state B_1^+ , raw SAR and 10-g SAR are imported into MATLAB for calculating the average B_1^+ (in μT) within the tissue in the coil effective volume, i.e., $B_{1^+}^{\text{mean}}$, and power dissipated to different tissue types. According to IEC60601-2-33, the partial body SAR is calculated as the total power absorbed in the coil effective volume divided by the total tissue mass in the coil effective volume. SAR values are normalized by $|B_1^+|^2_{\text{mean}}$ producing normalized SAR in $\text{W/kg}/\mu\text{T}^2$. Reviewing the 7T breast MRI literature, we computed TR-averaged B_1^+ values of 0.13 μT for fat suppression with 8° tip angle and 4-ms TR (68,69), 0.6 μT with an RF-intensive imaging protocol with 20 μT applied with 3% RF duty cycle (38), and 3.6 μT for WALTZ-16 proton decoupling of 18 μT applied with 20% RF duty cycle (70). Based on these practical TR-averaged B_1^+ values, we scale the output of raw SAR, 10-g averaged SAR, and partial body SAR to a moderate B_1^+ value of 1.5 μT .

3.3.4 Thermal simulation

Whole-body thermal simulation is performed in XFDTD using the same gridding from the EM simulation. The heat transfer equation solved adheres to the Pennes bioheat equation (81), with an additional heating term due to the RF dissipated power in tissue (82). The ambient (air) temperature is set to 25 °C, and the perfusion medium is blood at 37 °C. Both initial and final temperatures are calculated from the steady-state solution of the heat transfer equation. Initial temperature is tissue absolute temperature without RF exposure, and final temperature is absolute temperature with addition of dissipated power in tissue due to RF exposure. The total dissipated power in tissue of the thermal simulation is set to a value corresponding to an MRI sequence with TR-averaged mean $B_1^+ = 1.5 \mu\text{T}$ within tissue inside the coil effective volume. At a similar SAR level, the steady-state solution of the Pennes bioheat equation corresponds to 30 minutes of tissue exposure to RF (83). Final temperature data are exported to MATLAB.

3.4 EM simulation results

3.4.1 Modeled breast fused on human models

Figure 3-2 shows the sagittal and axial cross sections, in the same scale, of the Ella and Hanako models fused with 0.5-mm resolution breasts. Affine transformation results in the curved posterior breast portion fitting properly on the surface of the pectoral muscle and bones. The level-set method added additional SAT, depicted in blue color, to smooth the surface at the outer layer of the breast to the chest joint. Figure 3-2-d illustrates 3D surface renderings of Ella in prone position and fused to modified breast models while loaded with the unilateral RF coil for EM and thermal simulation. Figure 3-1-a-c shows the B_1^+ profile of a loaded breast coil in the three principal anatomical planes. A slight discontinuity of B_1^+ appears along the boundary between air and skin tissue, owing to surface currents on the skin. The volume RF transmit coil B_1^+ is distributed homogeneously (-20 to -29 dB) within the extended volume encompassed by the breast coil.

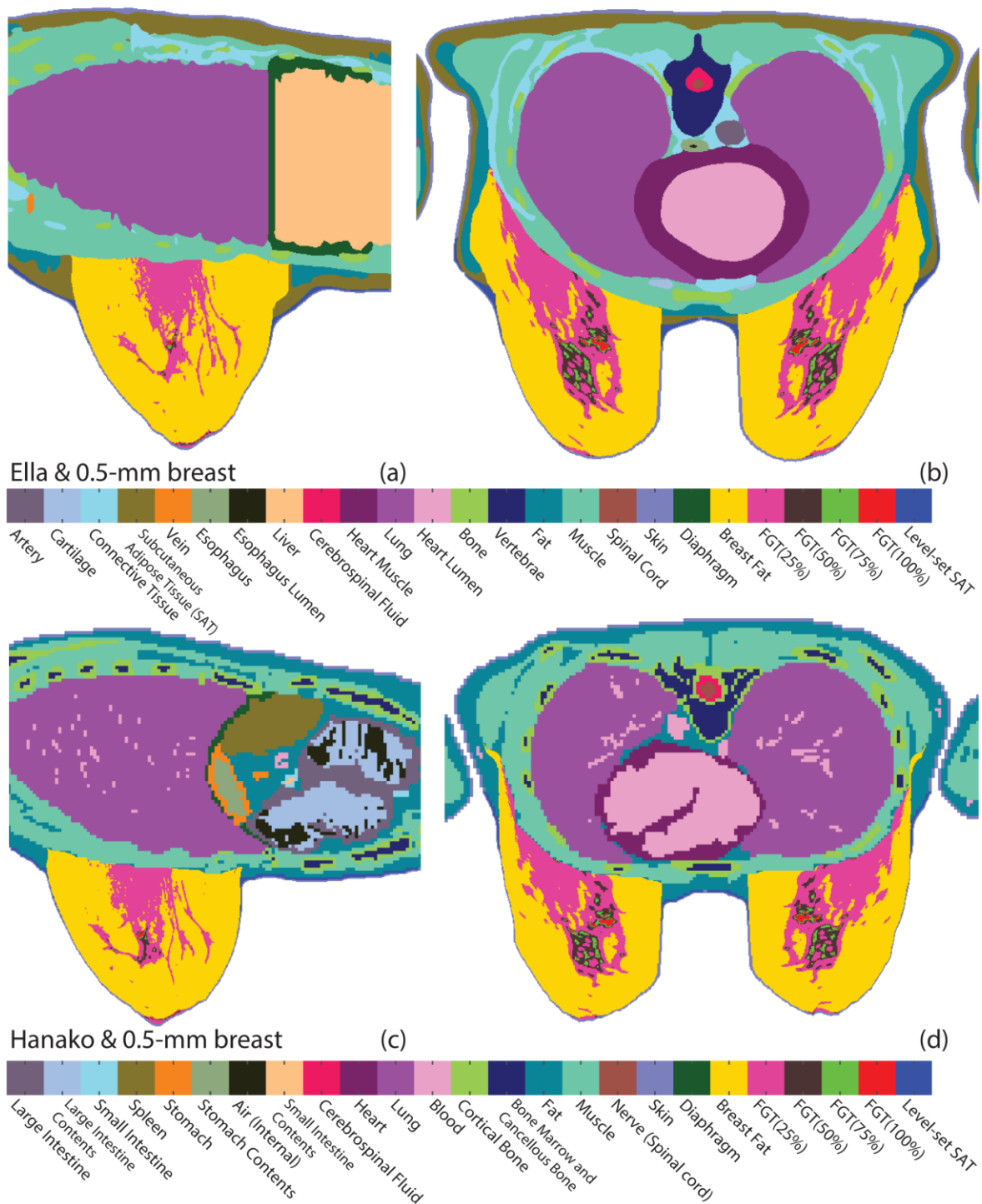


Figure 3-2. Bilateral breasts (0.5 mm resolution) fused to whole-body models. Sagittal (a) and axial (b) view of bilateral breasts fused to Ella (0.5 mm resolution); (c,d) the same set of bilateral breasts are fused to Hanako (2 mm resolution). The modified breast models are assigned a higher meshing priority and consequently overwrite the chest region of the whole-body models. Tissue added by the level-set method is designated Level-set subcutaneous adipose tissue (SAT) and colored blue.

3.4.2 SAR and temperature rise in breast

Figure 3-3 illustrate the sagittal slices of raw SAR and tissue temperature rise of four BI-RADS-category breasts. Sagittal slices of the raw and 10-g SAR and the local tissue temperature rise of all simulation cases are presented with the online version of this article as Supporting Figures B-1,2,3, respectively; corresponding axial slices are presented in Supporting Figures B-4,5,6. Figure 3-3-A shows breasts fused with Ella, and Figure 3-3-B shows breasts fused with Hanako. Figure 3-4 illustrate the sagittal slices of raw and 10-g SAR and the local tissue temperature rise of breast models of 0.5-mm and 2-mm voxel resolution fused with Hanako, with the same 0.5-mm breast model fused to Ella for comparison. In Figures 3-3 and Figure 3-4, skin and FGT have high raw-SAR level compared to the remaining breast tissue owing to their high conductivity. FGT of relatively high SAR levels branches out from regions near the nipple toward the chest, with SAR levels gradually attenuated near the pectoral muscle wall. In Figures 3-3, BI-RADS a, b, c and d breasts show ascending values of FGT%, raw and 10-g SAR and local tissue temperature rise.

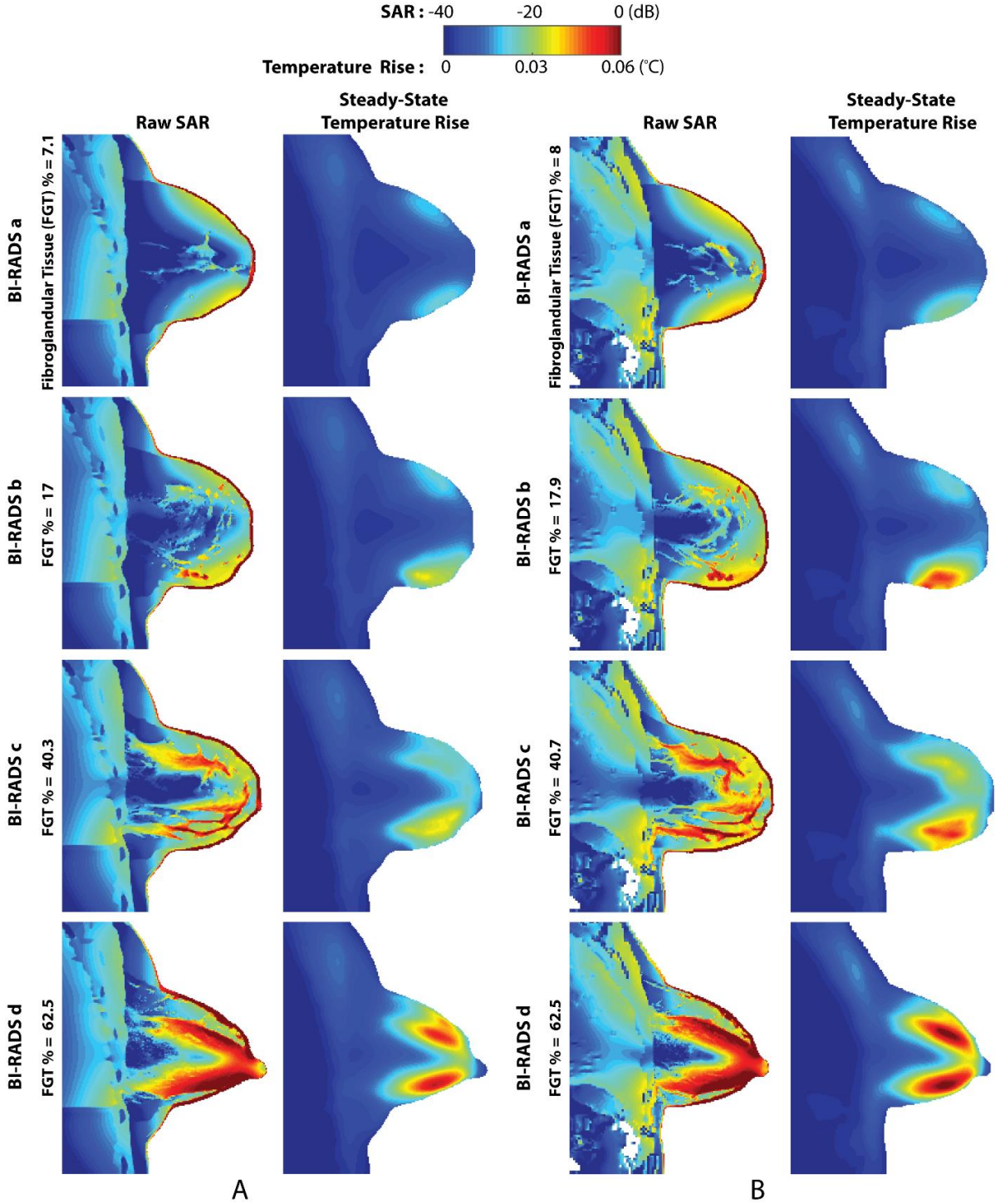


Figure 3-3. Sagittal plots of raw SAR and temperature rise with four BI-RADS-categorized breasts fused to Ella (**A**) and Hanako (**B**). Raw SAR and temperature rise when tissue temperature reaches the steady-state are quantified at mean $B_1^+ = 1.5 \mu\text{T}$ within breast tissue at 7 T. Each row represents a simulation case of one BI-RADS category, and corresponding FGT% is reported. All plots are taken from the sagittal plane across the coil center in a field of view of 22 cm (height) by 19 cm (width). Raw SAR 0 dB = 1.3 W/kg.

In Figure 3-4, the Hanako 2-mm resolution breast skin with relatively high SAR levels is thicker compared to Ella and Hanako 0.5-mm breast skin. In Figure 3-3-B and Figure 3-4, the blank areas in the Hanako body represent internal air in the large intestine. The breast models in Figure 3-4 included chest wall tissues in the posterior portion that were unable to be segmented from the CT images; thus, these regions remained in the breast models and appear heightened in the raw SAR image in Figure 3-4.

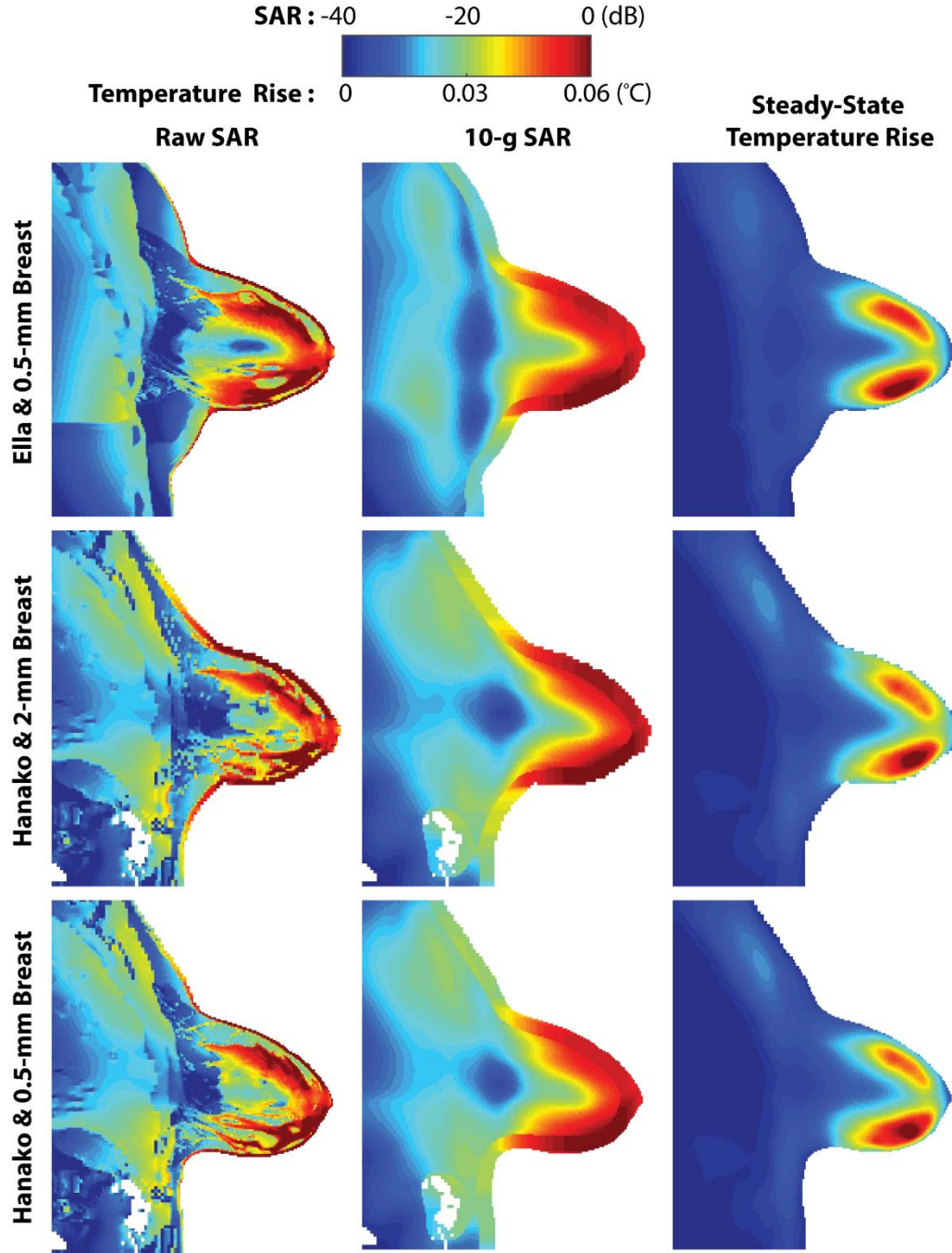
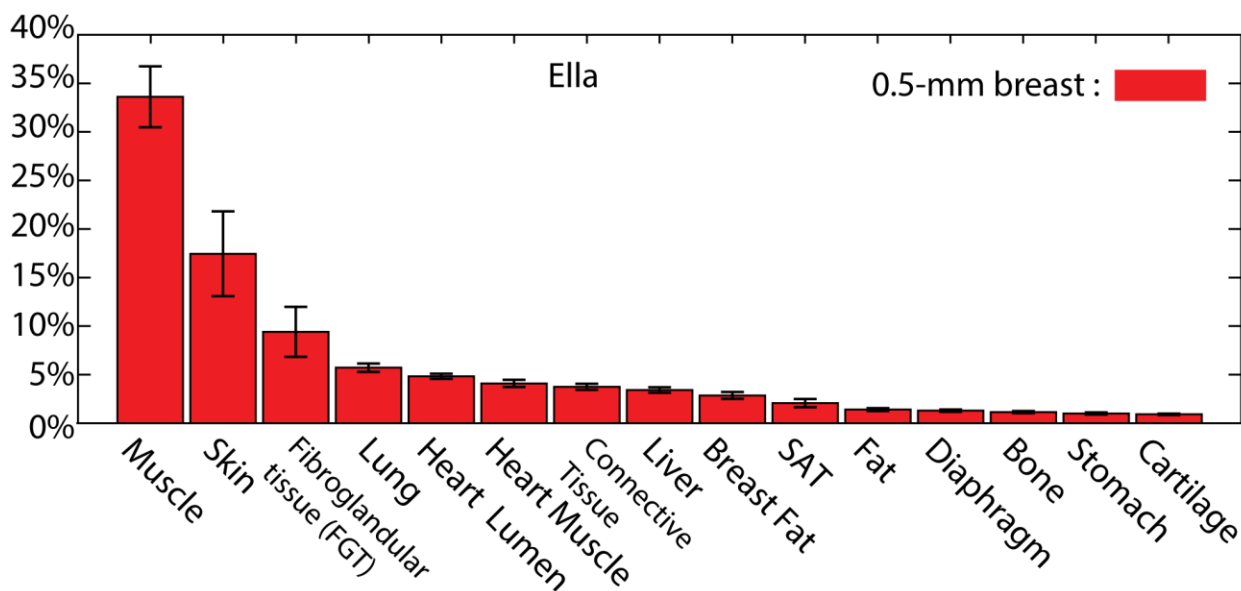


Figure 3-4. Sagittal plots of raw SAR, 10-g averaged SAR, and temperature rise with the same set of bilateral breasts, but of different voxel resolution, fused to Ella and Hanako. SAR and temperature rise when tissue temperature reaches the steady-state are quantified at mean $B_1^+ = 1.5 \mu\text{T}$ within breast tissue at 7 T. Both the top and bottom rows include breast models with 0.5-mm resolution, while the middle row includes the same breast models at 2-mm resolution. This breast was categorized as BI-RADS d, and the FGT% is 47.6 for Ella and 50.4 for Hanako. All plots are taken from the sagittal plane across the coil center in the same field of view of 22 cm (height) by 19 cm (width). SAR 0 dB = 1.3 W/kg. Internal air in the large intestine of Hanako results in the blank internal regions of raw SAR.

3.4.3 Power deposition in various tissue

Figure 3-5 shows the power deposition in tissue as a percentage of the same net power dissipated in Ella and Hanako. Muscle, skin, FGT, lung, heart, liver, and adipose tissue contain most dissipated power in both models. In addition, connective tissue (cyan labeled tissue in the Ella model in Figure 3-2) contained high percentage of dissipated power in Ella, while blood (pink labeled tissue in heart lumen of Hanako model in Figure 3-2) contained high percentage of dissipated power in Hanako. Breast fat has a mean value of 3% power dissipation, and FGT has a mean value of 9% in both 0.5-mm resolution Ella and Hanako breasts. In the 2-mm resolution Hanako breasts, the mean dissipated power in skin is significantly higher, while the mean dissipated power in FGT is slightly lower as compared to 0.5-mm resolution breasts.

Percentage of Power Dissipation



Percentage of Power Dissipation

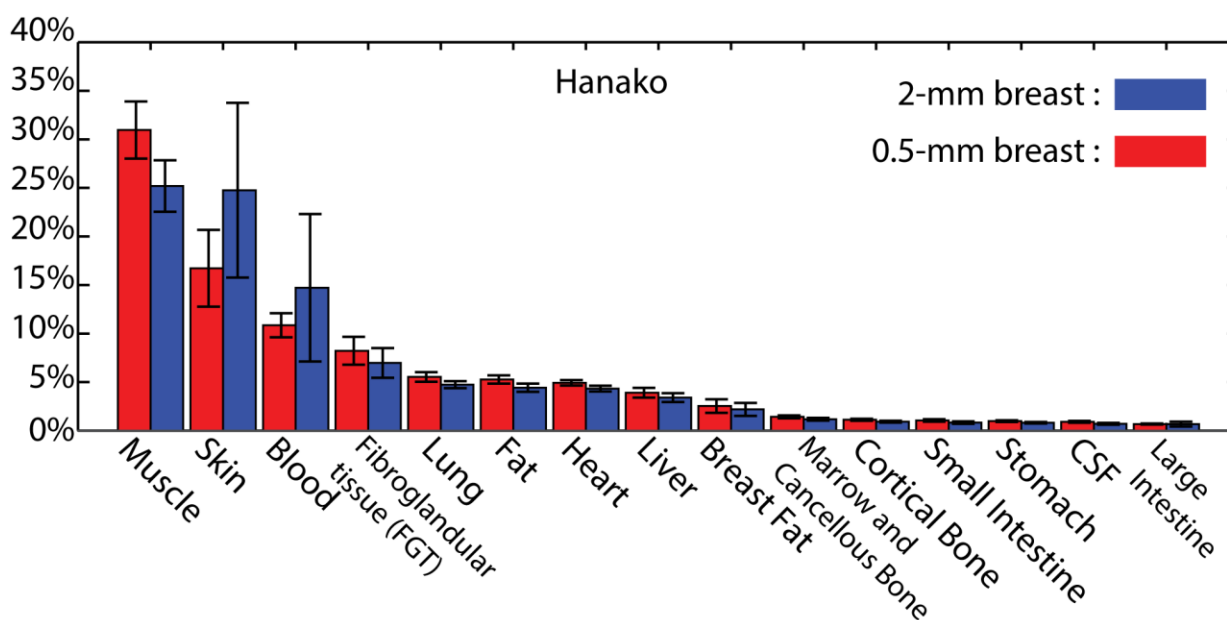


Figure 3-5. Mean power deposition percentage in tissues with the same net power dissipated under RF exposure in Ella (top) and Hanako (bottom). The same sample size of 0.5-mm and 2-mm resolution breasts are plotted in the bottom bar graph. Error bars demonstrate data distributed within one standard deviation.

3.4.4 FGT % increases SAR and temperature rise

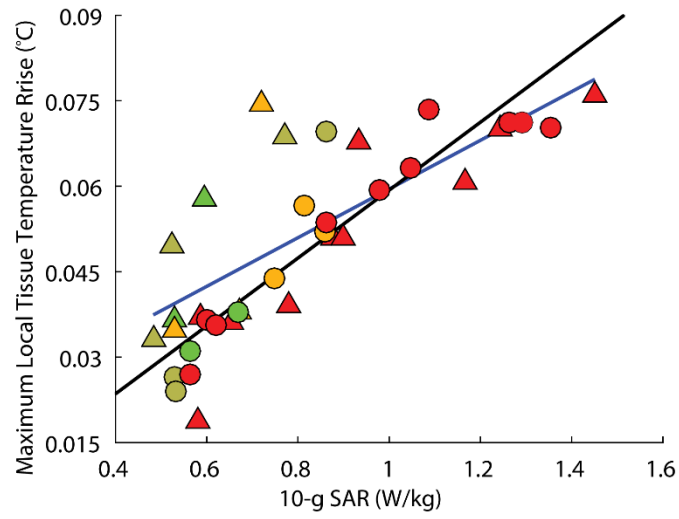
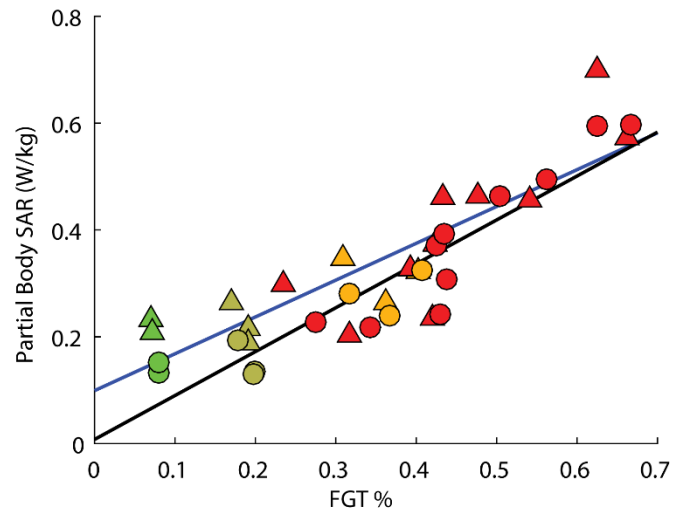
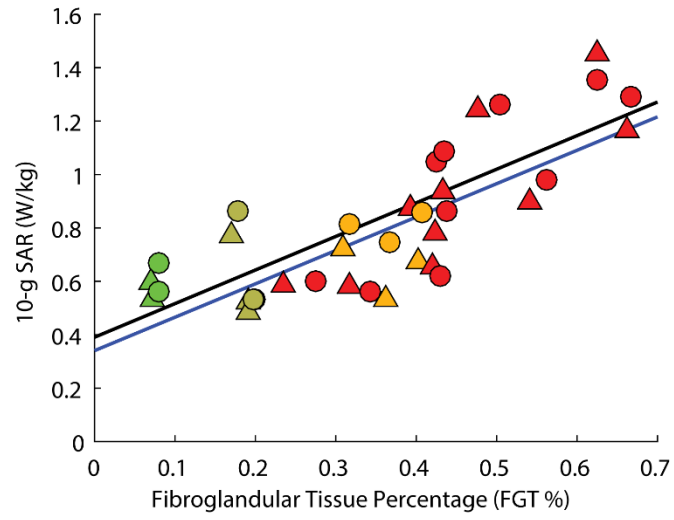
Figure 3-6 shows the plot of the maximum 10-g averaged SAR as a function of FGT%, the plot of partial body SAR as a function of FGT%, and the plot of maximum local tissue temperature rise (i.e., the maximum temperature rise of tissue within the coil effective volume) as a function of the maximum 10-g averaged SAR for Ella and Hanako 0.5-mm resolution breasts. For comparison of 10-g averaged SAR, partial body SAR, and temperature rise values among BI-RADS breasts within each human model, BI-RADS a and b breasts have the lowest values; BI-RADS c have moderate values; and BI-RADS d have the highest values. Both Ella and Hanako breasts have similar slope of 10-g SAR and partial body SAR as a function of FGT%, and the maximum 10-g averaged and partial body SAR among all breasts is 1.5 and 0.7 W/kg, respectively. For both models, partial body and the maximum 10-g SAR value are positively correlated with FGT%, and the maximum local tissue temperature rise values are positively correlated with the maximum 10-g averaged SAR value. There is stronger linear regression between the maximum local tissue temperature rise and the maximum 10-g SAR value in Hanako model as compared to Ella model, as the R^2 values are 0.85 in Hanako and 0.49 in Ella model. This implies the difference between Hanako and Ella anatomy may contribute to variance in bioheat thermal simulation results. Based on the bioheat simulation methodology in XFDTD, the simulated final tissue temperatures within human models are below 37.6 °C, and the simulated tissue temperatures within breast tissue in the effective coil volume are below 37.2 °C. Neither of the mentioned tissue temperatures increase as breast FGT% increases.

The transmit efficiency for each breast phantom simulation case is shown in Table 3-2. The transmission efficiency is calculated as mean B_1^+ within breast tissue inside the coil effective volume divided by the square root of the net input power. Comparably, the transmit efficiency of the quadrature coil reported by van de Bank et al. was $0.9487 \mu\text{T}/\sqrt{W}$, given 30 μT within breast tissue and input power of 1 kW (12).

Table 3-2. Transmit efficiency for each breast phantom simulation case

Ella		Hanako	
Fibroglandular Tissue (FGT) [%]	Transmit Efficiency [$\mu\text{T}/\sqrt{\text{W}}$]	Fibroglandular Tissue (FGT) [%]	Transmit Efficiency [$\mu\text{T}/\sqrt{\text{W}}$]
7.1	1.24	8	1.22
7.1	1.16	7.9	1.19
17	1.15	17.9	1.19
19.1	1.23	20	1.21
19.2	1.26	19.7	1.28
23.4	1.28	27.5	1.29
31	1.13	31.7	1.15
31.6	1.19	34.3	1.24
36.3	1.26	36.6	1.23
39.2	1.17	42.6	1.25
40.3	1.03	40.7	1.11
41.9	1.15	43.8	1.23
42.4	1.09	42.9	1.2
43.3	1.08	43.4	1.15
47.6	1.15	50.4	1.2
54.2	1.06	56.2	1.1
62.5	1.16	62.5	1.17
66.2	1.08	66.6	1.14

Figure 3-6. Plots illustrating correlations between FGT%, SAR, and temperature rise for Ella and Hanako breasts. Top plot shows the maximum 10-g averaged SAR values versus FGT%. Middle plot shows the partial body SAR versus FGT%. Bottom plot shows maximum local tissue temperature rise (at steady state) versus maximum 10-g averaged SAR values. All breast phantoms are in 0.5-mm resolution. Linear regression is used to fit Ella and Hanako breasts data separately; the blue regression line is for Ella, and the black line is for Hanako. The R^2 values for 10-g averaged SAR as a function of FGT%, partial body SAR as a function of FGT%, and temperature rise as a function of 10-g averaged SAR are 0.61, 0.70, and 0.49 for Ella, and 0.63, 0.86, and 0.85 for Hanako, respectively. All breast models are color-labeled according to their BI-RADS category.



Ella : BI-RADS a ▲ BI-RADS b ▲ BI-RADS c ▲ BI-RADS d ▲
 Hanako : BI-RADS a ● BI-RADS b ● BI-RADS c ● BI-RADS d ●
 Regression Line Ella : —
 Regression Line Hanako : — $|B_1^+|_{\text{mean}} = 1.5 \mu\text{T}$

3.5 Role of FGT % and various tissue on SAR and temperature

The simulated partial body SAR and local temperature obey the IEC60601-2-33 constraints for a volume transmit coil at normal operating mode. Furthermore, since local breast transmit coils are also utilized at 7 T (17,18,68), we provided 10-g averaged SAR results to facilitate comparison, and our simulation results also fulfill the 10-g averaged SAR constraints for local transmit coils. Breast transmit coils, as opposed to a whole-body transmit coil, will be necessary for potential future clinical adoption of 7T breast MRI. While the presented SAR and temperature results corresponding to a time-average B_1^+ of 1.5 μ T are well below recommended limits, it is important to note SAR increases proportionally with the square of B_1^+ . Furthermore, while temperature will increase proportionally to SAR for short exposure durations, new temperature simulations would be required for different time-average B_1^+ . Since the practical safety hazard from RF energy deposition is manifested by the thermal dose, not total power deposition, it is notable that dense breasts may be more vulnerable to local temperature increases. Adequate airflow during prone breast imaging can play a critical role in skin cooling (84).

3.5.1 FGT % increase SAR level

Our results show FGT%, BI-RADS breast composition categories, and human model resolution are important factors affecting SAR and thermal distributions. As shown in Figure 3-6, models of BI-RADS a, b, c and d breasts have FGT% in ascending order. Since FGT has the highest conductivity among breast tissues, both 10-g averaged SAR and partial body SAR values are positively correlated with breast FGT contents. This result is congruent with the transmit efficiency data presented in Table 3-2, with a general trend of higher FGT% requiring greater transmit power. In addition, FGT will experience temperature rise given its higher metabolic rate and greater vascular perfusion compared to adipose tissue. As shown in Figure 3-4, 2-mm Hanako breast skin is thicker than 0.5-mm breast skin at a detailed meshing scheme (e.g., 0.5-1.0 mm mesh) in FDTD simulation, due to the larger voxel length of 2-mm resolution breasts as compared to 0.5-mm resolution breasts. Hence, power dissipation in skin of 2-mm Hanako breasts are higher than in skin of 0.5-mm Hanako breasts as illustrated in Figure 3-5. Additionally, as 2-mm resolution breast models fused with Hanako are down-sampled four-fold as compared to 0.5-mm Hanako breasts, detailed FGT structures in breasts are not reserved, which results in loss of FGT-adipose

mixture of high FGT% (e.g., 75% FGT-25% adipose mixture). Therefore, Figure 3-5 illustrates higher power dissipation in 0.5-mm Hanako breasts as compared to 2-mm Hanako breasts. On the other hand, the power dissipation in the FGT and breast fat is similar in both Ella and Hanako with 0.5-mm breasts.

In practice, safety simulations must include the specific RF coil design being used in the imaging study, as coils may differ in transmit efficiency and produce unique \mathbf{B}_1^+ and \mathbf{E} field patterns. Notably, we previously compared a quadrature breast coil of two orthogonal loops, akin to that utilized in (17,18,67), with the Helmholtz and saddle pair used in this study; our results reported in (85) illustrated similar trends with respect to breast and body models and thus we exclude simulation of other RF coils in this paper. Furthermore, the whole-body transmit coils utilized at 1.5 and 3 T may be modeled with the fused phantoms presented herein; preliminary results utilizing the FDTD EM solver in the Sim4Life software package (Zurich MedTech AG, Zurich, Switzerland) are presented in (86).

3.5.2 Maximum tissue temperature rise

The observed maximum tissue temperatures based on the XFDTD thermal simulation are below 37.6 °C. In addition to XFDTD, the Pennes bioheat equation is also applied for the thermal simulation in Sim4Life version 3.4. In both cases, the blood temperature is constant during the thermal simulation, and thus the simulation results will not account for body core temperature. The generic bioheat transfer model (GBHTM) takes into account spatial and temporal blood temperature variation due to RF heating. Comparisons between in vivo and in silico data show the temperature results based on GBHTM have better fitting, while the temperature reported from the Pennes bioheat equation shows less fitting with in vivo data (83).

3.5.3 Additional considerations on breast morphology

Since various shapes and anatomical structures of breasts exist across the population, it is difficult to define a standard breast template, which is a primary criterion used for image registrations. In contrast to image registration, the level-set method can preserve the original structures of the middle and anterior portions of breast models as well as whole-body human models. The level-set function discussed in this paper is regularized by the surface curvatures of

both the human models and the breast models. Considering that recreating natural-appearing breast surface curvatures is considered the gold standard for breast reconstruction surgery (87–89), the fusion method presented here produces models that are analogous to the actual population.

4. EM SIMULATION OF A 16-CHANNEL HEAD TRANSCIEVER AT 7 T USING CIRCUIT-SPATIAL OPTIMIZATION

The recent regulatory clearance for the 7T MRI system has led to increased interest in clinical ultra-high field UHF applications (38,90–92). However, to robustly achieve the expected increase in SNR at UHF, the RF challenges need to be met, namely, problems with higher RF power (4), worse B_1^+ inhomogeneity (38,90,93,94), and increased tissue permittivity and conductivity at higher frequency, all of which usually results in increased SAR (6,22,51,94). The parallel transmission (pTx) coils and techniques are generally accepted as a realistic solution (5,22–25), providing improvement in the B_1^+ spatial homogeneity with good RF efficiency while reducing peak local SAR (26,27). In the development of such pTx coils, the need for accurate EM simulations for RF safety and performance design is evident. Over the past several years, the state-of-the-art for design and simulation of such coil arrays has advanced, e.g., Kozlov and Turner (28) described the circuit-domain co-simulation strategy to use the S-parameters from a single EM simulation with RF circuit analysis for coil tuning and matching thereby saving significant time. More specifically, Zhang (29) and Lemdiasov (30) described calculation of a closed-form S-parameter matrix to accomplish these simulations. These methods have been used to improve the prediction of local SAR in pTx coils (26,31) at 3 T, 7 T (32) and 10.5 T (33).

A key aspect of the use of pTx arrays has been the coil interactions, which become more severe at higher frequency. In order to minimize these couplings, several approaches (27,95–100) have been proposed including capacitive decoupling, inductive decoupling, and other methods such as induced current elimination (ICE), resonant inductive decoupling (RID), and dipole-loop decoupling. These methods range from geometric overlap to additional secondary resonant circuits that can minimize both real and imaginary terms in the impedance matrix. It is clear however that independent of the specific methodology of decoupling, given the decoupling circuit's effect on power distribution, it is important to include its impact in the EM simulation and circuit analysis. However, with the simulation tools available, solutions that include the decoupling circuits have been less discussed. The dual-row head coil modeled by Adriany (101) and Hoffmann (102) included transformer decoupling (TD) circuits modeled using the built-in toolbox offered in CST Microwave Studio 2018. However, more complex features, such as the Q factor and isolated

resonant frequency of the TD circuits, are not well modeled and optimized in the EM simulation or circuit analysis software (103).

In this work, we establish methods to assist in the design and optimization of a decoupled transceiver array for the human head. Based on the double row transceiver array as described by Avdievich (104–106), we introduce a closed-form S-parameter matrix of the transceiver that accounts for the matching circuits, decoupling circuits, and lumped capacitors. We implement a hybrid circuit-spatial domain analysis that uses a target cost function which includes both the S-parameters and B_1^+ homogeneity to determine coil parameters, including capacitors, inductors, and decoupling circuits' Q factors, isolated frequencies, and coupling coefficients. Over a series of four simulated head models and an input range of coil parameters determined from real experience, this hybrid circuit-spatial domain analysis obtains excellent agreement of optimized components. Finally, using the applied amplifier voltages from the MRI console, we generate B_1^+ profiles from individual coils which show good agreement with the in vivo data.

4.1 Method

4.1.1 Simulation set-up

The double row array coil was modeled in XFDTD (v7.7, Remcom, State College, PA) in 1-mm nominal cell resolution as shown in Figure 4-1-A. The cylindrical RF shield is made by two layers of overlapped slotted copper foil that are insulated from each other using a thin liquid crystal polymer layer ($\epsilon_r=2$). The slotted copper foil enhances the TEM waves inside the RF coil and thus improves the B_1^+ field (107). The coil former is modeled as polycarbonate ($\epsilon_r=3$), and the board material of the coil is Bakelite ($\epsilon_r=3.5$). The volume enclosed by the RF shield is meshed with 1-mm resolution gridding; the rest of the space (including the human body and simulation paddings) are meshed with gridding resolution of at least 20 cells per wavelength. The Japanese head model Hanako (2-mm resolution adult female) (108), two Virtual Family models Ella (v1.3 1-mm resolution 26 year old female) and Duke (v1.3 1-mm resolution 34 year old male) (109), and the Virtual Population model Louis (v1.3 1-mm resolution 14 year old male) (110) were loaded separately in the coil center, with coil-to-tissue distance greater than 1 cm. A broadband excitation with convergence criterion of -50 dB resulted a simulation time of 14 minutes per voltage port of

a multi-port simulation, running on an Intel Xeon workstation with 64 GB RAM and two Quadro K5200 GPU.

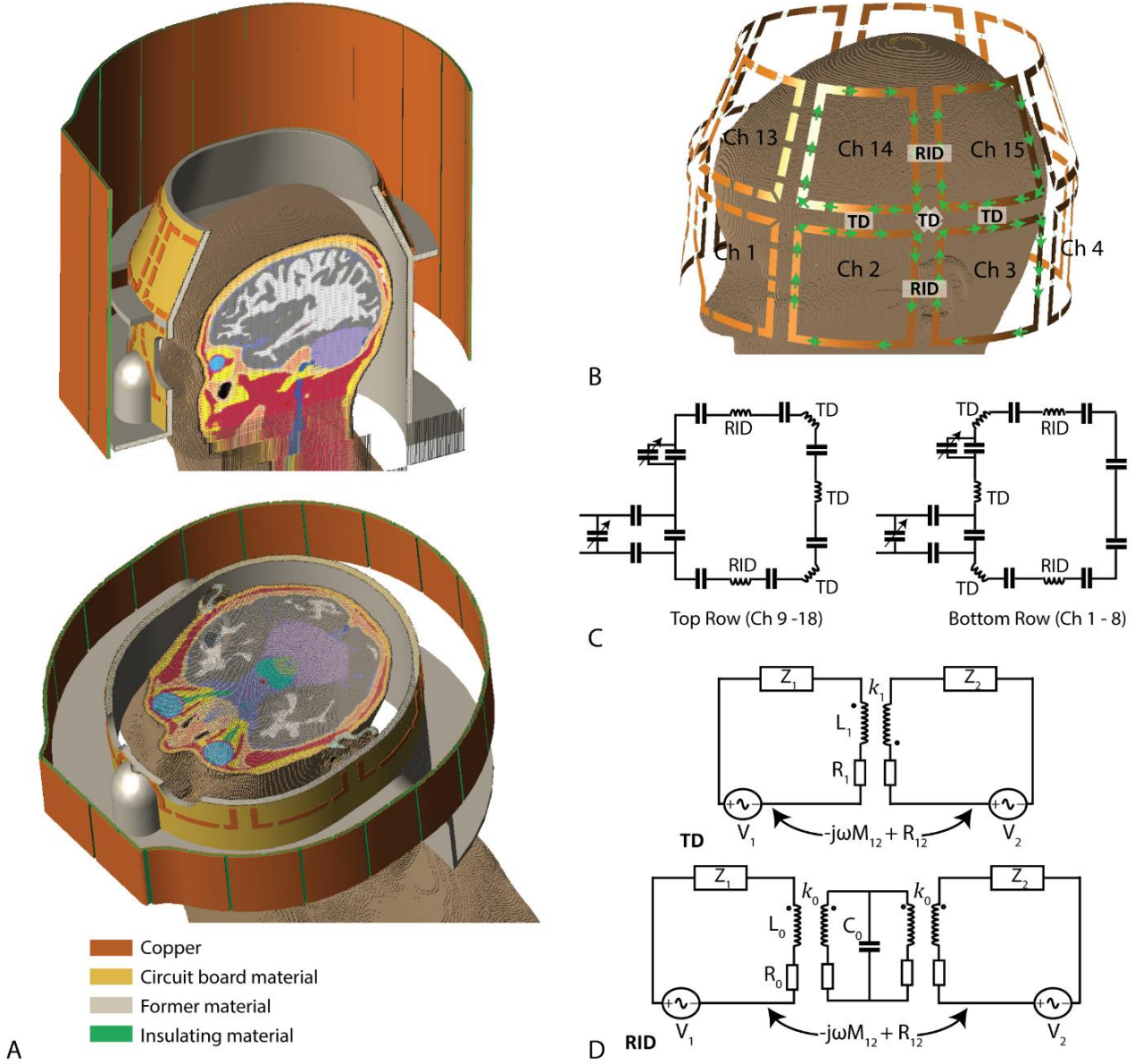


Figure 4-1. **A:** The coil set up. A slotted RF shield is placed outside the array coil. The dual-row coil is made with a former and covered with copper clad board. The simulated human models are positioned in the coil center, with the eyes aligned with the eye portals on the coil former, mimicking the real scanning scenario. **B:** The 1-V, 50- Ω voltage feeds orientations in the XFDTD setup for the $\mathbb{C}^{208 \times 208}$ S-parameters calculation. The arrow points to the current flowing direction. The circuit diagrams of the top and bottom row loop coils are shown in **C**. The RID and TD circuits are shown in **D**. There are 16 RID circuits applied to decouple neighboring coils in the horizontal direction, 8 vertical TD circuits applied to decouple neighboring coils in the vertical direction, and 16 diagonal TD circuits applied to decouple neighboring coils in the diagonal direction.

4.1.2 S-parameters relationship

The array coil (Figure 4-1) has 208 gaps distributed along the loops and is described by 296 parameters (a listing is shown in Table 4-1, first column).

Table 4-1. Mean \pm standard deviation of key components of the 296 optimized parameters.

Components	Hanako	Hanako (exclude B_1^+ inhomogeneity)	Ella	Duke	Louis
$x_1 - x_{96}$ Fixed lumped caps ("10 pF" or "8.2 pF") Optimization subject to $x_{1-96} \in [7, 13 \text{ pF}]$	9.66 \pm 1.24	9.52 \pm 0.87	9.66 \pm 0.91	9.53 \pm 0.85	9.69 \pm 0.87
$x_{105} - x_{112}$ Tuning cap, top coils [10, 20 pF]	14.19 \pm 0.85	13.75 \pm 0.50	14.80 \pm 0.24	14.19 \pm 0.40	14.37 \pm 0.56
$x_{97} - x_{104}$ Tuning cap, bottom coils [10, 20 pF]	15.70 \pm 1.53	15.11 \pm 0.45	15.43 \pm 0.39	15.52 \pm 0.71	15.03 \pm 0.55
$x_{121} - x_{128}$ Trimmer cap, matching, top coils [5, 20 pF]	5.56 \pm 0.30	7.28 \pm 0.70	6.58 \pm 1.01	6.61 \pm 1.05	6.02 \pm 0.46
$x_{113} - x_{120}$ Trimmer cap, matching, bottom coils [5, 20 pF]	10.84 \pm 2.33	7.82 \pm 0.51	8.39 \pm 2.21	6.97 \pm 1.08	7.72 \pm 1.29
$x_{129} - x_{144}$ Shunt matching cap [5, 20 pF]	6.22 \pm 0.82	6.53 \pm 0.56	6.38 \pm 0.79	5.92 \pm 0.43	6.18 \pm 0.47
$x_{145} - x_{160}$ Parallel matching cap [5, 25 pF]	18.93 \pm 4.08	19.55 \pm 0.58	19.93 \pm 2.24	20.16 \pm 2.69	20.14 \pm 2.34
$x_{161} - x_{168}$ RID inductor, top coils [5, 15 nH]	9.91 \pm 1.05	9.34 \pm 1.42	9.37 \pm 0.90	10.00 \pm 1.46	9.55 \pm 1.42
$x_{169} - x_{176}$ RID inductor, bottom coils [5, 15 nH]	11.50 \pm 1.20	9.49 \pm 1.49	10.31 \pm 1.06	11.35 \pm 1.30	10.18 \pm 1.63
$x_{201} - x_{216}$ RID isolated frequency [200, 298 MHz]	290.27 \pm 2.0 2	292.64 \pm 0.8 7	291.48 \pm 1.0 2	290.44 \pm 1.6 4	291.46 \pm 1.7 2
$x_{241} - x_{256}$ RID Q factors [150, 350]	235.46 \pm 22. 06	216.98 \pm 15. 90	238.24 \pm 9.2 3	245.25 \pm 16. 26	236.94 \pm 17. 22
$x_{281} - x_{296}$ RID k coefficients [0.06, 0.5]	0.282 \pm 0.02 9	0.257 \pm 0.01 9	0.279 \pm 0.01 4	0.295 \pm 0.02 1	0.280 \pm 0.02 4
$x_{177} - x_{184}$ TD vertical inductors [5, 20 nH]	17.93 \pm 0.49	18.47 \pm 0.33	17.81 \pm 0.26	17.93 \pm 0.29	17.79 \pm 0.32
$x_{185} - x_{200}$ TD diagonal inductors [5, 20 nH]	8.29 \pm 1.38	9.98 \pm 0.78	8.77 \pm 1.53	9.77 \pm 2.99	8.97 \pm 1.72
$x_{217} - x_{240}$ TD Q factors [150, 350]	249.95 \pm 3.3 2	247.76 \pm 1.5 9	249.02 \pm 1.8 8	250.02 \pm 1.4 2	248.92 \pm 1.9 7
$x_{257} - x_{264}$ TD vertical k coefficients [0.06, 0.5]	0.424 \pm 0.01 7	0.441 \pm 0.01 4	0.435 \pm 0.01 2	0.416 \pm 0.01 6	0.433 \pm 0.01 4
$x_{265} - x_{280}$ TD diagonal k coefficients [0.06, 0.5]	0.243 \pm 0.01 8	0.255 \pm 0.01 3	0.256 \pm 0.01 1	0.259 \pm 0.02 3	0.255 \pm 0.01 6

The voltage feeds are bridged across the gaps in the orientation as shown in Figure 4-1-B, with each voltage feed set to 1 V, 50 Ω with modulated Gaussian wave excitations. In the circuit-domain, this array can be modeled as a network of 208 ports, with 16 ports connected to the matching circuits, and 192 ports connected to 112 lumped capacitors and 40 decoupling circuits (using 2 ports each). At a given frequency, the $\mathbb{C}^{208 \times 208}$ S-matrix is

$$\mathbf{S}_{\text{CoilPorts}} = \begin{bmatrix} \mathbf{S}_{\text{drive drive}} & \mathbf{S}_{\text{drive lump}} \\ \mathbf{S}_{\text{lump drive}} & \mathbf{S}_{\text{lump lump}} \end{bmatrix}. \quad [4-1]$$

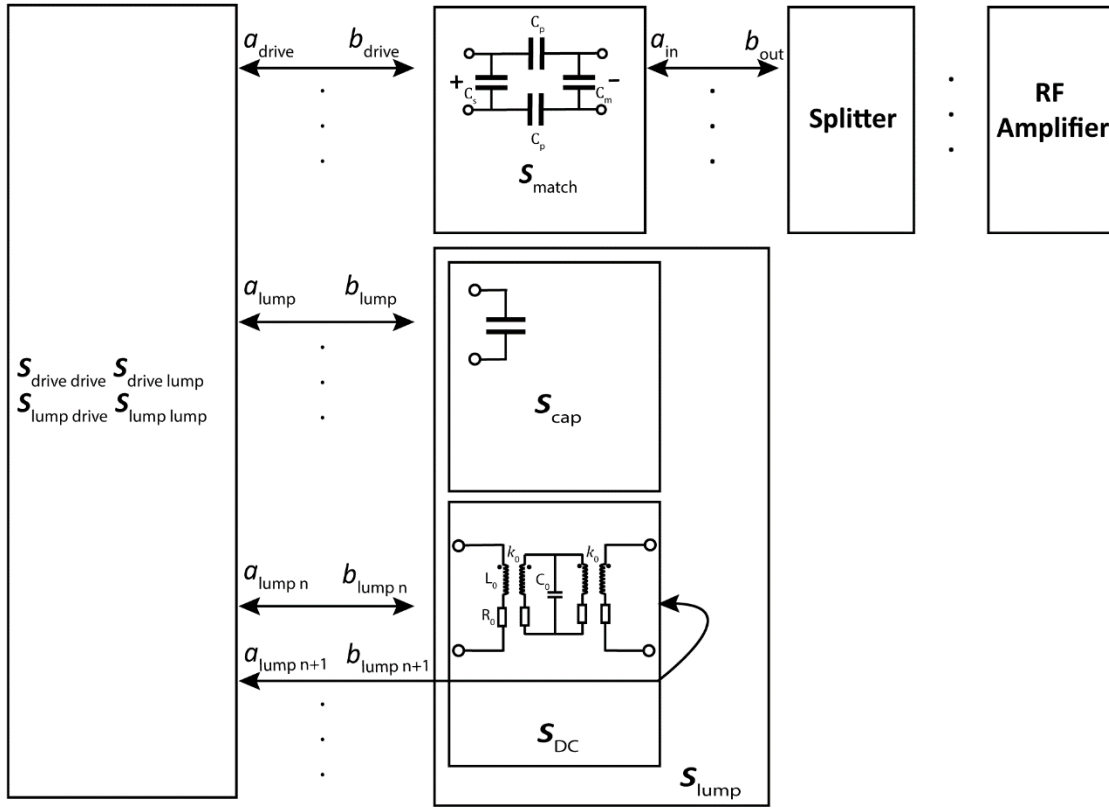


Figure 4-2. The 208-port coil as a network system. The 16 channels coming from the splitter are connected to matching circuits which are connected to the dual-row coil. The dual-row coil elements are also connected with lumped capacitors and transformers decoupling circuits.

With our experimental values for forward and reflected voltages being measured at the amplifier, in this analysis we need to describe the S-parameters at the RF amplifiers: as shown in Figure 4-2, this is defined as $b_{\text{out}}/a_{\text{in}}$ where a_{in} and b_{out} are the complex forward and reflected voltages,

respectively, between the matching circuits and amplifiers. Here we show the analysis relating the coil elements used in the optimization to the S-parameters $\mathbf{b}_{\text{out}}/\mathbf{a}_{\text{in}}$.

The forward wave to the network system is a column vector:

$$\mathbf{a} = [a_1 \quad a_2 \quad \cdots \quad a_{208}]^T = [\mathbf{a}_{\text{drive}}^T \quad \mathbf{a}_{\text{lump}}^T], \quad [4-2]$$

and the reflected waves of the network system are represented by a column vector:

$$\mathbf{b} = [b_1 \quad b_2 \quad \cdots \quad b_{208}]^T = [\mathbf{b}_{\text{drive}}^T \quad \mathbf{b}_{\text{lump}}^T], \quad [4-3]$$

where $\mathbf{a}_{\text{drive}}$ and $\mathbf{b}_{\text{drive}}$ are column vectors that contain 16 complex elements, annotated with complex vector space \mathbb{C}^{16} . $\mathbf{a}_{\text{drive}}$ and $\mathbf{b}_{\text{drive}}$ represent the forward and reflected waves connected to the driving ports on the coils, respectively. \mathbf{a}_{lump} and \mathbf{b}_{lump} are of \mathbb{C}^{192} , representing the forward and reflected waves to the lumped capacitors and decoupling circuits ports. The overall relationship of all ports is:

$$\begin{bmatrix} \mathbf{S}_{\text{drive drive}} & \mathbf{S}_{\text{drive lump}} \\ \mathbf{S}_{\text{lump drive}} & \mathbf{S}_{\text{lump lump}} \end{bmatrix} \begin{bmatrix} \mathbf{a}_{\text{drive}} \\ \mathbf{a}_{\text{lump}} \end{bmatrix} = \begin{bmatrix} \mathbf{b}_{\text{drive}} \\ \mathbf{b}_{\text{lump}} \end{bmatrix}. \quad [4-4]$$

The reflected waves can be represented by a function of reflection coefficients and forward waves as described by Lemdiasov (30). Eq. 4-5 relates the reflected waves in relation to both the coil array and the matching circuits:

$$\begin{bmatrix} \mathbf{b}_{\text{drive}} \\ \mathbf{b}_{\text{lump}} \end{bmatrix} = \begin{bmatrix} \mathbf{S}_{\text{match}+}^{-1} \cdot \mathbf{a}_{\text{drive}} \\ \mathbf{S}_{\text{lump}}^{-1} \cdot \mathbf{a}_{\text{lump}} \end{bmatrix} - \begin{bmatrix} \mathbf{S}_{\text{match}+-} \cdot \mathbf{S}_{\text{match}+}^{-1} \cdot \mathbf{a}_{\text{in}} \\ 0 \end{bmatrix}. \quad [4-5]$$

The $\mathbf{S}_{\text{match}+}$ and $\mathbf{S}_{\text{match}+-}$ are diagonal matrices for the 16 matching circuits: the diagonal terms are the reflection and the transmission coefficients respectively, when looking from the loop coil toward the matching circuit. In Eq. 4-5, \mathbf{S}_{lump} contains the S matrices of lumped capacitors (\mathbf{S}_{cap}) and decoupling circuits (\mathbf{S}_{DC}):

$$\mathbf{S}_{\text{lump}} = \begin{bmatrix} \mathbf{S}_{\text{cap}} & \mathbf{0} \\ \mathbf{0} & \mathbf{S}_{\text{DC}} \end{bmatrix} \quad [4-6]$$

The Appendix describes the S matrices for matching circuits ($\mathbf{S}_{\text{match}+}$, $\mathbf{S}_{\text{match}+-}$ and $\mathbf{S}_{\text{match}-}$), lumped capacitors (\mathbf{S}_{cap}) and decoupling circuits (\mathbf{S}_{DC}).

Inserting Eq. 4-5 in Eq. 4-4 gives:

$$\begin{bmatrix} \mathbf{S}_{\text{drive drive}} & \mathbf{S}_{\text{drive lump}} \\ \mathbf{S}_{\text{lump drive}} & \mathbf{S}_{\text{lump lump}} \end{bmatrix} \begin{bmatrix} \mathbf{a}_{\text{drive}} \\ \mathbf{a}_{\text{lump}} \end{bmatrix} = \begin{bmatrix} \mathbf{S}_{\text{match}+}^{-1} \cdot \mathbf{a}_{\text{drive}} \\ \mathbf{S}_{\text{lump}}^{-1} \cdot \mathbf{a}_{\text{lump}} \end{bmatrix} - \begin{bmatrix} \mathbf{S}_{\text{match}+-} \cdot \mathbf{S}_{\text{match}+}^{-1} \cdot \mathbf{a}_{\text{in}} \\ 0 \end{bmatrix}. \quad [4-7]$$

As stated, we need to determine the array S-parameters from $\mathbf{b}_{\text{out}}/\mathbf{a}_{\text{in}}$, with \mathbf{b}_{out} given by the relationship between the matching circuits' $\mathbf{S}_{\text{match}}$ parameters and $\mathbf{a}_{\text{drive}}$:

$$\mathbf{b}_{\text{out}} = \mathbf{S}_{\text{match}+-} \cdot \frac{\mathbf{a}_{\text{drive}} - \mathbf{S}_{\text{match}+-} \cdot \mathbf{a}_{\text{in}}}{\mathbf{S}_{\text{match}+}} + \mathbf{S}_{\text{match}-} \cdot \mathbf{a}_{\text{in}}, \quad [4-8]$$

where $\mathbf{a}_{\text{drive}}$ is calculated from Eq. 4-7 as

$$\begin{aligned} \mathbf{a}_{\text{drive}} = & (\mathbf{S}_{\text{match}+}^{-1} - \mathbf{S}_{\text{drive drive}} - \mathbf{S}_{\text{drive lump}} \cdot (\mathbf{S}_{\text{lump}}^{-1} - \mathbf{S}_{\text{lump lump}})^{-1} \cdot \\ & \mathbf{S}_{\text{drive lump}})^{-1} \cdot \mathbf{S}_{\text{match}+-} \cdot \mathbf{S}_{\text{match}+}^{-1} \cdot \mathbf{a}_{\text{in}}. \end{aligned} \quad [4-9]$$

Thus the $\mathbb{C}^{16 \times 16}$ S-parameters of the array coil measured at the RF amplifier is

$$\mathbf{S} = \frac{\mathbf{b}_{\text{out}}}{\mathbf{a}_{\text{in}}} = \mathbf{S}_{\text{match}+-} \cdot \mathbf{S}_{\text{match}+}^{-1} \cdot \left(\frac{\mathbf{a}_{\text{drive}}}{\mathbf{a}_{\text{in}}} - \mathbf{S}_{\text{match}+-} \right) + \mathbf{S}_{\text{match}-}. \quad [4-10]$$

To validate Eq. 4-10, the XFDTD-calculated $\mathbf{S}_{\text{CoilPorts}}$ from Eq. 4-1 was imported into the SnP (Touchstone) instance in ADS 2020 and connected with corresponding circuit models (lumped capacitors, matching circuits, and decoupling circuits). The resulting S-parameters obtained at the 16 feed ports in the ADS 2020 SnP instance are the same as the $\mathbb{C}^{16 \times 16}$ S-parameters obtained using Eq. 4-10.

4.1.3 Decoupling circuits

In the above 208-port array description, we used a lumped component description of the decoupling circuits. Figure 4-1-B shows the adjacent surface coils being decoupled using two types of decoupling circuits. Depending on the orientation, the nearest neighbor surface coils have mutual impedance $Z_{12} = -j\omega M_{12} + R_{12}$, where ω is coil resonant angular frequency $2\pi \times 298$ MHz. As shown in Figure 4-1-B, within a row (top or bottom), the horizontally adjacent coils are decoupled by RID circuits; the vertically and diagonally (“cornering”) adjacent coils are decoupled by TD circuits (Figure 4-1-D). As shown by Avdievich (45), for the RID circuit both the reactive

and resistive terms can be canceled when $\omega_0 < \omega$ while the TD eliminates the reactive term of the mutual impedance. The $\mathbb{C}^{2 \times 2}$ Z matrix of each RID circuit (\mathbf{Z}_{RID} in Appendix Eq. A7) is characterized by four variables ω_0 , L_0 , Q_0 and k_0 , representing the isolated resonant frequency, inductors, RID Q factor and coupling coefficients. Consequently, the capacitor value (C_0) and the inductor resistivity (R_0) can be determined based on $C_0 = 2/(\omega_0^2 L_0)$, and $R_0 = \omega_0 L_0 / Q_0$. The $\mathbb{C}^{2 \times 2}$ Z matrix of each TD circuit (\mathbf{Z}_{TD} in Appendix Eq. A8) is characterized by three variables L_1 , Q_1 and k_1 , representing inductors, inductor Q factor and the coupling coefficient. The inductor resistivity (R_1) of the TD circuit is given by $R_1 = \omega L_1 / Q_1$.

4.1.4 Optimization

The optimization was performed using a cost function ($f(\mathbf{x})$) defined in Eq. 4-11, where $\| \cdot \|$ denotes the Euclidean distance, $| \cdot |$ is the elementwise absolute values, and w_{1-3} are weights:

$$f(\mathbf{x}) = w_1 \| |\text{diag}(S(\mathbf{x}))| - S_{ii} \| + w_2 \| |S_r(\mathbf{x})| - S_{ij} \| + w_3 \left\| \frac{\text{Std}(B_1)}{\text{Mean}(B_1)} - \text{target} \right\|. \quad [4-11]$$

The minimum is given by the constrained optimization:

$$\hat{\mathbf{x}} = \arg \min_{\mathbf{x}} \{ f(\mathbf{x}) \},$$

over the 296 parameters, and each coil port has at least one parameter (see Table 4-1, left column for itemization for \mathbf{x}), subject to

$$\mathbf{x} \in \{\Omega: x_{n \text{ lower}} < x_n < x_{n \text{ upper}}, n = 1, 2, \dots, 296\}.$$

Eq. 4-11 contains three parts, with the first part optimizing the diagonal terms of the S-parameters $S(\mathbf{x})$ from Eq. 4-10 (denoted by $\text{diag}(S(\mathbf{x}))$) with a target value S_{ii} of -20 to -25dB. The second part is optimization of decoupling of any two adjacent coils, represented by the selected off-diagonal terms of the coil S-parameter (denoted by $S_r(\mathbf{x})$, terms are shown as $S_{ij(\text{RID bot})}$, $S_{ij(\text{RID bot})}$, and $S_{ij(\text{TD})}$ in Figure 4-3-A) with a target value S_{ij} of -20 to -30 dB; these boundary values based on experimental data. Notably, $S_r(\mathbf{x})$ are effectively defined by the TD and RID circuits (rather than the sample), so the optimization of $S_r(\mathbf{x})$ is equivalent to optimization of the TD and RID circuits. The third part is the optimization of B_1^+ inhomogeneity within the brain calculated using Eqs. 4-9,12,13,14 (see below); we used a target B_1^+ inhomogeneity of 10%. The weightings w_1 , w_2 and w_3 were set at 0.1, 0.1, and 1.5, based on obtaining equal contributions to the $f(\mathbf{x})$

minimization from the three target parameters. To avoid large matrix sizes and to save optimization time, we downsampled the B_1^+ maps from 300^2 to 64^2 resolution over the 9 slices (i.e., ~20 fold reduction in matrix size) before calculating $\text{Std}(B_1^+)$ and $\text{Mean}(B_1^+)$.

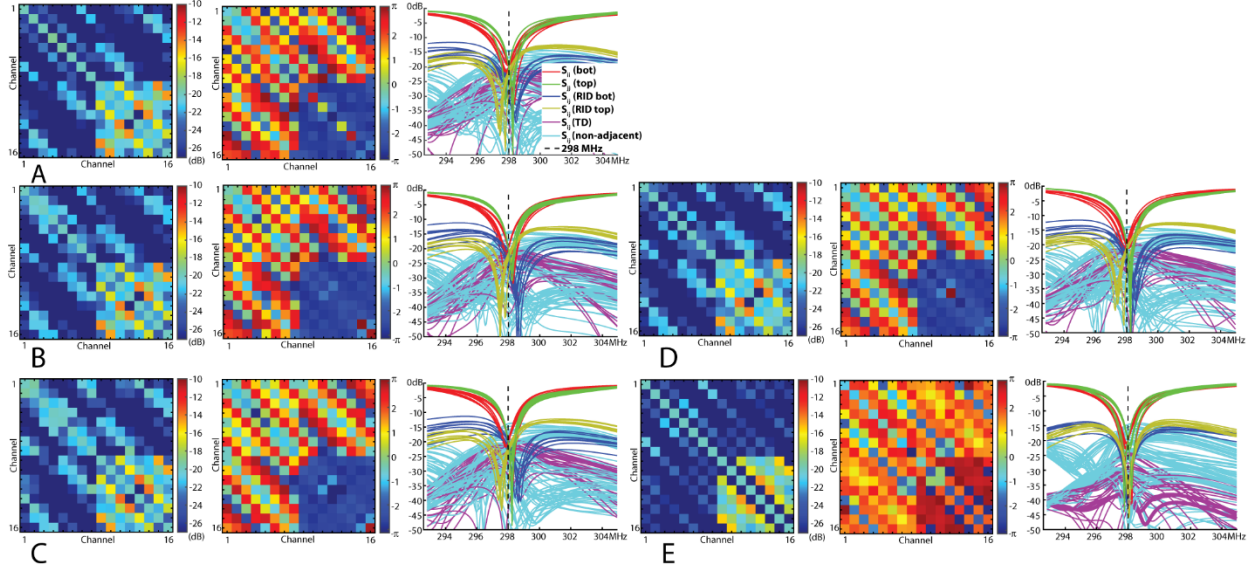


Figure 4-3. Magnitude (dB) and phase of S-parameter matrix at 298 MHz, and frequency sweep determined from cost function Eq. 4-11 (with B_1^+ homogeneity optimization) for Duke (A), Ella (B), Hanako (C), and Louis (D). Panel E shows these equivalent data for Louis but determined with Eq. 4-15, without B_1^+ homogeneity optimization.

This constrained optimization can be solved using solvers such as Self Organizing Migrating Algorithm (SOMA) (111), the alternating direction method of multipliers (ADMM) (112), Genetic Algorithm (GA) and a nonlinear programming solver ‘fmincon’. Both GA and fmincon are provided in the MATLAB Optimization Toolbox (MathWorks, Natick, MA). We used fmincon as the optimization solver and searched for optimal x parameters within the upper and lower bounds.

As shown in Table 4-1, over the four modeled heads Ella, Duke, Hanako and Louis, the constrained optimization of $f(\mathbf{x})$ gave highly consistent values for all mean component values (264 parameters associated with the RID, TD, and distributed capacitors, excluding tuning and matching circuits). These values were thus used to define the “fixed” transceiver T_0 . To mimic real-world workflow, T_0 was then used with optimization of the 32 tuning and matching capacitors (x_{97} to x_{128}) for each head to estimate field maps and RF shim.

ADMM Optimization implementation

To remove the constraint on \mathbf{x} for the cost function Eq 4-11

-11, we define the convex function:

$$g(\mathbf{x}) = \begin{cases} 0 & \text{if } \mathbf{x} \in \Omega \\ \infty & \text{if } \mathbf{x} \notin \Omega \end{cases} .$$

Then, the minimum is given by the unconstrained optimization:

$$\hat{\mathbf{x}} = \arg \min_{\mathbf{x}} \{ f(\mathbf{x}) + g(\mathbf{x}) \} .$$

We can use variable splitting to derive a constrained optimization problem that is equivalent to the above equation:

$$(\hat{\mathbf{x}}, \hat{\mathbf{v}}) = \arg \min_{\mathbf{x}=\mathbf{v}} \{ f(\mathbf{x}) + g(\mathbf{v}) \} .$$

Next, we use the augmented Lagrangian method to formulate the constrained optimization as an unconstrained optimization:

$$(\hat{\mathbf{x}}, \hat{\mathbf{v}}) = \arg \min_{\mathbf{x}, \mathbf{v}} \{ f(\mathbf{x}) + g(\mathbf{v}) + \frac{a}{2} \|\mathbf{x} - \mathbf{v} + \mathbf{u}\|^2 \} ,$$

and $\frac{a}{2} \|\mathbf{x} - \mathbf{v} + \mathbf{u}\|^2$ is regularization term. We apply the ADMM algorithm to formulate an iterative algorithm to solve the augmented Lagrangian, and the pseudocode is

Initialize $\mathbf{x}, \mathbf{v}, \mathbf{u}$ and a

Repeat K times

$$\mathbf{x} \leftarrow \arg \min_{\mathbf{x}} \{ f(\mathbf{x}) + \frac{a}{2} \|\mathbf{x} - \mathbf{v} + \mathbf{u}\|^2 \} \quad [4-12]$$

$$\mathbf{v} \leftarrow \text{clip}\{\mathbf{x} + \mathbf{u}, \Omega\}$$

$$\mathbf{u} \leftarrow \mathbf{u} + (\mathbf{x} - \mathbf{v})$$

}

Here the $\text{clip}(\mathbf{x} + \mathbf{u}, \Omega)$ function clips $\mathbf{x} + \mathbf{u}$ into the convex set Ω .

After K iterations, the both \mathbf{x} and \mathbf{v} vectors converged, and \mathbf{x} equals to \mathbf{v} , as shown in Fig. 3-4-B. In addition, upon convergence, the entries in \mathbf{x} are within the imposed upper and lower bounds.

We define the proximal mapping $L(\mathbf{x}) = f(\mathbf{x}) + \frac{a}{2} \|\mathbf{x} - \mathbf{v} + \mathbf{u}\|^2$, and the implementation of Eq. 4-12 is described be achieved by the following pseudocode:

Initialize α_0

Repeat M times{

For $n \in [1, \dots, N]$ {

$$\alpha \leftarrow \alpha_0 \cdot \left(-\frac{\partial L(\mathbf{x})}{\partial x_n} \right) \quad [4-13]$$

While $L(\mathbf{x}) > L(\mathbf{x} + \alpha \cdot \boldsymbol{\varepsilon}_n)$

 {

$$\alpha \leftarrow \alpha \cdot 0.1$$

 }

$$\mathbf{x} \leftarrow \mathbf{x} + \alpha \cdot \boldsymbol{\varepsilon}_n$$

 }

}

$\boldsymbol{\varepsilon}_n$ is a column vector with its n^{th} element 1 and 0 otherwise. One full iteration of the above pseudocode consists of a sequence of single updates, where entry in \mathbf{x} is updated exactly once. After repeating M times, we can obtain the minimum for Eq. 4-12. Numerical differentiation with sufficiently small ∂x_n can be used to implement Eq. 4-13.

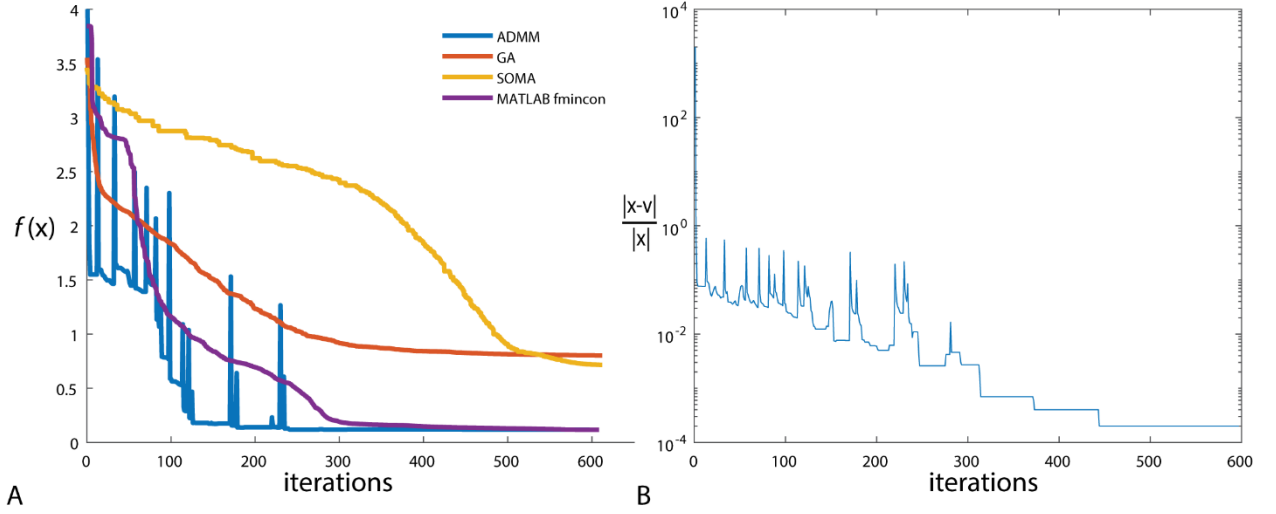


Figure 4-4. **A:** Four optimization solvers, with the objective function evaluations plotted with normalized iterations. The SAMO optimization took 11 hours to converge. **B:** The ADMM solver is able to converge when the difference between vector x and v becomes negligible

4.1.5 Reconstruction of B_1^+ profiles and RF shimming

As shown in Figure 4-2, the forward waves from the 8-channel RF amplifier are split to 16 forward waves (a_{in}) to feed the 16 coil elements. While the RF amplifier of the Siemens Magnetom 7T VB17 8 pTx system is capable of up to 165 V per channel, to target a final B_1^+ of 500 Hz, each channel is optimized with a maximum of 110 V. To include the splitter and approximate real-world conditions, we applied 4.5 dB attenuation on the forward voltage, i.e., each coil received maximum 65.5 V forward voltage. Thus, the expression of forward voltage (a_{in}) for each coil at the coil plug-in is

$$a_{in} = V_k e^{j(\phi_k)} = V_0 e^{j(\phi_{CP} + D_{inter-row})}, \quad [4-14]$$

where V_k is the forward voltage amplitude, ϕ_k is applied forward voltage phase ($k = 1, 2, \dots, 16$). To generate a circularly polarized (CP) distribution, ϕ_{CP} is $\pi/4$ phase increments along the 8 channels in the azimuthal direction. It should be recognized that there is an additional phase shift $D_{inter-row}$ (identical for all 8 channels) between the top and bottom rows of the array, reflecting additional cable lengths associated with the splitter. An optimization of Eq. 4-11 over a range of

$\Delta_{\text{inter-row}}$ ($0 - 80^\circ$) showed the least B_1^+ homogeneity at $>50^\circ$ (Figure 4-4-B). We used $\Delta_{\text{inter-row}} = 56^\circ$ for the remainder of the study.

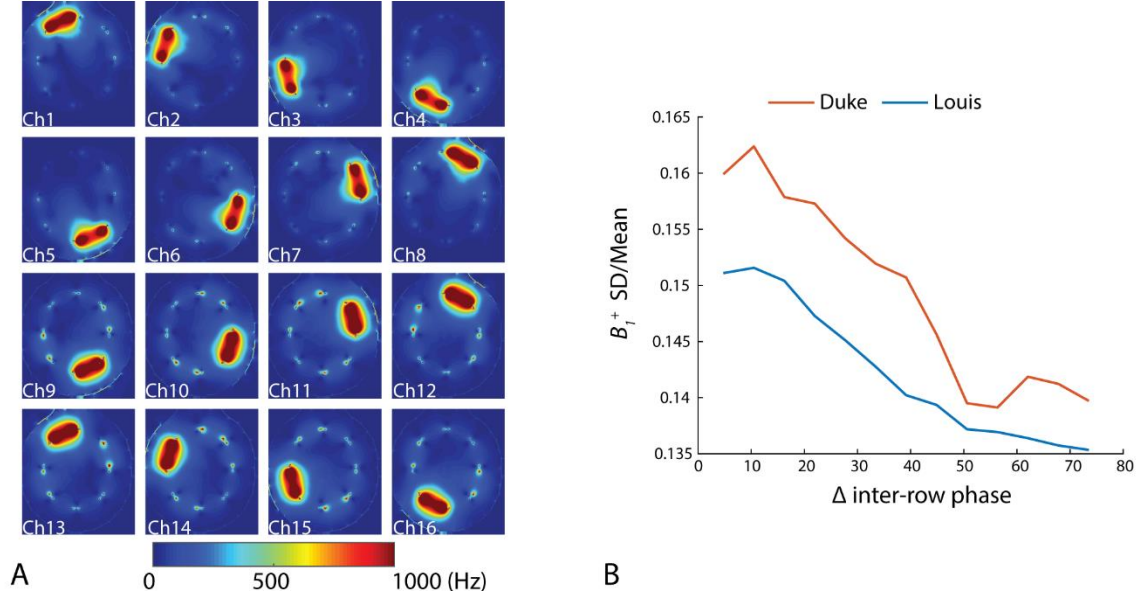


Figure 4-5. **A:** B_1^+ field magnitude for 16 channels, and each coil is fed with 65.5 V forward voltage. The field maps are taken in the axial plane at the center of each surface coil. The channel index is labeled in Figure 4-1-B. **B:** The standard deviation over mean (B_1^+ inhomogeneity) over the inter-row coil phase shift from 0 to 80° .

The \mathbf{a}_{in} is a vector concatenating \mathbf{a}_{in} of all 16 coils. Substituting this \mathbf{a}_{in} into Eq. 4-9 gives $\mathbf{a}_{\text{drive}}$, and using Eq. 4-15 gives \mathbf{a}_{lump} .

$$\mathbf{a}_{\text{lump}} = (\mathbf{S}_{\text{lump}}^{-1} - \mathbf{S}_{\text{lump lump}})^{-1} \cdot \mathbf{S}_{\text{lump drive}} \cdot \mathbf{a}_{\text{drive}} \quad [4-15]$$

After calculating $\mathbf{a}_{\text{drive}}$ and \mathbf{a}_{lump} , we can obtain the forward wave vector \mathbf{a} in Eq. 4-2, and its elements a_n are used in the following Eq. 4-16, which can be used to generate either the B_1^+ of individual coil or all coils simultaneous transmission.

$$B_1^+ = \sum_{n=1}^{208} a_n \cdot \frac{B_1^+ \text{ voltage source } n}{a \text{ voltage source } n}, \quad [4-16]$$

where the a_n is the n^{th} element of the forward wave vector \mathbf{a} , the $B_{1 \text{ voltage source } n}^+$ is the B_1^+ field map generated by the n^{th} voltage feed (one of the 208 voltage feeds in XFDTD), and $a_{\text{voltage source } n}$ is the forward voltage at the load of the n^{th} voltage feed. $a_{\text{voltage source } n}$ is calculated based on the load voltage and the reflection coefficient seen at the n^{th} voltage feed. To check the accuracy of Eq. 4-16, a simplified coil array (without the decoupling circuits) was used, i.e., a direct simulation was performed with XFDTD using lumped capacitors and voltage sources bridging the coil gaps, and matching circuits embedded at the voltage sources as SPICE circuit models. The resulting direct simulation S-parameters and field maps are compared to the calculated co-simulated results generated from Eqs. 4-10 and 4-16, respectively; Figure A-1 shows largely identical results.

For RF shimming using these simulated field maps, we used the RF shim method described in (25). For the “Homogeneous” distribution that targets the intracerebral region, two ROIs are defined: an inner ROI ($\text{ROI}^{\text{HomogPhase}}$) over which the phase per channel is calculated and a larger outer ROI ($\text{ROI}^{\text{HomogAmp}}$) that includes all of the intracerebral tissue. The $\text{ROI}^{\text{HomogPhase}}$ is used with each channel data to obtain a constant phase across all channels and the amplitudes of the forward voltages of the 8 channels (combining each vertical pair of the 16 channels) optimized to achieve the targeted B_1^+ (500 Hz, 11.7 μT) in the $\text{ROI}^{\text{HomogAmp}}$. The selections of ROI are shown in Figure A-2.

All in vivo B_1^+ data in this paper ($n=8$ total healthy controls, $n=4$ women) were acquired as part of ongoing studies recruited with Institutional Review Board approval.

4.2 Results

4.2.1 Defining the fixed transceiver T_0

Despite the variation in head sizes, the optimization yielded very consistent results as shown in Table 4-1, with an overall covariance of $\sim 8\%$. Thus the “fixed” transceiver T_0 was defined from the mean values from the four heads for each component. Using T_0 , we then optimized the tuning and matching capacitors to generate the coil S-parameter matrix at single frequency 298 MHz for each head model. As shown in Figure 4-3, the S-parameter matrices have element-wise similar magnitude and phase over the four models. For all cases, the S_{ii} and S_{ij} (for adjacent decoupled coil pairs) are close to their target values of -25 dB and -40 dB respectively, while the S_{ij} of the next adjacent coil (which is not explicitly decoupled) are all better than -14 dB.

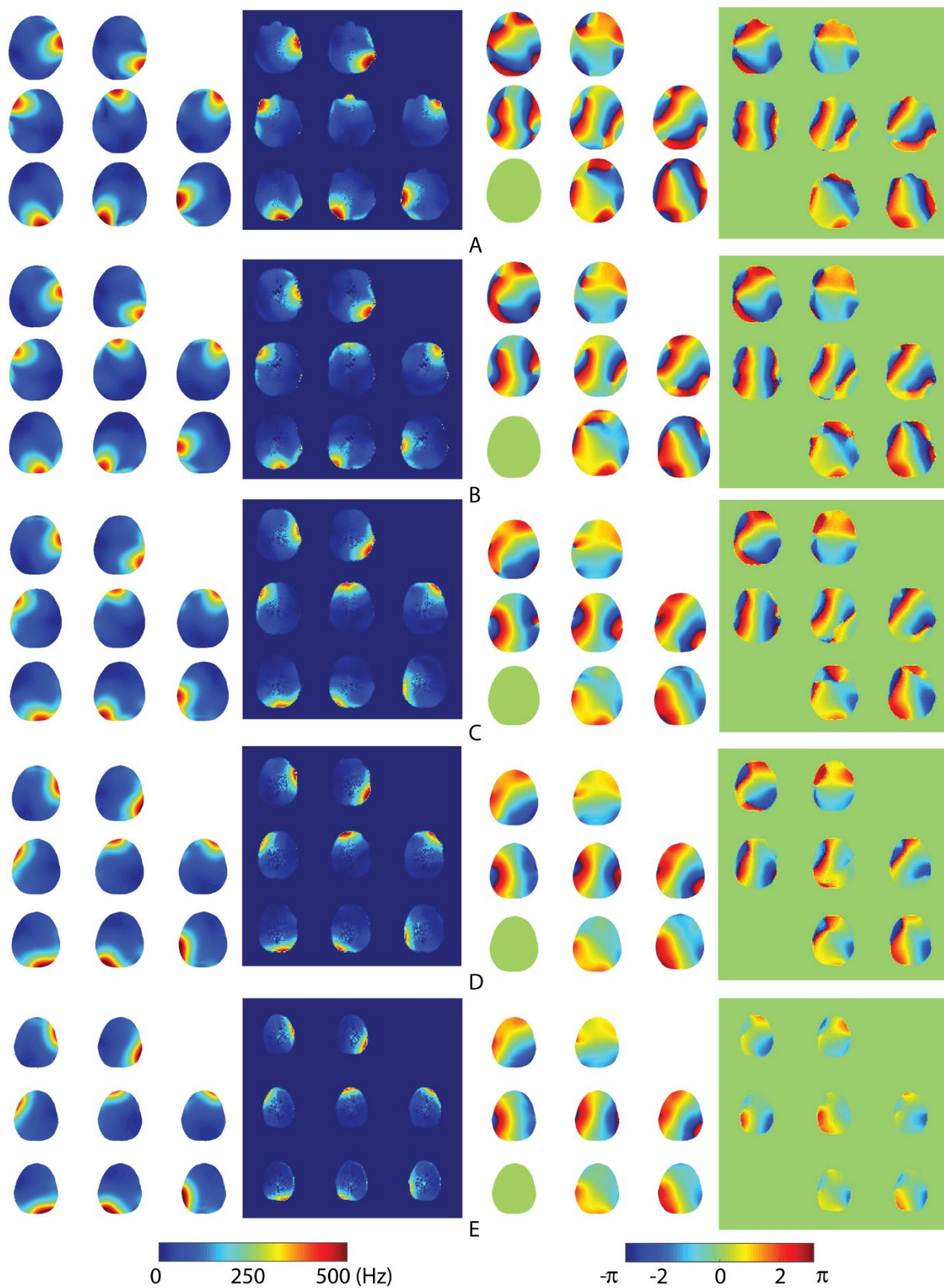
The top row 8 coils (the 9th to 16th coils) are more difficult to decouple because the top row coils are angled inward towards the human head, increasing the mutual resistance between adjacent coils. However, for all adjacent coils decoupled by the RID circuits, the S-parameter frequency sweep showed a dip, reaching S_{ij} values of -30 dB to -50 dB (95).

Figure 4-4-A shows the reconstructed B_1^+ magnitude profiles (reconstructed using Eq. 4-16) of all 16 coils loaded with the Louis model, and each coil is fed with 65.5 V forward voltage. Each coil has similar spatial distribution of B_1^+ magnitude, as each coil is well decoupled from the adjacent coils, with the coupling between the next nearest neighbor coils reaching -14 dB isolation (e.g., $S_{13,11}$ and $S_{14,12}$ in Figure 4-4-D). Allowing for variation in $\Delta_{\text{inter-row}}$, Figure 4-4-B shows that two simulating heads behaved similarly for resulting B_1^+ inhomogeneity variation, with an approximate minimum beyond $>50^\circ$.

4.2.2 Simulated and experimental B_1^+ maps

Figure 4-5 shows good agreement in the B_1^+ maps (phase, amplitude) of individual channels between simulation and experimental data for the Louis model. In both simulation and experiment, each of the 16 coils is fed with 65.5 V forward voltage.

Figure 4-6. B_1^+ phase and magnitude profiles of eight channels on five axial slices (**A-E**) evenly spaced across the simulated and in vivo heads. Within the same row, from left to right order, are the simulated magnitude, in vivo magnitude, simulated phase, and in vivo phase. The phase map of each channel is relative to the 1st channel. In both simulation and experiment, each coil is fed with 65.5 V forward voltage.



Results from the RF shimmed homogeneous B_1^+ maps using cost function Eq. 4-11 are shown in Figure 4-6 and in Table 4-2A, finding reasonable agreement with in vivo data obtained from eight human subjects.

Table 4-2. The mean and standard deviations of B_1^+ in the intracerebral tissue, and the total peak forward power of RF amplifier for homogeneous distribution. (A) Including homogeneity weighting (Eq. 4-11), (B) excluding homogeneity weighting (Eq. 4-17). (A, B) perform the transceiver T optimization individually over the four models, optimizing full set of parameter x . (C) Using the fixed transceiver T_0 as determined from the homogeneity weighted optimization.

	B_1^+ Mean (Hz)	B_1^+ Std (Hz)	B_1^+ Std/Mean %	Peak Forward Power (W)	RF efficiency (Hz/ \sqrt{W})
A: With B_1^+ inhomogeneity in cost function					
Hanako (3.14 L)	487.5	69.2	14.2	1920.84	11.12
Ella (3.20 L)	488.3	66.6	13.6	1922.79	11.14
Duke (3.75 L)	473.8	64.2	13.6	1936.00	10.77
Louis (3.28 L)	490.9	64.2	13.1	1781.28	11.63
Mean simulated	485.1 \pm 7.7	66.0 \pm 2.4	13.6 \pm 0.4	1890.2 \pm 72.9	11.16 \pm 0.35
in vivo ($n = 8$)	472.7 \pm 4.3	49.37 \pm 7.34	10.5 \pm 1.5	1723 \pm 104	11.39
B: Excluding B_1^+ inhomogeneity in cost function					
Hanako	475.1	94.0	19.8	1705.6	11.50
Ella	475.5	80.7	17.0	1782.8	11.26
Duke	472.9	81.5	17.2	1824.4	11.07
Louis	482.7	78.0	16.1	1716.4	11.65
Mean simulated	476.6 \pm 4.3	83.6 \pm 7.1	17.5 \pm 1.6	1757.3 \pm 56.3	11.36 \pm 0.26
C: Optimizing the user-tunable 32 tuning and matching capacitors on the “fixed” transceiver T_0					
Hanako	487.2	73.3	15.1	1846.11	11.34
Ella	486.2	65.3	13.4	1931.0	11.06
Duke	484.9	66.9	13.8	1915.7	11.08
Louis	490.9	64.3	13.1	1748.2	11.74
Mean simulated	487.3 \pm 2.6	67.4 \pm 4.0	13.9 \pm 0.9	1860.3 \pm 83.3	11.31 \pm 0.32

There is excellent agreement in RF efficiency, achieving an in silico $11.16 \pm 0.35 \text{ Hz}/\sqrt{W}$, in comparison in vivo $11.39 \text{ Hz}/\sqrt{W}$, and good agreement in B_1^+ inhomogeneity, at $13.6 \pm 0.4\%$ in silico, in comparison to our previous reports at 11-13% (104,105) and $10.5 \pm 1.5\%$ ($n=8$ subjects) in vivo. To mimic real world workflow, Table 4-2-C shows the performance when using the T_0 transceiver on all four head models, optimizing only the tuning and matching capacitors. As expected, the RF efficiency and B_1^+ inhomogeneity are in good agreement with in vivo data.

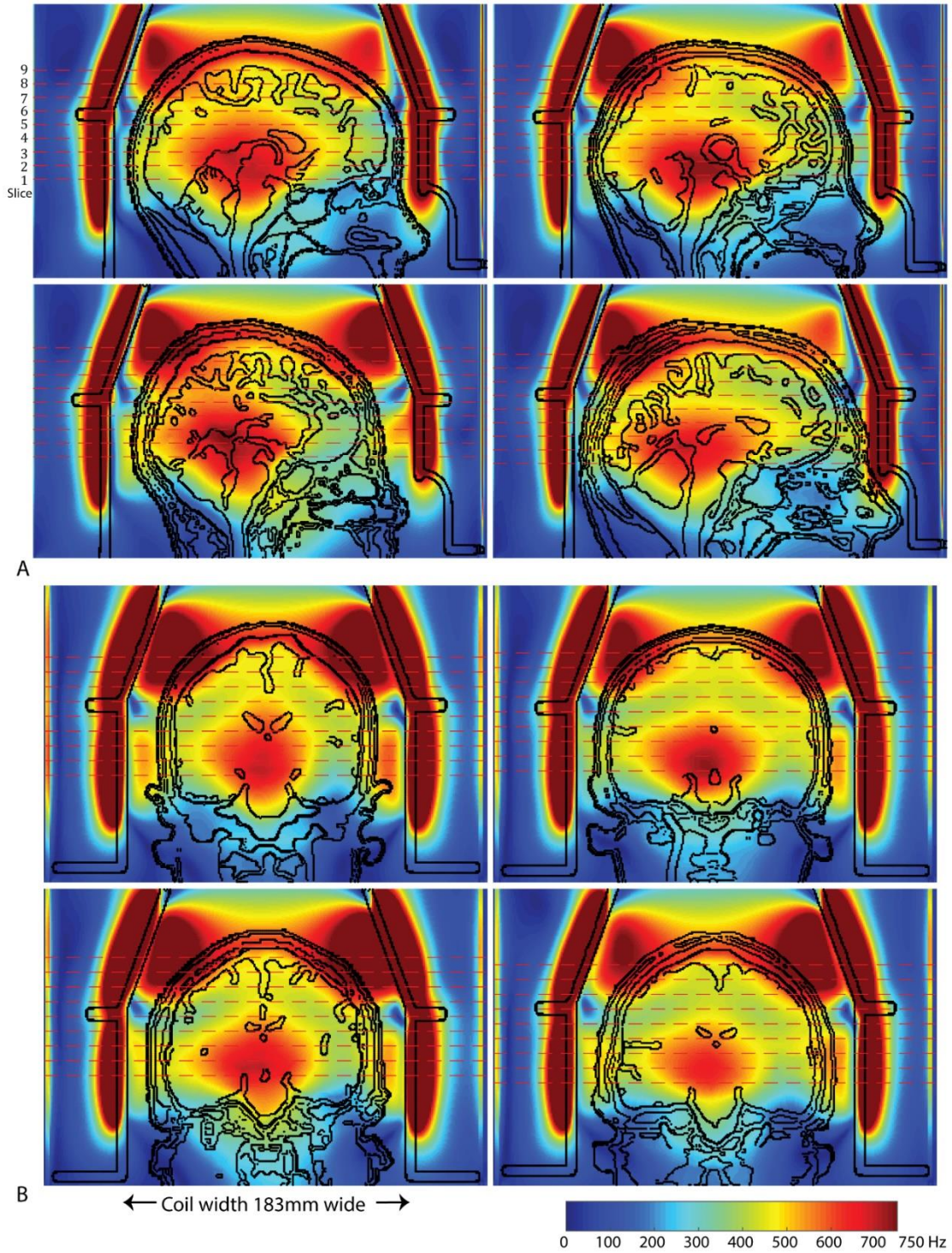


Figure 4-7. **A:** The sagittal B_1^+ profiles of the RF shimmed homogeneous distributions for Ella (top left), Louis (top right), Hanako (bottom left), and Duke (bottom right). The nine ROI slices indicated with dashed red lines are evenly spaced across the head, and the axial views are shown in Supporting Figure A-2 for four simulation heads. **B:** The corresponding coronal B_1^+ profiles for the four head models.

4.2.3 With and without a homogeneity cost function

The decoupled array design is advantageous due to better control of the coil interactions that affect homogeneity and amplitude. In this analysis, we were able to consider the homogeneity as a design feature in the cost function (Eq. 4-11) and examine the consequent impact on the coil components. For this comparison, we modified the cost function to eliminate the homogeneity condition, giving Eq. 4-17.

$$f(\mathbf{x}) = w_1 \left\| |\text{diag}(S(\mathbf{x}))| - S_{ii} \right\| + w_2 \left\| |S_r(\mathbf{x})| - S_{ij} \right\| \quad [3-17]$$

As shown in Table 4-2-A,B, comparing the effect of homogeneity weighting, the mean B_1^+ covariance worsened by $28.4 \pm 7.5\%$ to $17.5 \pm 1.6\%$, while the RF efficiency is slightly improved. Hanako exhibited the greatest change, an absolute 5% drop in covariance, $14.2\% > 19.8\%$, i.e., a $\sim 39\%$ change in inhomogeneity. The consequences of omitting the homogeneity weighting for Hanako are seen throughout the decoupling circuits, with increased isolated RID resonance frequency and TD inductor values, decreased Q factors, RID inductor values, and RID k coefficients. Figure 4-3-D,E compare the S-parameters and frequency sweeps calculated with and without homogeneity weighting for the Louis model. It is notable that with omission of the homogeneity weighting, the majority of change in the S-parameters amplitude and phase are in the top-top and top-bottom row coil interactions, with little effect in the bottom-bottom row interactions. Comparing with and without homogeneity weighting, the top-top and top-bottom S_{ij} values are remarkably worse (larger values) with homogeneity weighting. Nonetheless, with homogeneity weighting, this range of values for the $S_{ij(\text{RID top})}$, $S_{ij(\text{RID bot})}$ and $S_{ij(\text{TD})}$ is similar over the four models (Figure 4-3-A-D).

4.3 Discussion

4.3.1 Co-simulation and S-parameters optimization

This work demonstrates a co-simulation method, paired with S-parameters and B_1^+ inhomogeneity optimization to simulate a double-row, 16-coil head transmit array at 7 T. Our co-simulation model considered the matching circuits, decoupling circuits, and lumped capacitors. With the RID and TD circuits, the array coil can be tuned and matched at various loadings in silico with all coil elements achieving S_{ij} coupling better than ~ -14 dB, consistent with known in vivo performance (106). The optimization parameters accurately characterized the decoupling circuits,

e.g., the Q factors and isolated resonant frequencies of decoupling circuits are similar to those previously published (45), and would be important to account for the effect on RF power distribution by the decoupling circuits. Based on this co-simulation, the coil S-parameters and B_1^+ inhomogeneity can be optimized by different constrained optimization solvers (ADMM, SOMA, GA, and fmincon). The resulting complex field maps of individual and summed coils show excellent agreement with in vivo data.

4.3.2 Cost function: hybrid circuit-spatial domain optimization

Commercial software such as the industrial standard ADS 2020 includes S-parameter calculation but has limited cost function optimization capability and is unable to adjust the parameters used in optimization algorithms. Our analysis avoids these limitations, and we found that either the MATLAB fmincon or ADMM (data not shown) optimizations are substantially faster than ADS 2020, but more importantly, using either fmincon or ADMM, the cost function was minimized to a smaller value than with ADS 2020.

In our analysis we have compared the behavior of the S-parameters using two cost functions that explicitly use spatial information (Eqs. 4-11 and 4-17). With and without the homogeneity cost function results in significant 8-17% change in the Q factors, coupling coefficients, and inductances. It is of interest that the homogeneity weighting worsens the S_{ij} values, particularly affecting the top row coils and their coupling with the bottom row. This may reflect the need for some propagation and complex summation within the top row and between the two rows for greater resulting homogeneity, which results in a small decrease in efficiency and amplitude (~1-3%, Table 4-2-A,B). In this manner, the inclusion of the spatially variable homogeneity cost function is effectively making use of both the magnitude and phase of the S-parameters, the phase which is commonly ignored in RF simulation studies (28,31,102).

4.3.3 Simulating the transceiver and experimental B_1^+ maps

Over the four heads placed in the coil center, the simulation generated highly consistent values for the component terms (Table 4-1). The head volumes inside the RF shield are reported in Table 4-2-A left column. Several observations are of note. First, even though there is a 16.3% difference in head volume between the Duke head (3.75 liters, determined from all head tissue

within the RF shield) and Hanako head (3.14 liters), there was no significant difference between any matching circuit or decoupling components and minimal differences in S_{ij} (Figure 4-3), indicating that with the applied decoupling circuits, the residual impedance is small. Second, the effects of the decoupling circuits are clear. As demonstrated by the validation simulation of Eq. 4-16 (Figure A-1), for a single activated coil at bottom row, the highest S_{ij} (~ -9 dB) is with adjacent coil, significantly worse than the scenarios after adding the RIDs where the highest S_{ij} (~ -15 dB) is with the next adjacent coils.

Finally, there is good agreement between simulated and in vivo in terms of B_1^+ profiles (as shown in Figure 4-8) and RF power efficiency. In RF shimming, we achieved a mean B_1^+ covariance of $13.6 \pm 0.4\%$ and RF efficiency 11.16 ± 0.35 Hz/ \sqrt{W} in comparison to experimental data here of B_1^+ covariance $10.5 \pm 1.5\%$, RF efficiency 11.37 ± 0.26 Hz/ \sqrt{W} , and of 11-13% covariance previously reported (29,30), Table 4-2-A. We suspect these residuals may be a result of differences in ROI selection, head position or tilt within the array, or may still be affected by the accuracy of the model heads (e.g., in mesh size or tissue properties; for example, such measurements may depend on the temperature of the tissue, in vivo or in vitro (96); additionally, the dielectric properties of muscle can be anisotropic (97)).

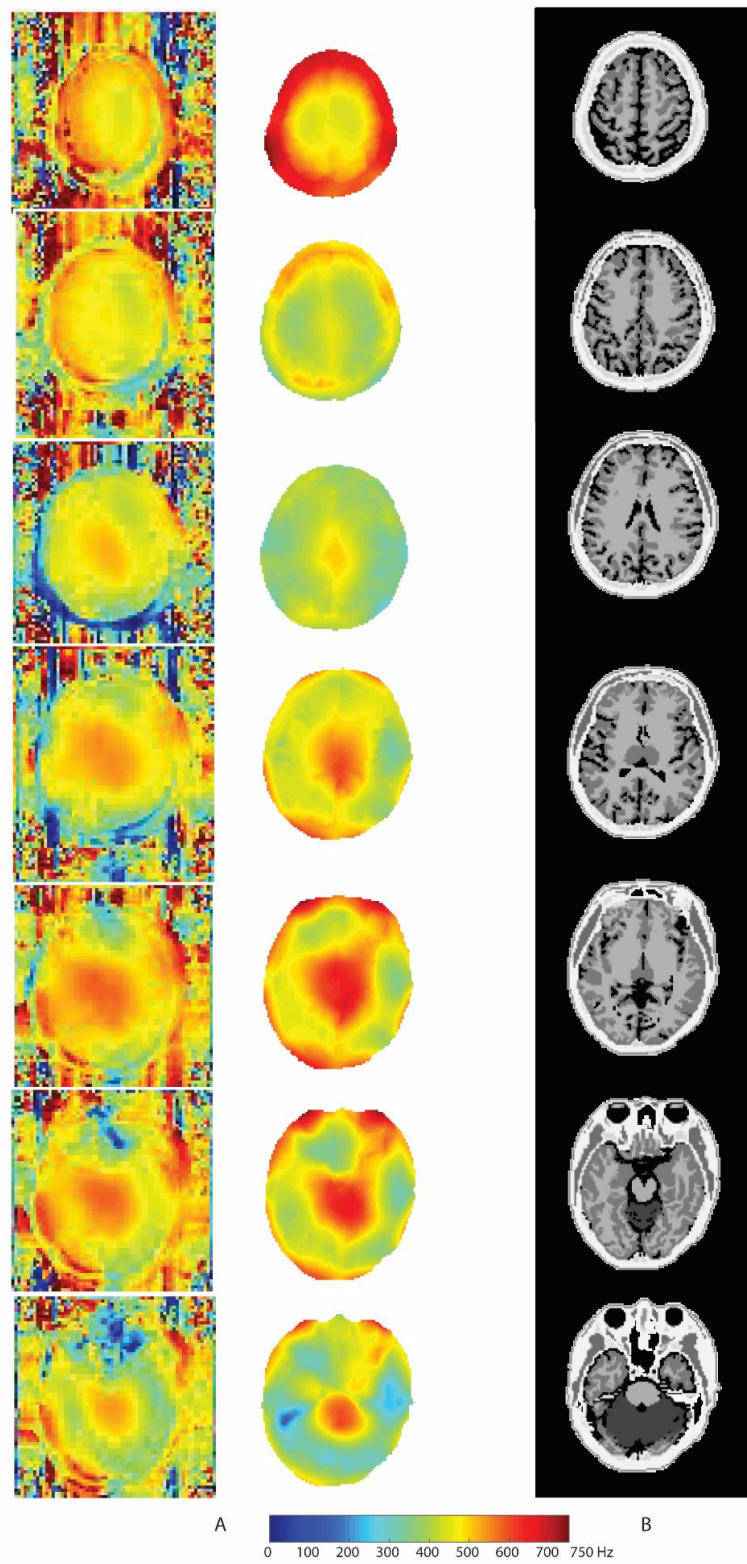


Figure 4-8. **A:** The RF shimmed B_1^+ profiles of in vivo scan compared with one simulation head. **B:** The tissue contrast image of simulated head (contrast provided solely based on tissue conductivity).

4.3.4 Additional considerations

There are several assumptions that were made in these simulations. First, we did not explicitly have measurements of the target S_{ii} for all 16 coils, instead using the 8 available experimental directional coupler measurements. The measured 8 channel S_{ii} values range from -15 dB to -20 dB, and the measurements did not account for the impedance of the 2×8 splitters, transmit/receive switches, and cables. Thus, we assumed that the actual S_{ii} of all 16 coils are -20 to -25 dB. Also, with the lumped component description of the decoupling circuits, we assumed that the decoupling circuits are small enough that they do not generate additional complex fields in the human head. Indeed, the decoupling circuits on the real coil are small in size, and they are elevated several centimeters from the surface coil. As a next step in this analysis, extension of our co-simulation method can facilitate designing the next generation of multi-row coils by finding the optimal locations to map the decoupling circuits from the circuits-domain onto the S-parameters in the co-simulation.

The hybrid circuit-spatial domain optimization may be considered disadvantageous for coil analysis, given the additional spatial complexity. Indeed, we did need to reduce the size of the available spatial data by ~20x in order to perform these analyses. However, it should be noted that the resulting additional time needed for optimization was shorter (optimization time decreased from 40 min to 30 min); we hypothesize that the additional spatial information effectively reduced the search space in the minimization.

4.4 Conclusions

Overall, this study presents a hybrid circuit-spatial domain and cost function optimization to accelerate the FDTD simulation and design stages of a double row pTx head coil. The resulting field maps are in excellent agreement with in vivo results, and the high consistency of the coil components (typically varying by 2 to 8%, mean 3.4%) over the 4 simulated heads contends that the methods are robust and identify realistic component values. The inclusion of the spatial B_1^+ homogeneity into the cost function is novel and demonstrates that the optimization of this decoupled array is based on the desired homogeneity, amplitude, and power efficiency. The available solution space shows that a substantial gain in homogeneity (28%) can be achieved with a near-negligible (2%) loss in amplitude and efficiency. The accuracy of these maps can be used

for predictions for individualized and universal RF shimming (5,27,98–100,113) and for the design of spatially accurate pulses for pTx imaging (114–116). From a coil design view, these methods are not limited by the complexity of the coil designs such as the number of lumped components, nor coil-to-coil proximity, and should thus be applicable to analysis and simulation of array coil designs of higher port counts and geometrically overlaid coils.

5. VIRTUAL OBSERVATION POINTS AND HIGH PERMITTIVITY MATERIAL

5.1 Local SAR and VOP:

The spatial matrices (S-matrices) defined in the work of Eichfelder and Gebhardt (117) is similar to the Q matrices defined by Homann (118) and Zhu (119), except the channel weights are the complex-valued waveforms in the former and the currents in the latter. The SAR of in the center of one spatial voxel (Yee's cell in FDTD) is defined as

$$\begin{aligned}
 SAR &= \frac{\sigma}{\rho} \mathbf{E}^H \cdot \mathbf{E} \\
 &= \frac{\sigma}{\rho} [(\mu_1 \exp(j\theta_1))^H \quad (\mu_2 \exp(j\theta_2))^H \quad \dots \quad (\mu_n \exp(j\theta_n))^H] \begin{bmatrix} \mu_1 \exp(j\theta_1) E_1 \\ \mu_1 \exp(j\theta_1) E_1 \\ \dots \\ \mu_n \exp(j\theta_n) E_n \end{bmatrix} \\
 &= [(\mu_1 \exp(j\theta_1))^H \quad (\mu_2 \exp(j\theta_2))^H \quad \dots \quad (\mu_n \exp(j\theta_n))^H] \underbrace{\frac{\sigma}{\rho} \begin{bmatrix} E_1 E_1^H & \dots & E_1 E_n^H \\ \dots & \dots & \dots \\ E_n E_1^H & \dots & E_n E_n^H \end{bmatrix}}_{\stackrel{\text{def}}{=} \mathbf{Q}} \begin{bmatrix} \mu_1 \exp(j\theta_1) \\ \mu_1 \exp(j\theta_1) \\ \dots \\ \mu_n \exp(j\theta_n) \end{bmatrix} \\
 &= \mathbf{U}^H \mathbf{Q} \mathbf{U} \tag{5-1}
 \end{aligned}$$

The ‘ H ’ denotes complex conjugate transpose for vectors or complex conjugate for complex numbers, and the σ and ρ is the tissue conductivity and density respectively. The E_n in Eq. 5-1 is the electric field generated by the n^{th} transmit channel at peak voltage (110 volts) with 0-degree phase shift. Here we considered 8 transmit channels in total, and \mathbf{U} is the channel weight vectors. Using Eq. 4-16 for reconstructing the reconstruct B_I^+ field and substituting the B_1^+ fields with electric fields we can also generate the electric field of each transmit channel. The $\mu_n \exp(j\theta_n)$ term in Eq. 5-1 has amplitude from 0 to 1 and phase from $-\pi$ to π . In the circuit-field optimization, we can use

$$E = \sum_{n=1}^{208} a_n \cdot \frac{E_{\text{voltage source } n}}{a_{\text{voltage source } n}},$$

To generate E fields of individual channel.

5.1.1 10-gram averaged Q matrices

Each element of the complex valued Q matrix need to be 10-gram averaged. The Q matrix element is averaged in a 10-g concentric growing cube based on the IEEE C95.3-2002 (80). Each element of the Q matrix corresponds to the combined effect of the n th and m th source. Figure 5-1 and Figure 5-2 present the $Q_{3,4}$ magnitude and phase map, corresponding to the combined E fields of source 3 and source 4. As the Q matrix is a Hermitian matrix, to save the computational power we only need to calculate half of the 10-g averaged Q matrix, as the other half will be the complex conjugate.

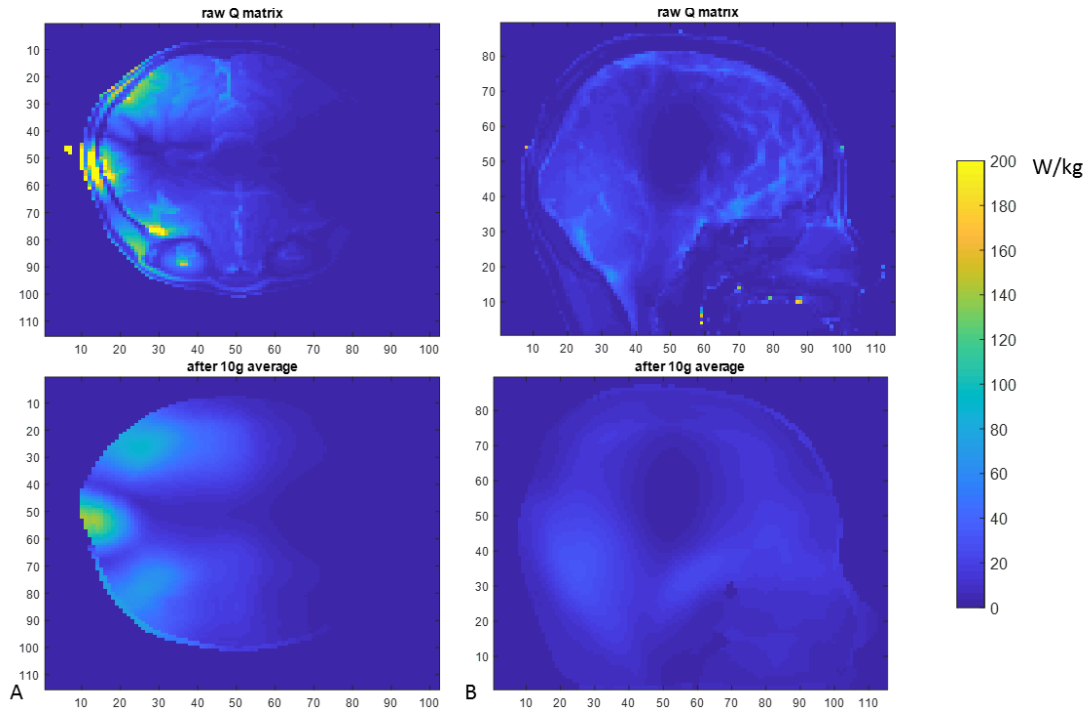


Figure 5-1. the magnitude map of the $Q_{3,4}$ element of the Q matrix. **A**: the axial view before and after the 10-gram average. **B**: the sagittal view before and after the 10-gram average.

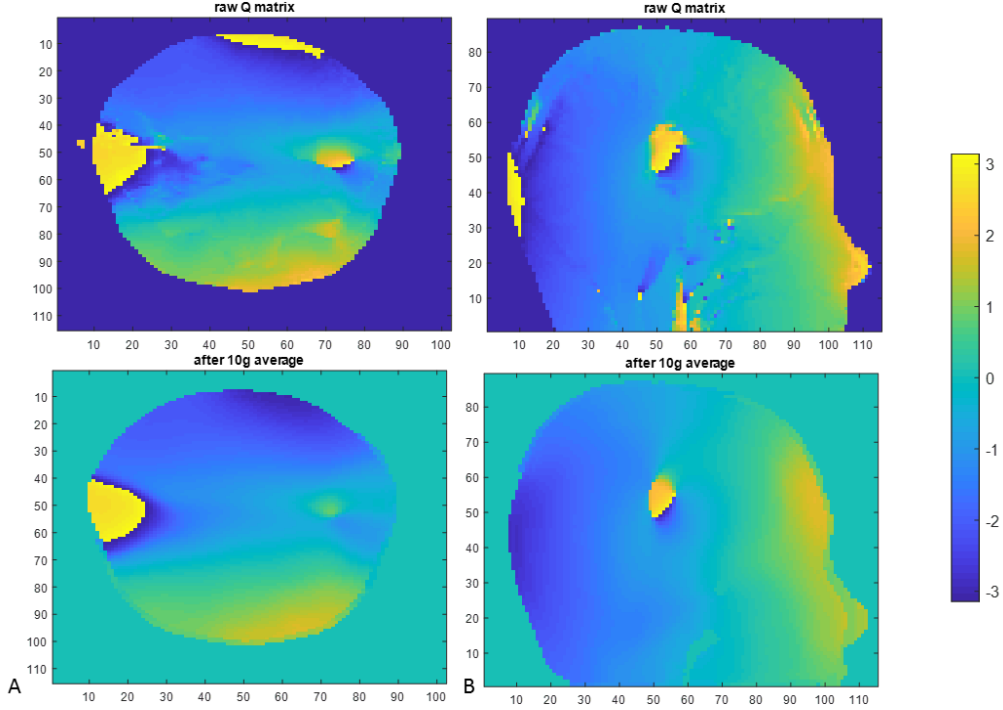


Figure 5-2. the phase map of the $Q_{3,4}$ element of the Q matrix. **A**: the axial view before and after the 10-gram average. **B**: the sagittal view before and after the 10-gram average.

5.1.2 Worst-case SAR

Eq. 5-1 is a quadratic form of $\mathbf{U}^H \mathbf{Q} \mathbf{U}$, and has an upper bound of $|\mathbf{Q}|_2 \mathbf{U}^H \mathbf{U}$, where $|\mathbf{Q}|_2$ is the 2-norm. We can express the upper bound of equation Eq. 5-1 as

$$SAR = \mathbf{U}^H \mathbf{Q} \mathbf{U} \leq |\mathbf{Q}|_2 \mathbf{U}^H \mathbf{U} \quad [5-2]$$

Since \mathbf{Q} is a Hermitian matrix, its 2-norm is the maximum eigenvalue λ_{max} of the Q matrix; We can express Eq 5-2 as:

$$|\mathbf{Q}|_2 \mathbf{U}^H \mathbf{U} = \lambda_{max} \|\mathbf{U}\|^2 \quad [5-3]$$

Eq. 5-3 is the expression of the worst-case SAR for a given voxel. We notice the worst-case SAR is independent of the phase of the n th source θ_n , but is proportional to the square of the magnitude of the channel weight vector $\|\mathbf{U}\|$. To find the global worst-case SAR, we only need to find the largest λ_{max} among all n voxels, then substitute it into Eq. 5-3.

5.1.3 VOP compression

Now we define the \mathbf{Q} matrix at the k th voxel as \mathbf{Q}_k , and call it the spatial matrix of the k th voxel. Notice \mathbf{Q}_k is a Hermitian matrix. Recall the definition of positive semi-definite (psd), for any spatial matrix \mathbf{Q}_k at the m th voxel, $m = 1, 2, \dots, N$ (there are N voxels in total). If we have

$$\mathbf{Q}_k - \mathbf{Q}_m \text{ psd}, \quad [5-4]$$

then we can have

$$\mathbf{U}^H (\mathbf{Q}_k - \mathbf{Q}_m) \mathbf{U} \geq 0, \quad [5-5]$$

for any \mathbf{U} (i.e. for any weightings applied to the pTx system). Then the minimum eigenvalue of $\mathbf{Q}_k - \mathbf{Q}_m$ is greater than zero, i.e. $\lambda_{\min}(\mathbf{Q}_k - \mathbf{Q}_m) \geq 0$.

The goal of VOP clustering is to select \mathbf{Q}_{core} from $\mathbf{Q}_1 \dots \mathbf{Q}_N$ and find \mathbf{Z} such that

$$\mathbf{Q}_{\text{core}} + \mathbf{Z} - \mathbf{Q}_1 \text{ psd}$$

$$\mathbf{Q}_{\text{core}} + \mathbf{Z} - \mathbf{Q}_2 \text{ psd}$$

...

$$\mathbf{Q}_{\text{core}} + \mathbf{Z} - \mathbf{Q}_{N-1} \text{ psd}$$

with $|\mathbf{Z}|_2$ minimal and $|\mathbf{Z}|_2 \leq \varepsilon \cdot \text{SAR}_{\text{global worst-case}}$.

The VOP matrix (\mathbf{Q}_{vop}) is defined as

$$\mathbf{Q}_{\text{vop}} = \mathbf{Q}_{\text{core}} + \mathbf{Z}, \quad [5-6]$$

so that for any spatial matrix as the m th voxel, we can have

$$\mathbf{Q}_{\text{vop}} - \mathbf{Q}_m \text{ psd}. \quad [5-7]$$

Here ε is a user-input fraction number, and it is usually taken to be 1%, 5% or 10%. The $\text{SAR}_{\text{global worst-case}}$ can be calculated by using Eq. 5-3, or one may use the maximum global SAR. To achieve better compression, we need to generate the least amount of \mathbf{Q}_{vop} matrices as possible.

5.1.4 The compression method

Here we present an effective compression method inspired by Eichfelder and Gebhardt (117)

Step 1:

Select \mathbf{Q}_{core} , which is the core matrix that has the maximum eigenvalue over all spatial matrix \mathbf{Q}_m , where $m = 1, 2, \dots, N$.

Step 2:

Arrange

$$0 \geq \lambda_{min}(\mathbf{Q}_{core} - \mathbf{Q}_1) > \lambda_{min}(\mathbf{Q}_{core} - \mathbf{Q}_2) > \dots > \lambda_{min}(\mathbf{Q}_{core} - \mathbf{Q}_N)$$

This arrangement is to ensure the overestimation $|\mathbf{Z}|_2$ grows as low as possible so that we can generate a large cluster in Step 3.

Step 3:

To achieve $\mathbf{Q}^* + \mathbf{Z}_1 - \mathbf{Q}_1$ psd with $|\mathbf{Z}_1|_2$ minimal, we assign $-\lambda_{min}(\mathbf{Q}_{core} - \mathbf{Q}_1)$ as the diagonal element of \mathbf{Z}_1 . To achieve $\mathbf{Q}^* + \mathbf{Z}_1 + \mathbf{Z}_2 - \mathbf{Q}_2$ psd with $|\mathbf{Z}_1 + \mathbf{Z}_2|_2$ minimal, we assign $-\lambda_{min}(\mathbf{Q}_{core} + \mathbf{Z}_1 - \mathbf{Q}_2)$ as the diagonal element of \mathbf{Z}_2 .

...

$$\mathbf{Q}^* + \mathbf{Z}_1 + \mathbf{Z}_2 + \dots + \mathbf{Z}_N - \mathbf{Q}_N \text{ psd}$$

Step 4:

Break from Step 3 when

$$\sum_{k=1}^N |\mathbf{z}_k|_2 > \varepsilon \cdot SAR_{\text{global worst-case}}$$

Now $\mathbf{Q}_1 \dots \mathbf{Q}_{N-1}$ are in a VOP cluster.

Step 5:

A VOP cluster has been created, now go back to Step 1 to create another VOP cluster. The only difference is now in Step 1 we do not need to consider spatial voxels that have been clustered. A complete set of VOP clusters will be created once we have either one or no spatial matrix left in Step 1.

Finished.

Here we present an example of how to compress three Q matrices below, with the constraint $\varepsilon \cdot SAR_{\text{global worst-case}} = 0.15$.

$$\mathbf{Q}_1 = \begin{bmatrix} 0.2 & 0 \\ 0 & 1.2 \end{bmatrix} \quad \mathbf{Q}_2 = \begin{bmatrix} 0.4 & 0 \\ 0 & 0.2 \end{bmatrix} \quad \mathbf{Q}_3 = \begin{bmatrix} 0.1 & 0 \\ 0 & 1.5 \end{bmatrix}$$

Step 1:

Chose core matrix

$$\mathbf{Q}_{core} = \mathbf{Q}_3 = \begin{bmatrix} 0.1 & 0 \\ 0 & 1.5 \end{bmatrix}$$

Step 2:

Arrange Q matrices in order, so \mathbf{Q}_1 goes first, then \mathbf{Q}_2 .

Step 3:

$$\text{Calculate } \mathbf{Z}_1 = \begin{bmatrix} 0.1 & 0 \\ 0 & 0 \end{bmatrix}, \mathbf{Z}_2 = \begin{bmatrix} 0.2 & 0 \\ 0 & 0 \end{bmatrix}$$

Step 4:

Break from Step 3 when $|\mathbf{Z}_2|_2 + |\mathbf{Z}_1|_2 = 0.3 > 0.15$

Step 5:

Now \mathbf{Q}_3 and \mathbf{Q}_1 are in VOP cluster #1, and \mathbf{Q}_2 is in VOP cluster #2. For VOP cluster #1, $\mathbf{Q}_{vop} =$

$$\mathbf{Q}_{core} + \mathbf{Z}_1 = \begin{bmatrix} 0.2 & 0 \\ 0 & 1.5 \end{bmatrix}; \text{ and for VOP cluster \#2, } \mathbf{Q}_{vop} = \mathbf{Q}_2.$$

Finished.

5.1.5 VOP on human heads

The channel weight vectors in Eq. 5-1 are scaled such that their Euclidean norms equal one ($\|\mathbf{U}\| = 1$). The worst-case local SAR of one voxel at $\|\mathbf{U}\| = 1$ is the maximum eigenvalue of the 10-g averaged Q matrix. Finally, the 10-g averaged Q matrices are compressed using a home-written VOP compression software previously mentioned. We generated 2000 random channel weight vectors, and their elements have varied phases and amplitudes; again, all the channel weight vectors are normalized such that $\|\mathbf{U}\| = 1$. Substitute each random channel weight vector and the uncompressed Q matrices in Eq. 5-2, we can find the maximum local SAR. Repeating these procedures, we can find the maximum local SAR for the VOP matrices.

For simulation heads in relatively shallow positions in the head coil, results are in Figure 5-3; for heads in deeper position in the head coil, results are in Figure 5-4. Figure 5-3-A shows the worst-case local SAR maps when $\|\mathbf{U}\| = 1$. The SAR distribution scale (0 – 500 W/kg) can be multiplied by $\|\mathbf{U}\|^2$ to relate to the real experience, when $\|\mathbf{U}\| \neq 1$. At 5% over-estimation rate, for Ella, 215386 10-gram averaged Q matrices were compressed to 1425 VOP matrices; for Hanako, 216837 Q matrices were compressed to 2283 VOP matrices; for Duke, 247170 Q matrices were

compressed to 1522 VOP matrices; for Louis in coil center, 222300 Q matrices were compressed to 2782 VOP matrices; for posterior shift Louis, 223592 Q matrices were compressed to 1489 VOP matrices; for superior shift Louis, 236367 Q matrices were compressed to 993 VOP matrices. As the worst-case SAR levels increased, the Q matrix compression ratio increases. Each VOP cluster has one core Q matrix. The locations of the core Q matrices of all VOP clusters are plotted on the worst-case SAR maps in Figure 5-3-A. In Figure 5-3-B, we plotted the maximum local SAR over the uncompressed Q matrices and the maximum local SAR over the compressed VOP matrices for 2000 random excitations.

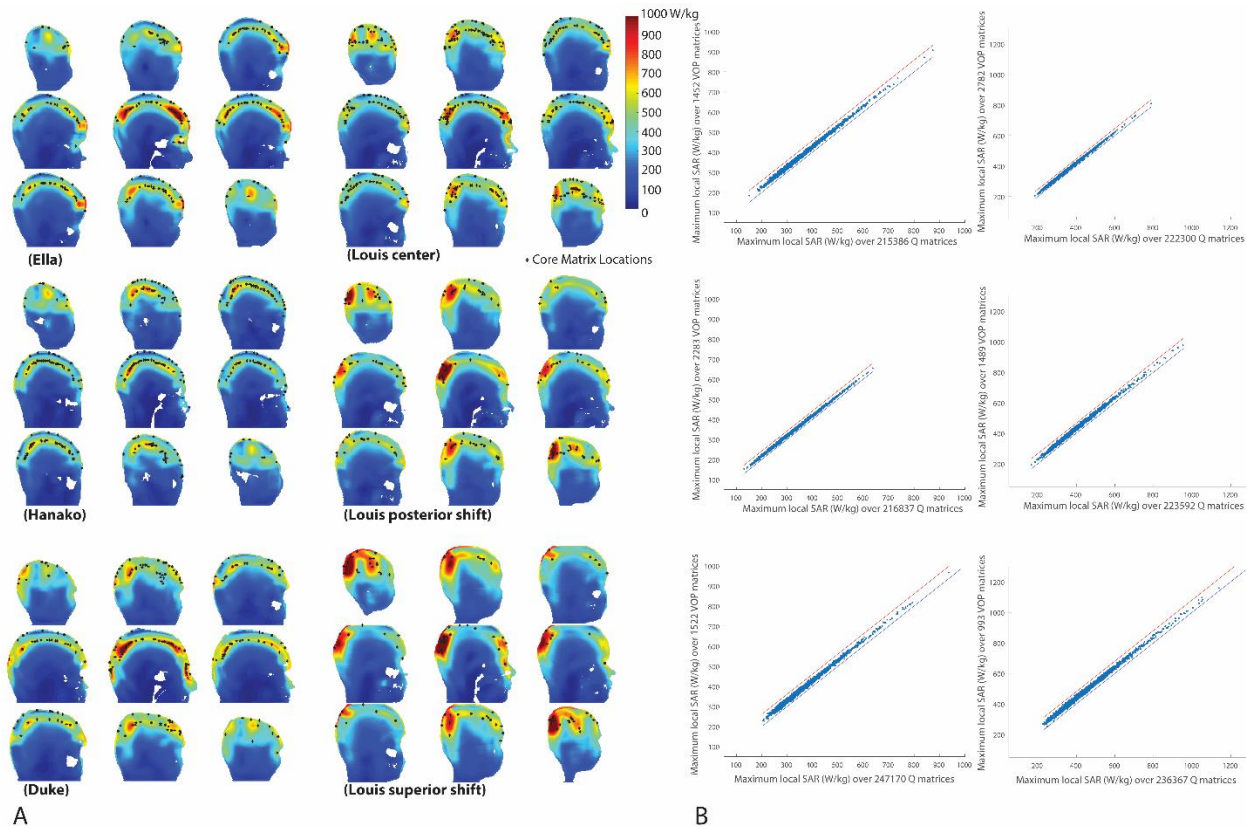


Figure 5-3. **A:** The VOP locations on the worst-case local SAR (10g-SAR) maps in sagittal views within the heads of realistic human models: of Ella, Hanako, Duke, Louis head in coil center, Louis head posterior shift, and Louis head superior shift. The SAR scale bar (0 – 1000 W/kg) are based on $\|U\| = 1$. **B:** 2000 random RF excitations were used to validate the VOP matrix with the uncompressed Q matrix at 5% over-estimation rate for heads in **A**. The maximum local SAR for both cases at all 2000 random RF excitations is plotted.

To compare ϵ effect on VOPs, we compared the Louis head (small) with Duke head (adult male, large) at $\epsilon = 5\%$ and 10% . Figure 5-4 compares the VOP core matrices location for Louis head in the center of coil, and the Duke head with nose close to the anterior part of the array coil. Table 5-1 shows the worst-case SAR, VOP matrices number, and Q matrices number for Duke and Louis. Duke has worst-case SAR nearly three times higher than Louis, and this is related with the ~ 10 to 20 times higher in VOP compression ratio for Duke. Additionally, increasing the ϵ percentage increases the VOP compression ratio, while the worst-case SAR map is not changed.

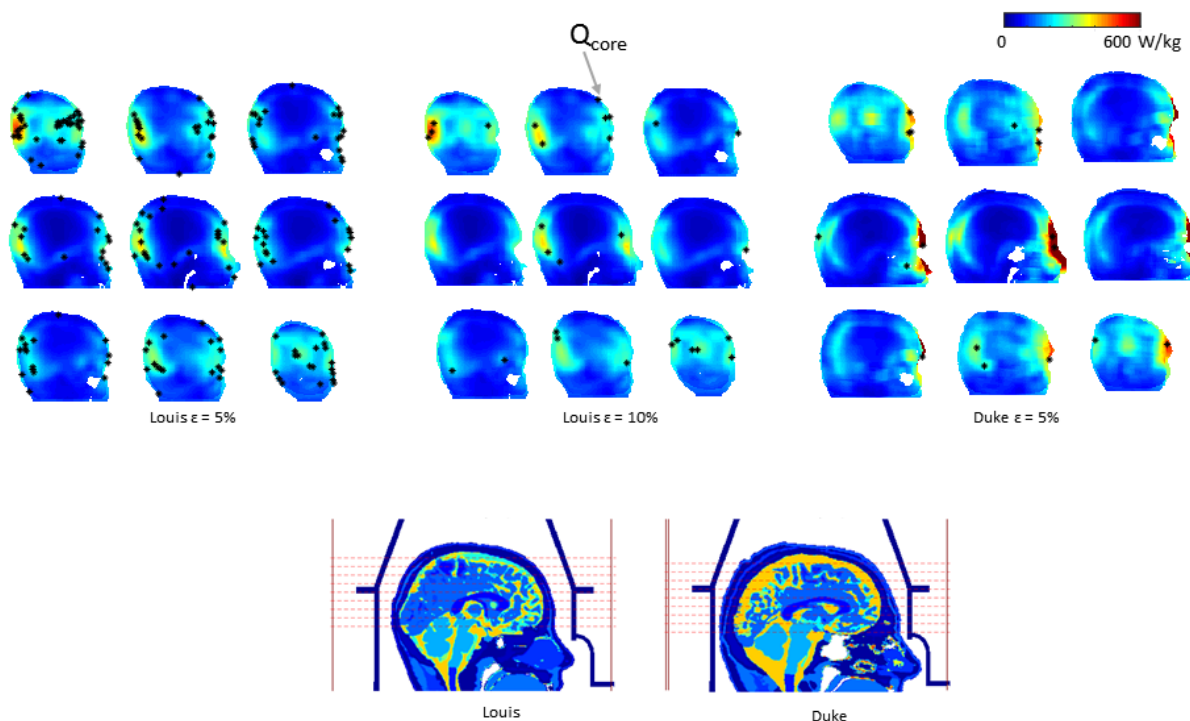


Figure 5-4. Louis VOP core matrices locations on the worst-case SAR map, for $\epsilon = 5\%$ and 10% ; and Duke VOP core matrixes for $\epsilon = 10\%$. Bottom row figures are the sagittal view of head tissue contrast maps, pTx coil former and RF shield.

Table 5-1. VOP matrices comparison for Louis and Duke

ε	Worst-case SAR (W/kg)	Number of Q matrices	Number of VOPs	Compression factor	Cubic voxel size (mm)
Louis					
$\varepsilon = 5\%$	486.5	194,376	1547	126	1
$\varepsilon = 10\%$	486.5	194,376	272	715	1
Duke					
$\varepsilon = 5\%$	1619	222,980	109	2,045	1
$\varepsilon = 10\%$	1619	222,980	27	8,259	1

5.2 HPM head former enhancing coil performance

5.2.1 HPM head former with single coil

The HPM pads have high relative permittivity ($\varepsilon_r > 100$), that has been shown to increase the RF efficiency when used in combination with birdcage RF coils (34–36). The increment of the RF efficiency for a single coil is apparent as the displacement current in the HPM pad can induce a secondary B_1^+ in the head. Figure 5-5 shows when a 5-mm thickness HPM head former covers the upper head of Louis, the RF efficiency in the head is increased as ε_r increases. The S-parameters of the pTx head coil and B_1^+ within the head in presence of the HPM have not been well studied.

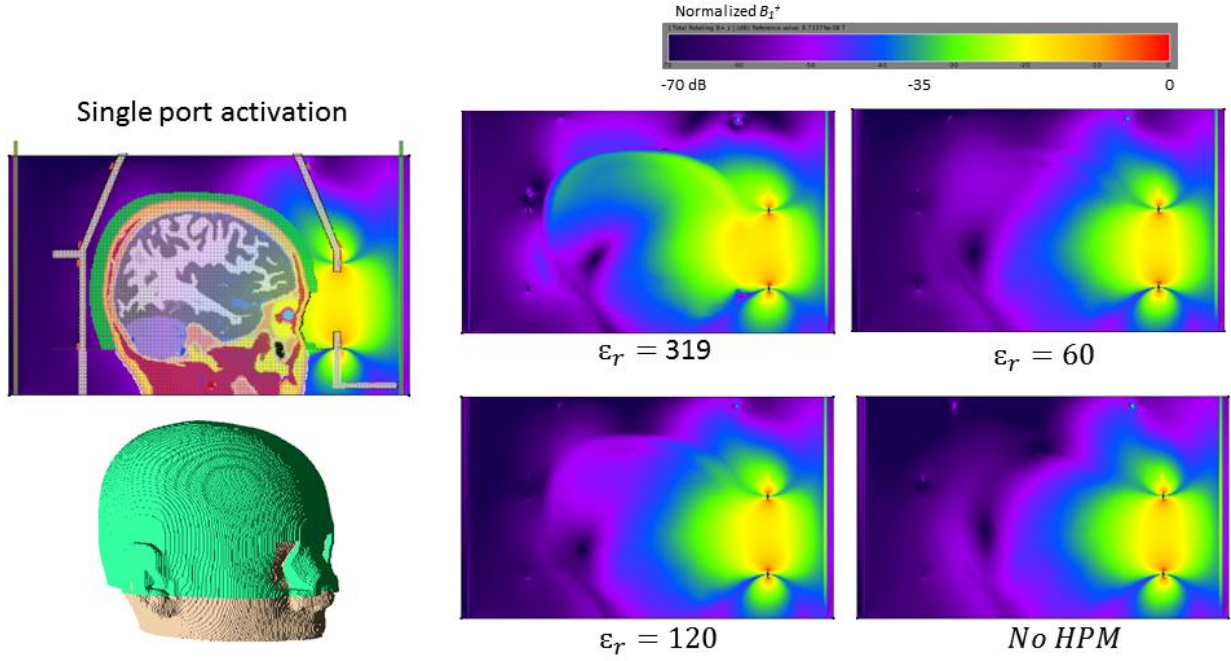


Figure 5-5. RF efficiency in the head when single port of the coil is activated when a 5-mm thickness HPM head former (green) covers the upper head. The RF efficiency increased as the relative permittivity increased.

5.2.2 HPM head former with simultaneous transmission

We applied the co-simulation method detailed in Chapter 3 with the Louis head with HPM former and compared its simulation results with those generated from direct XFDTD simulation. There is large agreement in S-parameter and B_1^+ map between the co-simulation and direct XFDTD simulation, as shown in Figure 5-6

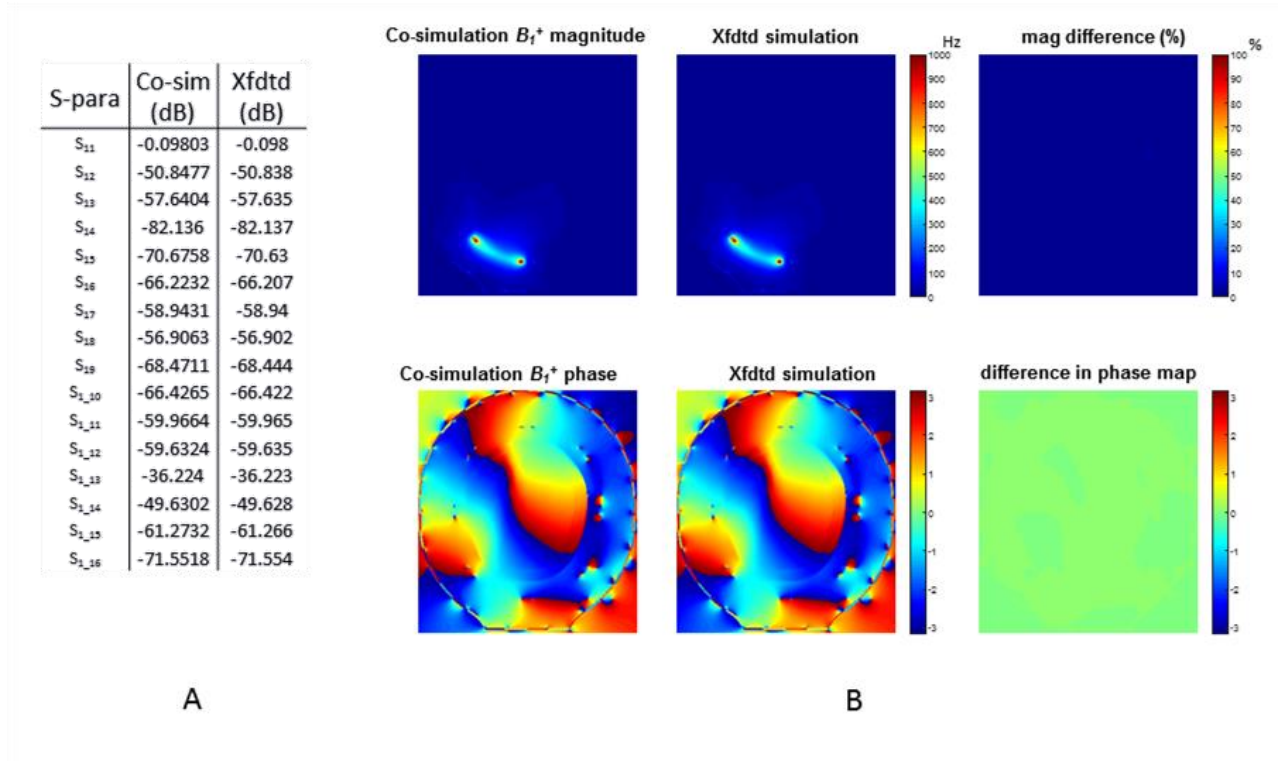
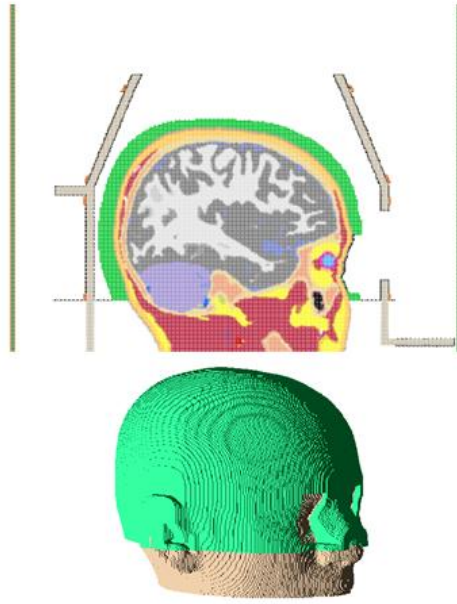


Figure 5-6. Comparisons of direct simulation and circuit-domain co-simulation. **A:** the S parameters for single coil activation, calculated separately using the circuit-domain co-simulation (left column) and direct XFDTD simulation (right column). **B:** the B_1^+ magnitude and phase map for single coil activation.

The B_1^+ statistics in the Louis upper brain tissue when wearing HPM head former are shown in Figure 5-7. There is a decrease in RF efficiency in the head with simultaneous transmission, unlike the case of an increase in RF efficiency of the single port activation in Figure 5-5. The B_1^+ homogeneity has a nonlinear relationship with the ϵ_r values; the best B_1^+ homogeneity is achieved at $\epsilon_r = 120$. We also investigated how the array coil S-parameter changes with HPM head former. The coil S-parameter with HPM head former at various ϵ_r is shown in Figure 5-8. At the resonating frequency, the S_{ij} values are not affected by the HPM below $\epsilon_r = 316$, but the S_{ii} decreases as ϵ_r decreased. At $\epsilon_r = 120$, the S_{ii} can be optimized to -16dB. At ϵ_r below 60, the coils S parameters can be optimized to values as if there is no HPM.



A

ϵ_r (relative permittivity)	B_1 mean	B_1 std	std/mean	Power	RF efficiency (Hz/ \sqrt{W})
319	458.3	74.7	0.163	1936	10.42
120	454.2	55.0	0.121	1936	10.32
90	426.4	53.3	0.125	1936	9.69
60	438.7	55.5	0.126	1936	9.97
40	438.5	57.6	0.131	1936	9.97
0	491.1	63.6	0.130	1797	11.58

B

Figure 5-7. Head former with simultaneous transmission. **A**: the sagittal view and 3D view of the HPM head former, head tissue and coil structure. **B**: The B_1^+ statistics (mean, standard deviation, power, and RF efficiency) in the brain tissue for various ϵ_r of the HPM head former.

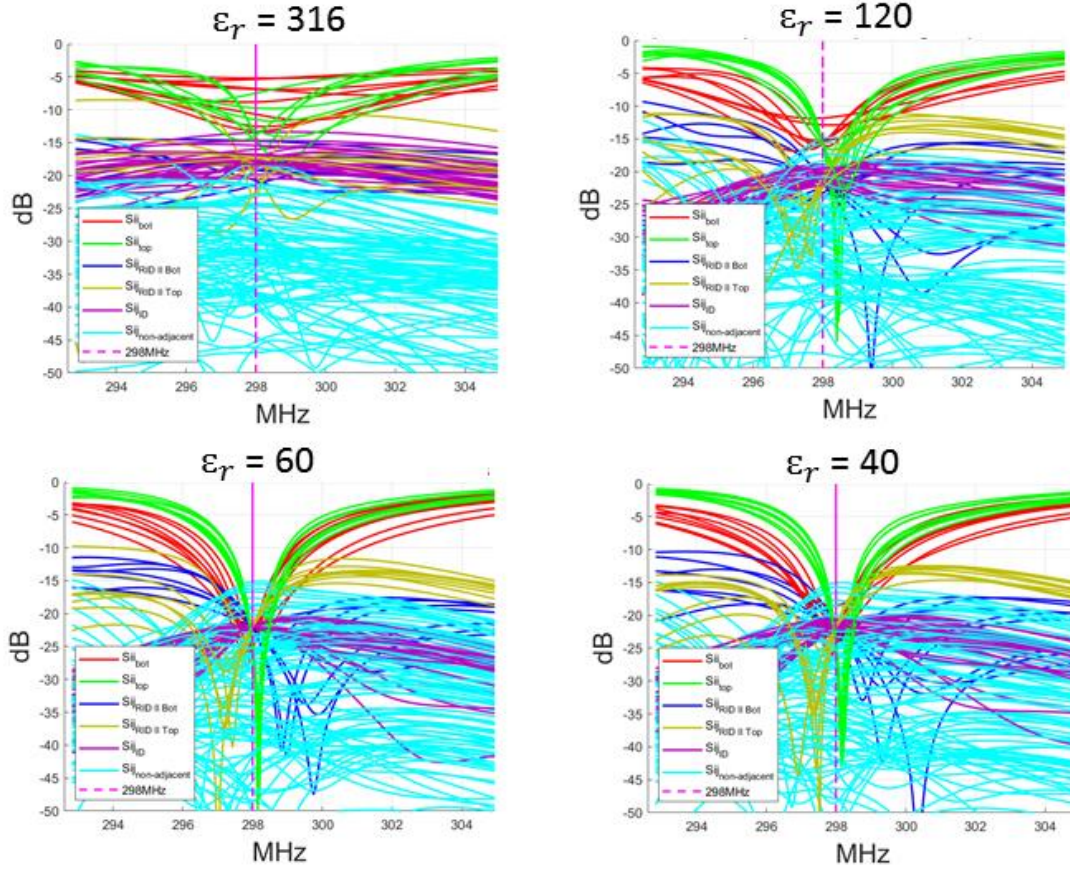


Figure 5-8. The S-parameters of the 16 channels head coil wearing HPM head former at various ϵ_r .

The sagittal view and coronal view of the Louis head with HPM $\epsilon_r = 120$ and without HPM is shown in Figure 5-9. The B_1^+ distribution is more homogeneous with HPM $\epsilon_r = 120$ as shown in Figure 5-9-A compared to without HPM as shown in Figure 5-9-B, which shows a brighter B_1^+ region in the head center.

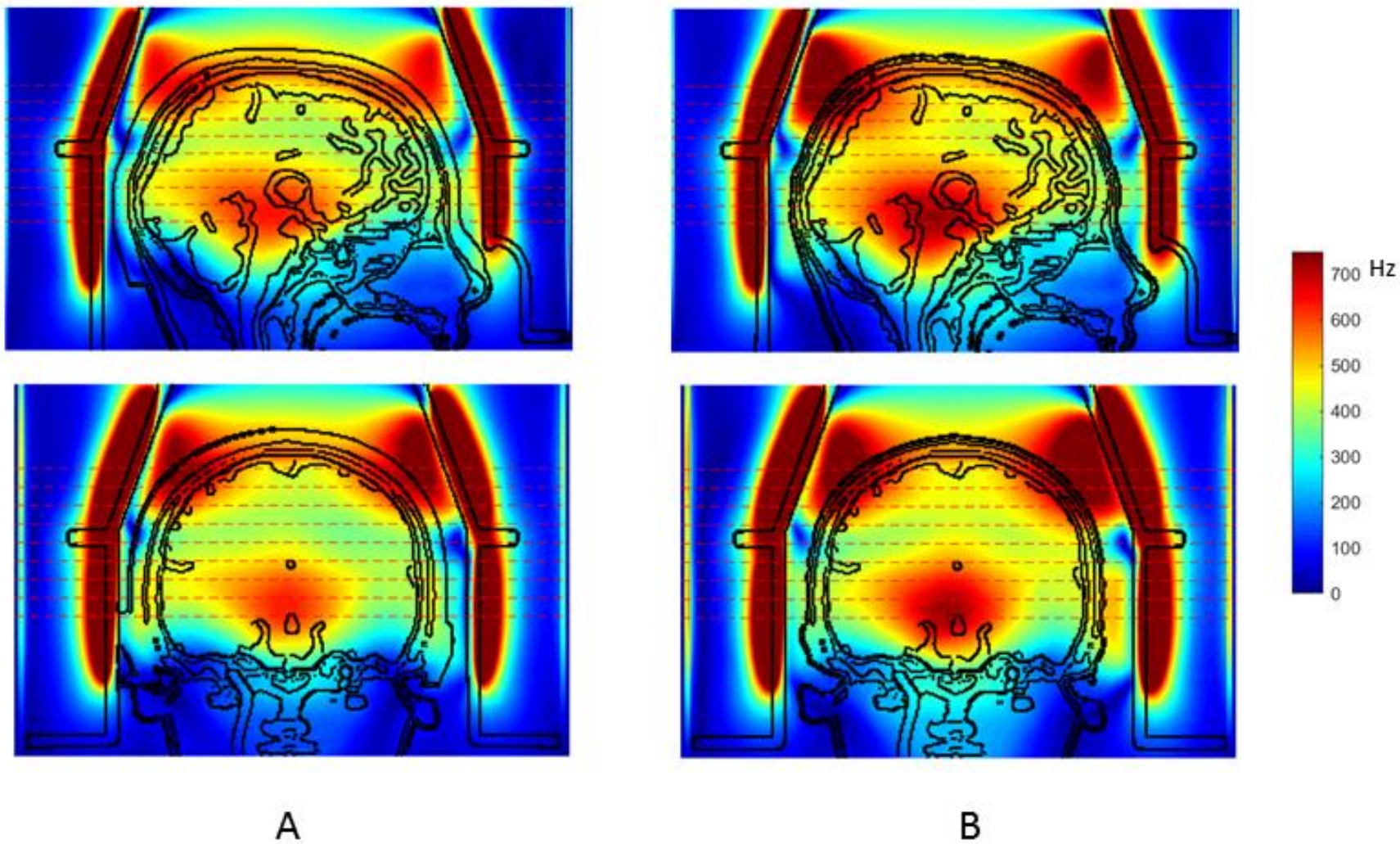


Figure 5-9. The sagittal view (top row) and coronal views (bottom row) of the Louis head when wearing HPM head former ($\epsilon_r = 120$) in **A**, and not wearing the HPM head former in **B**.

5.2.3 VOP on human heads with HPM head former

The VOP core matrices ($\epsilon = 5\%$) locations on the worst-case SAR maps for Louis without and with HPM head former is shown in Figure 5-10-A,B. The HPM head former in cyan in sagittal view is shown in Figure 5-10-D. In Figure 5-10-B, the VOP core matrices and high-level worst-case SAR are showing in the periphery of the head that covered by the HPM head former.

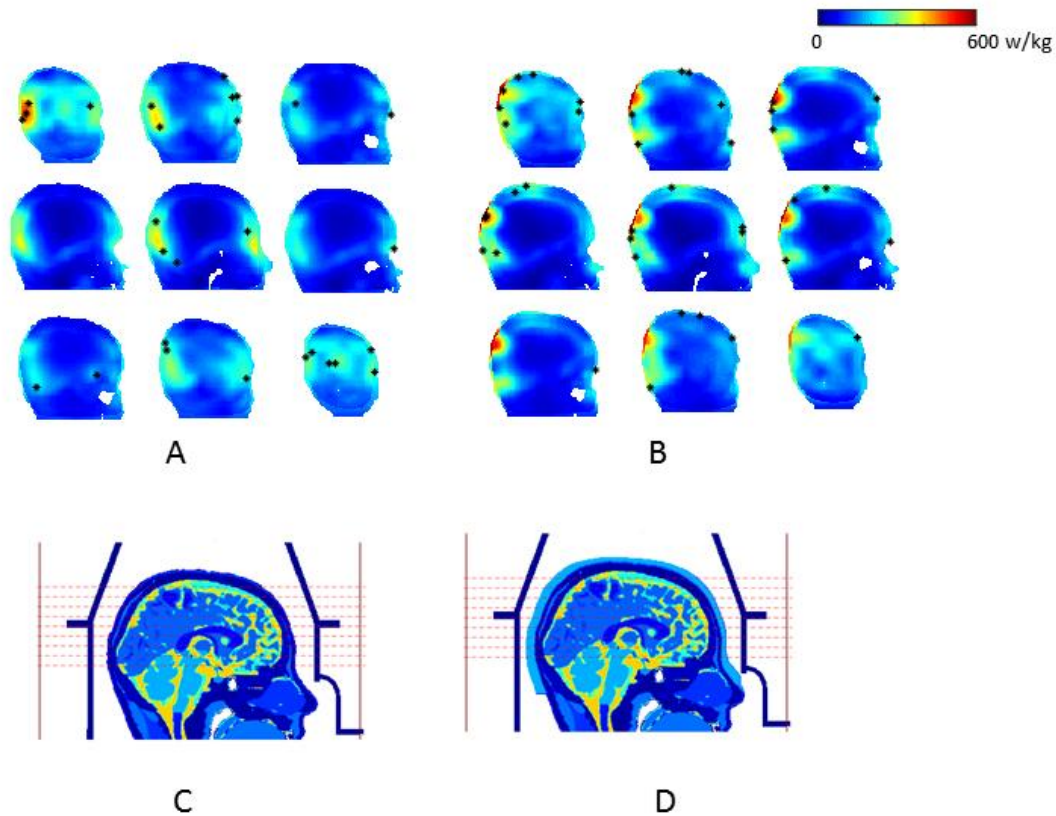


Figure 5-10. The locations of VOP cluster core matrices on the worst-case SAR map for Louis without HPM head former (A) and wearing HPM head former (B). The sagittal view of head tissue and coil structure without HPM is in C, and with HPM is in D.

The VOP matrices and worst-case SAR for Louis without and with HPM head former is shown in Table 5-2. There is 23% increment in worst-case SAR, and 7% reduction in VOP compression ratio for with HPM head former as compared to without HPM. The increment in worst-case SAR is as expected because it is at higher forward power when wearing HPM head former. As observed from the Duke model in Table 5-1, the increasing worst-case SAR will cause

increment in VOP compression ratio. But the reduction of VOP compression ratio here when wearing HPM head former is different from our previous conclusion.

Table 5-2. The VOP matrices and worst-case SAR for Louis without and with HPM.

	Worst-case SAR (W/kg)	Number of Q matrices	Number of VOPs	Compression factor	Cubic voxel size
Louis (no HPM)					
$\varepsilon = 10\%$	486.5	194,376	272	715	1mm
Louis (HPM $\varepsilon_r = 120$)					
$\varepsilon = 10\%$	598.4	202,288	306	661	1mm

APPENDIX A. S-MATRICES CALCULATION

Matching circuit \mathbf{Z} and \mathbf{S} -matrices

The \mathbf{Z} matrix for a given matching circuit is written as (using the capacitor notation in Figure 4-2):

$$\mathbf{Z}_{\text{match}} = \begin{bmatrix} S_{\text{match}+} & S_{\text{match}+-} \\ S_{\text{match}+-} & S_{\text{match}-} \end{bmatrix} = \begin{bmatrix} \frac{-j}{\omega C_s} + \frac{\frac{j}{C_s C_s}}{\frac{2\omega}{C_p} + \frac{\omega}{C_s} + \frac{\omega}{C_m}} & -\frac{\frac{j}{C_m C_s}}{\frac{2\omega}{C_p} + \frac{\omega}{C_s} + \frac{\omega}{C_m}} \\ -\frac{\frac{j}{C_m C_s}}{\frac{2\omega}{C_p} + \frac{\omega}{C_s} + \frac{\omega}{C_m}} & \frac{-j}{\omega C_m} + \frac{\frac{j}{C_m C_m}}{\frac{2\omega}{C_p} + \frac{\omega}{C_s} + \frac{\omega}{C_m}} \end{bmatrix}. \quad [\text{A1}]$$

The $\mathbf{S}_{\text{match}+}$ and $\mathbf{S}_{\text{match}+-}$ are diagonal matrices for the 16 matching circuits: the reflection coefficient between the coil and matching circuit, and the transmit coefficient between the coil and voltage feeds respectively. $\mathbf{S}_{\text{match}-}$ is the reflection coefficient between the voltage feed (RF amplifier) and matching circuit. Thus, for the 16 matching circuits,

$$\mathbf{S}_{\text{match}+} = \begin{bmatrix} S_{1 \text{ match}+} & \ddots & 0 \\ \ddots & S_{n \text{ match}+} & \ddots \\ 0 & \ddots & S_{16 \text{ match}+} \end{bmatrix} \quad [\text{A2}]$$

and

$$\mathbf{S}_{\text{match}+-} = \begin{bmatrix} S_{1 \text{ match}+-} & \ddots & 0 \\ \ddots & S_{n \text{ match}+-} & \ddots \\ 0 & \ddots & S_{16 \text{ match}+-} \end{bmatrix}. \quad [\text{A3}]$$

Lumped capacitors \mathbf{Z} and \mathbf{S} -matrices

Recall Eq. 4-6, \mathbf{S}_{lump} is of $\mathbb{C}^{192 \times 192}$, and contains the \mathbf{S} -parameters of lumped capacitors (\mathbf{S}_{cap}) and decoupling circuits (\mathbf{S}_{DC}), where \mathbf{S}_{cap} is the lumped capacitors' reflection coefficients, and it is a diagonal matrix of $\mathbb{C}^{112 \times 112}$:

$$\mathbf{S}_{\text{cap}} = \begin{bmatrix} S_{\text{cap } 1} & \ddots & 0 \\ \ddots & S_{\text{cap } n} & \ddots \\ 0 & \ddots & S_{\text{cap } 112} \end{bmatrix} = (\mathbf{Z}_{\text{cap}} - 50 \mathbf{I})(\mathbf{Z}_{\text{cap}} + 50 \mathbf{I})^{-1}, \quad [\text{A4}]$$

Where \mathbf{Z}_{cap} is a diagonal matrix, and its diagonal elements are the input impedances of the 112 lumped capacitors. To account for the capacitor equivalent series resistance (ESR), we added 0.2- Ω resistor in series with each capacitor.

Decoupling circuit \mathbf{Z} and \mathbf{S} -matrices

Recall Eq. 4-6, \mathbf{S}_{lump} is of $\mathbb{C}^{192 \times 192}$ and contains the \mathbf{S} -parameters of lumped capacitors (\mathbf{S}_{cap}) and decoupling circuits (\mathbf{S}_{DC}), where \mathbf{S}_{DC} is of $\mathbb{C}^{80 \times 80}$ and contains the 40 decoupling circuits' \mathbf{S} -parameters:

$$\mathbf{S}_{\text{DC}} = \begin{bmatrix} \mathbf{S}_{\text{DC } 1} & \ddots & \mathbf{0} \\ \ddots & \mathbf{S}_{\text{DC } n} & \ddots \\ \mathbf{0} & \ddots & \mathbf{S}_{\text{DC } 40} \end{bmatrix}, \quad [\text{A5}]$$

where $\mathbf{S}_{\text{DC } n}$ is a $\mathbb{C}^{2 \times 2}$ \mathbf{S} -parameters of the n^{th} decoupling circuit. Since each decoupling circuit has 2 ports, we have:

$$\mathbf{S}_{\text{DC } n} = \begin{bmatrix} S_{11} & S_{12} \\ S_{21} & S_{22} \end{bmatrix} = (\mathbf{Z}_{\text{DC } n} - 50 \mathbf{I})(\mathbf{Z}_{\text{DC } n} + 50 \mathbf{I})^{-1}, \quad [\text{A6}]$$

where the $\mathbf{Z}_{\text{DC } n}$ is a $\mathbb{C}^{2 \times 2}$ impedance matrix of the n^{th} RID or TD circuit, and their expressions are calculated as below. As shown in Figure 4-1-B, the RID decoupling circuits are used to decouple within-row adjacent coil pairs, while the TD circuits are used to decouple “cornering” coils and between-row coil pairs. Using notations in Figure 4-1-D, the RID circuit \mathbf{Z} matrix is written as:

$$\mathbf{Z}_{\text{RID}} = \begin{bmatrix} j\omega L_0 + R_0 - \frac{\omega^2 k_0^2 L_0^2 (j\omega L_0 - \frac{j}{\omega C_0} + R_0)}{(j\omega L_0 - \frac{j}{\omega C_0} + R_0)^2 - (\frac{j}{\omega C_0})^2} & \frac{-\omega^2 k_0^2 L_0^2 (\frac{j}{\omega C_0})}{(j\omega L_0 - \frac{j}{\omega C_0} + R_0)^2 - (\frac{j}{\omega C_0})^2} \\ \frac{-\omega^2 k_0^2 L_0^2 (\frac{j}{\omega C_0})}{(j\omega L_0 - \frac{j}{\omega C_0} + R_0)^2 - (\frac{j}{\omega C_0})^2} & j\omega L_0 + R_0 - \frac{\omega^2 k_0^2 L_0^2 (j\omega L_0 - \frac{j}{\omega C_0} + R_0)}{(j\omega L_0 - \frac{j}{\omega C_0} + R_0)^2 - (\frac{j}{\omega C_0})^2} \end{bmatrix}, \quad [\text{A7}]$$

where

$$C_0 = \frac{2}{\omega_0^2 L_0}, \text{ and } R_0 = \omega_0 L_0 / Q_0.$$

The TD circuit \mathbf{Z} matrix is written as:

$$\mathbf{Z}_{\text{TD}} = \begin{bmatrix} j\omega L_1 + R_1 & j\omega k_1 L_1 \\ j\omega k_1 L_1 & j\omega L_1 + R_1 \end{bmatrix}, \quad [\text{A8}]$$

where

$$R_1 = \omega L_1 / Q_1.$$

After the impedance matrices of decoupling circuits are derived, we can derive the S-matrices using Eq. A6.

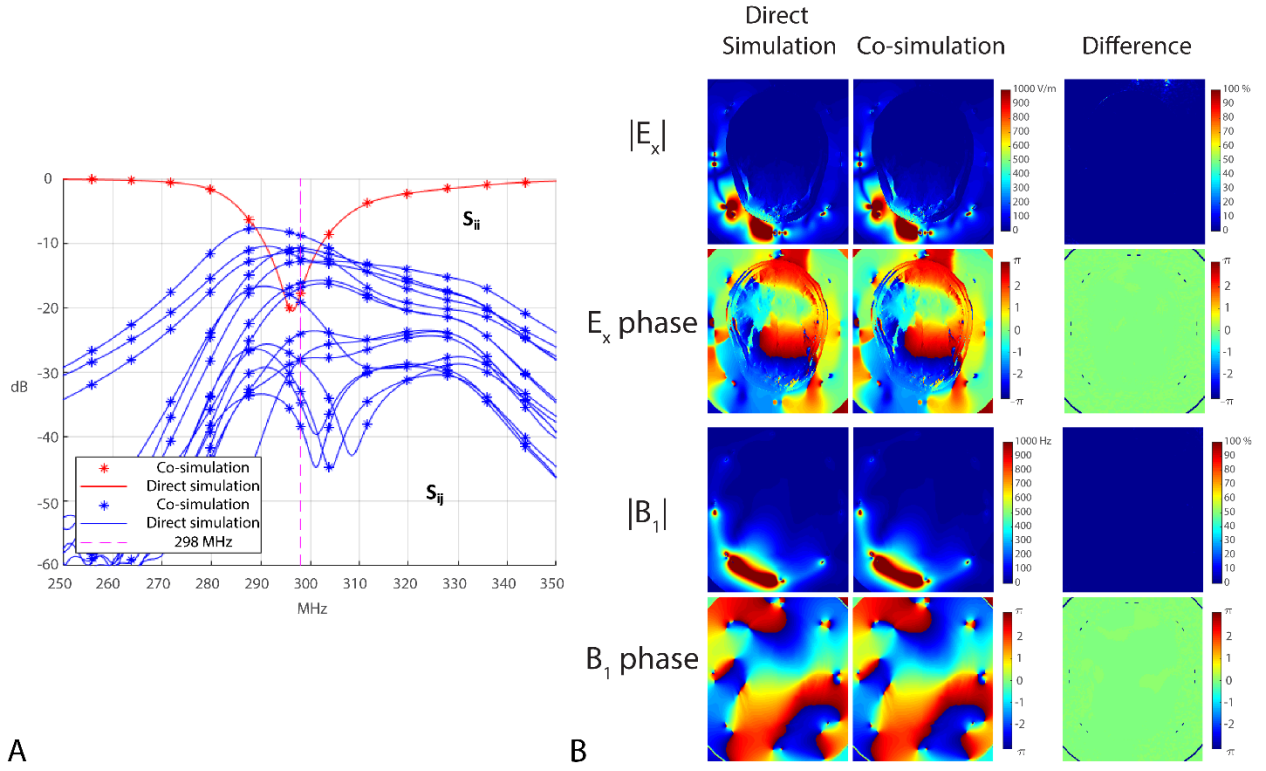


Figure A-1. Comparison of co-simulation with direct XFDTD simulation. The voltage feed for the direct simulation is 150 V, 50 Ω at 90° phase shift; and the a_{in} for the co-simulation is 75 V; this value is $V_+ = V_L / (1 + S_{11})$, where V_L is the load voltage and S_{11} is the reflection coefficient seen at the voltage feed in the direct simulation. **A** displays the S-parameters of one channel (S_{ii} red, S_{ij} blue), and **B** shows the corresponding E_x and B_1 phase and magnitude maps.

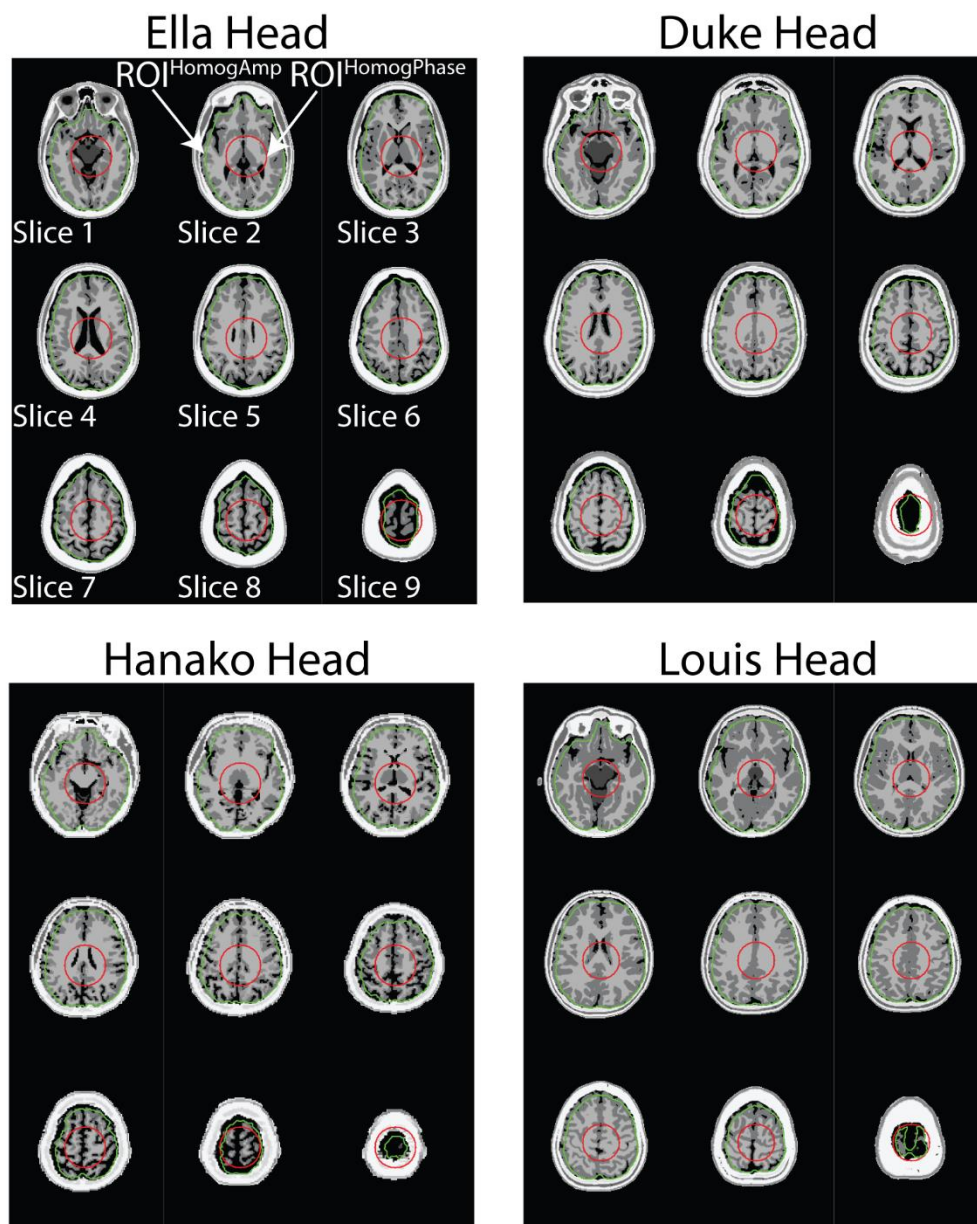


Figure A-2. The ROI selections for the Homogeneous distribution. The ROIs are overlaid on the head in the axial view.

APPENDIX B. BREAST MODEL

Figure B-1. Sagittal plots of raw SAR in 7 T at mean $B_1^+ = 1.5 \mu\text{T}$ within breast tissue for 0.5-mm resolution breast models derived from the BI-RADS categorized CT (triangles) and MRI (squares) images fused with Ella (stars) and Hanako (diamonds). The same breast models from Ella (upper row) are down-sampled to fuse with Hanako (lower row). The FGT%, in ascending order, is quantified below the marker lines. The FGT% values on the left and right side of the forward slash correspond to Ella and Hanako breasts, respectively. Raw SAR of 0 dB = 1.3 W/kg. All images are taken from the axial plane across the coil center in the same field of view. The blank raw SAR in the Hanako model corresponds to internal air in the large intestine.

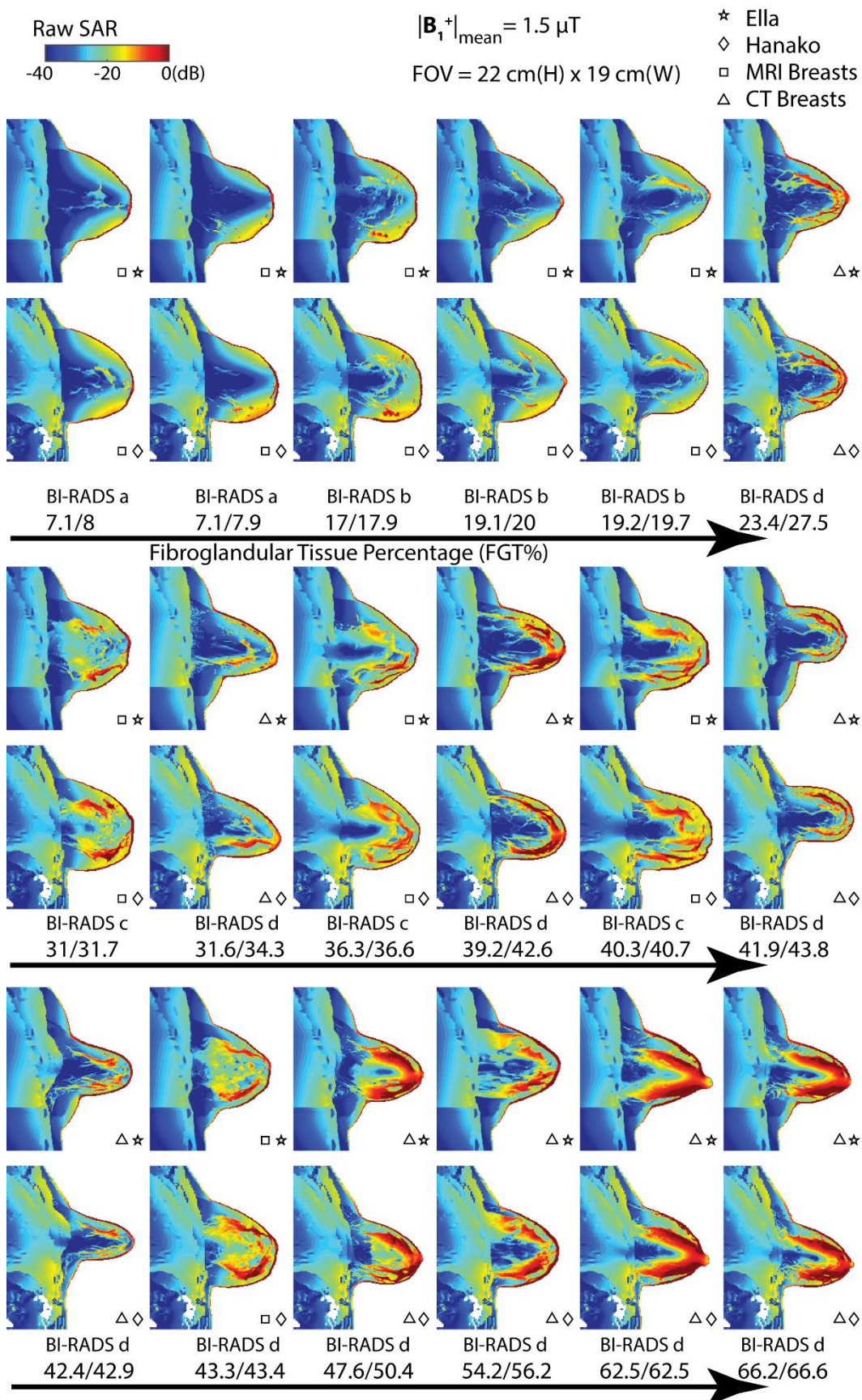


Figure B-2. Sagittal plots of 10-g averaged SAR in 7 T at mean $B_1^+ = 1.5 \mu\text{T}$ within breast tissue for 0.5-mm resolution breast models derived from the BI-RADS categorized CT (triangles) and MRI (squares) images fused with Ella (stars) and Hanako (diamonds). The same breast models from Ella (upper row) are down-sampled to fuse with Hanako (lower row). The FGT%, in ascending order, is quantified below the marker lines. The FGT% values on the left and right side of the forward slash correspond to Ella and Hanako breasts, respectively. 10-g SAR of 0 dB = 1.3 W/kg. All images are taken from the axial plane across the coil center in the same field of view.

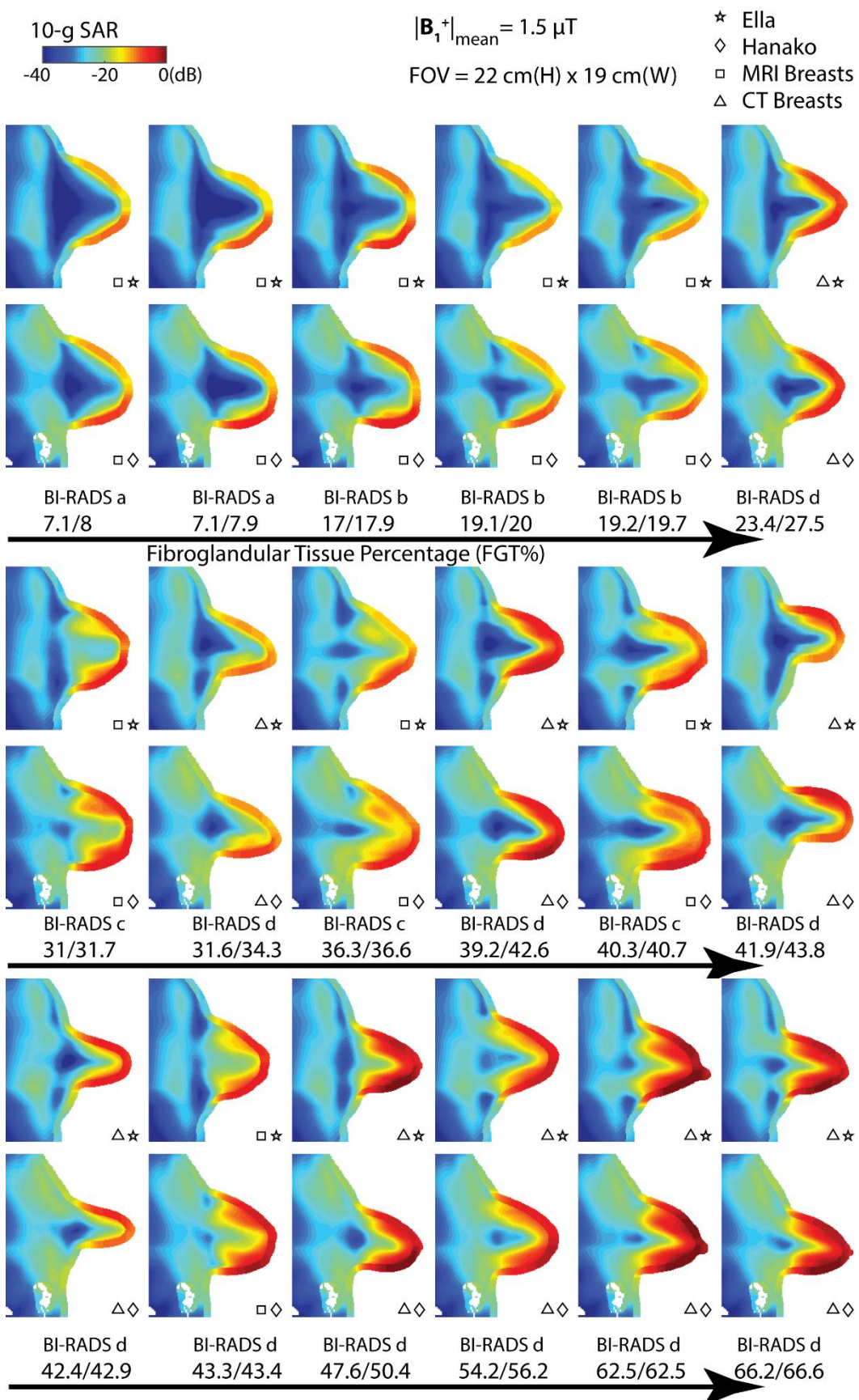


Figure B-3. Sagittal plots of temperature rise when tissue temperature reaches the steady-state in 7 T at mean $B_1^+ = 1.5 \mu\text{T}$ within tissue for 0.5-mm resolution breast models derived from the BI-RADS-categorized CT (triangles) and MRI (squares) images fused with Ella (stars) and Hanako (diamonds). The same breast models from Ella (upper row) are down-sampled to fuse with Hanako (lower row). The FGT%, in ascending order, is quantified below the marker lines. The FGT% values on the left and right of the forward slash correspond to Ella and Hanako breasts, respectively. All images are taken from the sagittal plane across the coil center in the same field of view.

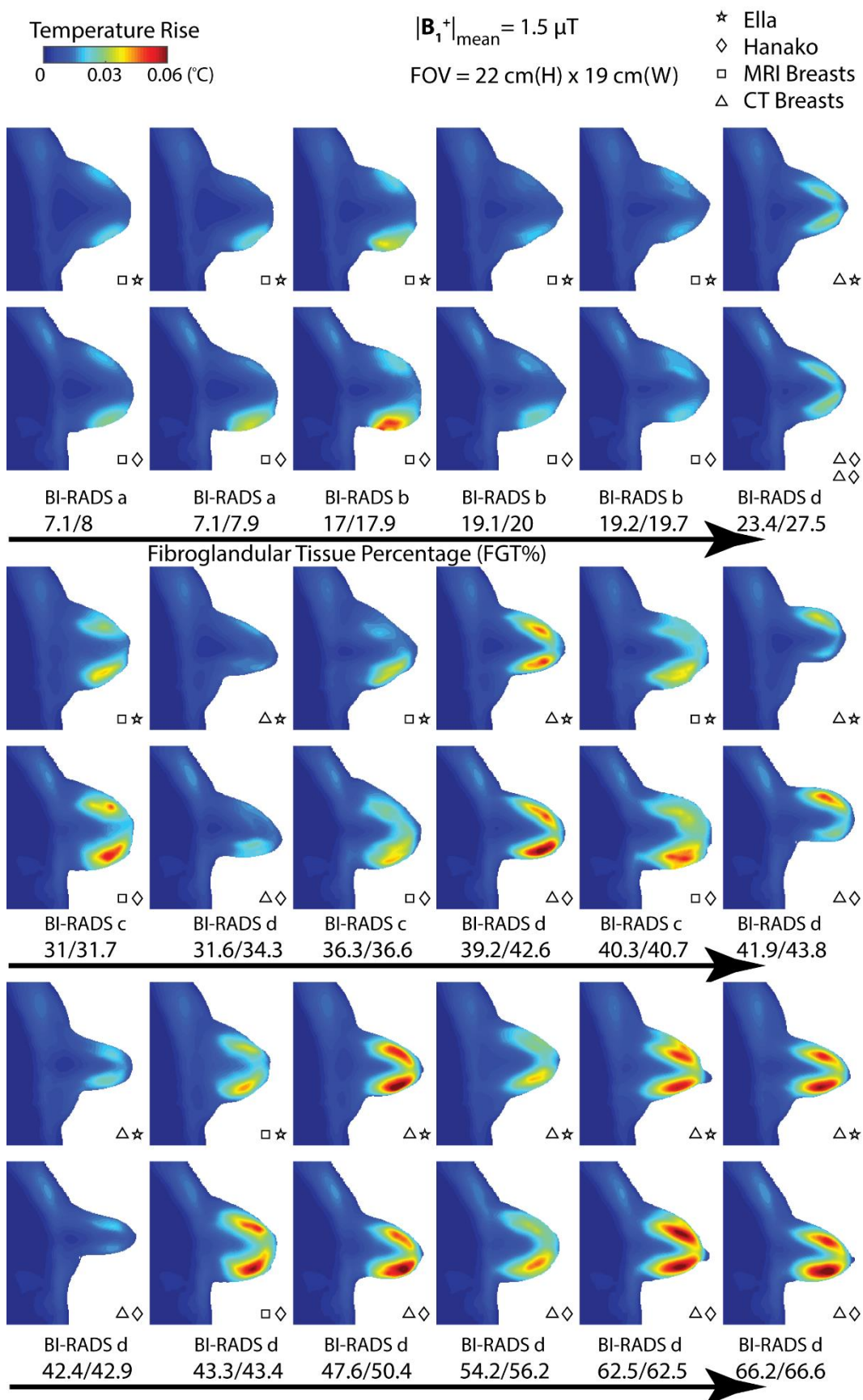


Figure B-4. Axial plots of raw SAR in 7 T at mean $B_1^+ = 1.5 \mu\text{T}$ within breast tissue for 0.5-mm resolution breast models derived from the BI-RADS categorized CT (triangles) and MRI (squares) images fused with Ella (stars) and Hanako (diamonds). The same breast models from Ella (upper row) are down-sampled to fuse with Hanako (lower row). The FGT%, in ascending order, is quantified below the marker lines. The FGT% values on the left and right side of the forward slash correspond to Ella and Hanako breasts, respectively. Raw SAR of 0 dB = 1.3 W/kg. All images are taken from the axial plane across the coil center in the same field of view.

Raw SAR
-40 -20 0(dB)

$|B_1^+|_{\text{mean}} = 1.5 \mu\text{T}$
FOV = 19 cm(H) x 17 cm(W)

★ Ella
◇ Hanako
□ MRI Breasts
△ CT Breasts

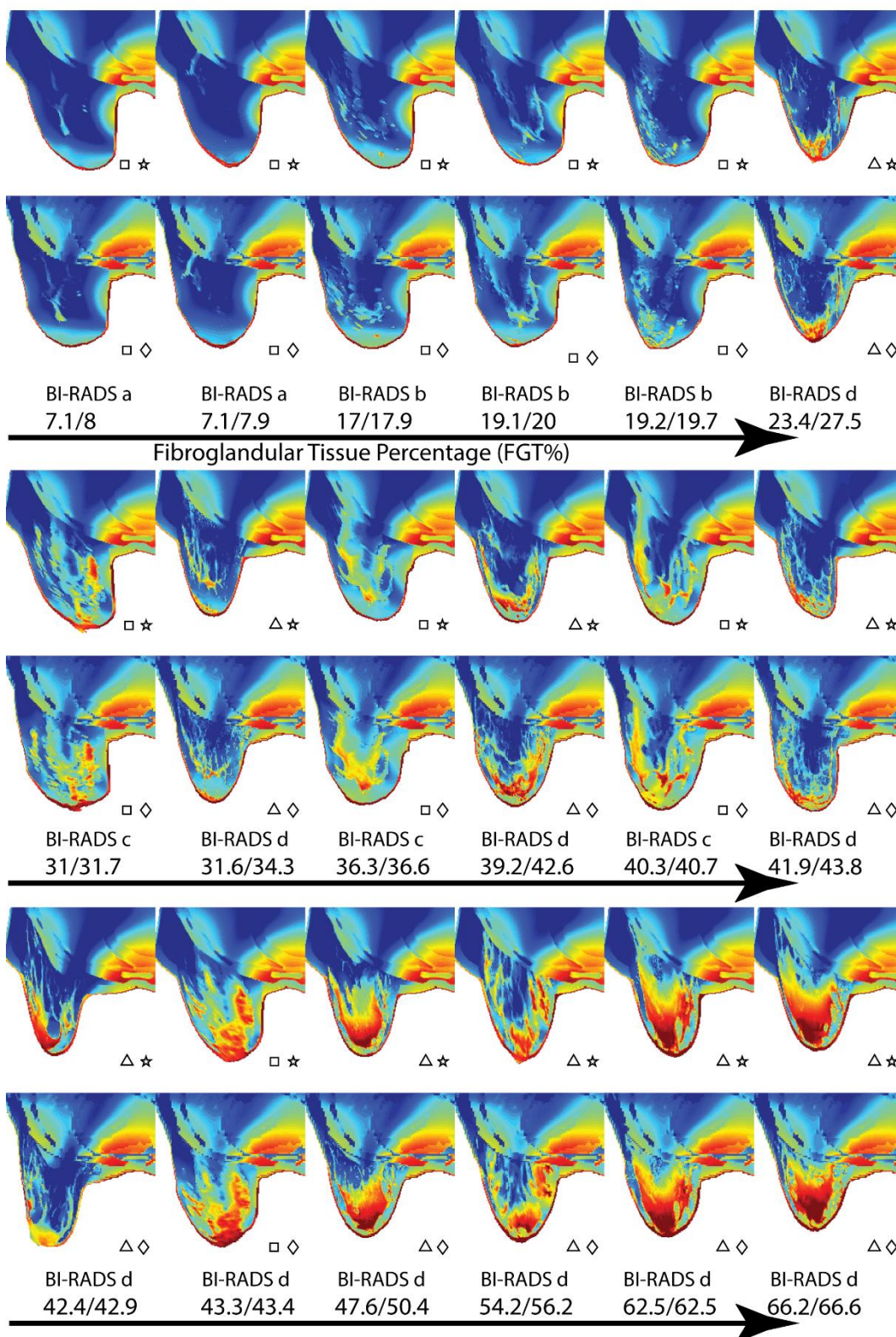
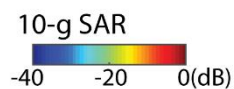


Figure B-5. Axial plots of 10-g averaged SAR in 7 T at mean $B_1^+ = 1.5 \mu\text{T}$ within breast tissue for 0.5-mm resolution breast models derived from the BI-RADS categorized CT (triangles) and MRI (squares) images fused with Ella (stars) and Hanako (diamonds). The same breast models from Ella (upper row) are down-sampled to fuse with Hanako (lower row). The FGT%, in ascending order, is quantified below the marker lines. The FGT% values on the left and right side of the forward slash correspond to Ella and Hanako breasts, respectively. 10-g SAR of 0 dB = 1.3 W/kg. All images are taken from the axial plane across the coil center in the same field of view.



$|B_1^+|_{\text{mean}} = 1.5 \mu\text{T}$
FOV = 19 cm(H) x 17 cm(W)

- ★ Ella
- ◇ Hanako
- MRI Breasts
- △ CT Breasts

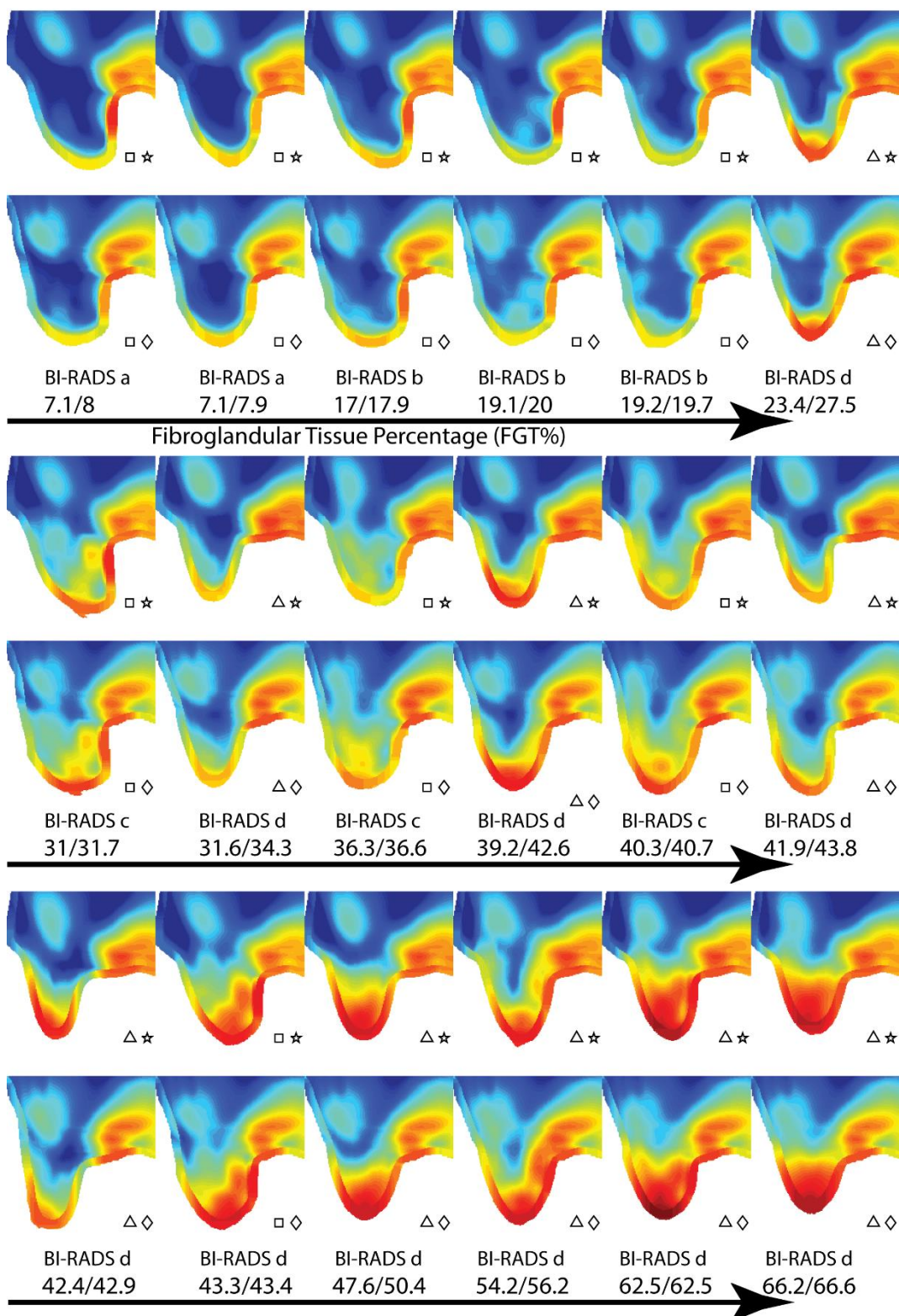
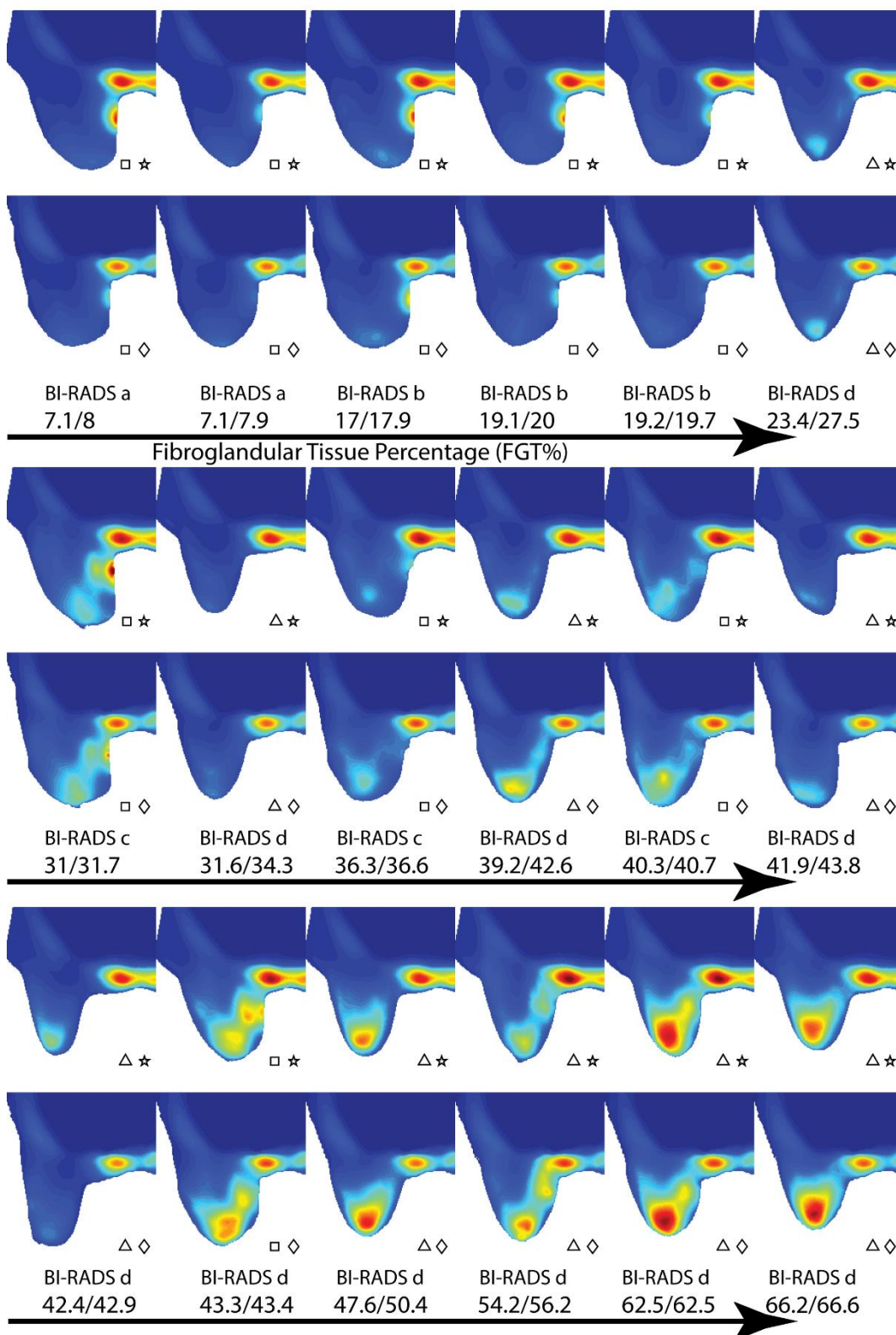


Figure B-6. Axial plots of temperature rise when tissue temperature reaches the steady-state in 7 T at mean $B_1^+ = 1.5 \mu\text{T}$ within tissue for 0.5-mm resolution breast models derived from the BI-RADS categorized CT (triangles) and MRI (squares) images fused with Ella (stars) and Hanako (diamonds). The same breast models from Ella (upper row) are down-sampled to fuse with Hanako (lower row). The FGT%, in ascending order, is quantified below the marker lines. The FGT% values on the left and right side of the forward slash correspond to Ella and Hanako breasts, respectively. All images are taken from the axial plane across the coil center in the same field of view.

Temperature Rise
0 0.03 0.06 (°C)

$|B_1^+|_{\text{mean}} = 1.5 \mu\text{T}$
FOV = 19 cm(H) x 17 cm(W)

★ Ella
◇ Hanako
□ MRI Breasts
△ CT Breasts



REFERENCES

1. Budinger TF, Bird MD, Frydman L, et al. Toward 20 T magnetic resonance for human brain studies: opportunities for discovery and neuroscience rationale. *Magn. Reson. Mater. Physics, Biol. Med.* 2016;29:617–639.
2. Yacoub E, Shmuel A, Pfeuffer J, et al. Imaging brain function in humans at 7 Tesla. *Magn. Reson. Med.* 2001;45:588–594 doi: 10.1002/mrm.1080.
3. Ertürk MA, Wu X, Eryaman Y, et al. Toward imaging the body at 10.5 tesla. *Magn. Reson. Med.* 2017;77:434–443 doi: 10.1002/mrm.26487.
4. Vaughan JT, Garwood M, Collins CM, et al. 7T vs. 4T: RF power, homogeneity, and signal-to-noise comparison in head images. *Magn. Reson. Med.* 2001 doi: 10.1002/mrm.1156.
5. Hetherington HP, Avdievich NI, Kuznetsov AM, Pan JW. RF shimming for spectroscopic localization in the human brain at 7 T. *Magn Reson Med* 2010;63:9–19 doi: 10.1002/mrm.22182.
6. Li X, Rispoli J V. Toward 7T breast MRI clinical study: safety assessment using simulation of heterogeneous breast models in RF exposure. *Magn Reson Med* 2019;81:1307–1321 doi: 10.1002/mrm.27395.
7. Siegel RL, Miller KD, Jemal A. Cancer statistics, 2016. *CA Cancer J Clin* 2016;66:7–30 doi: 10.3322/caac.21332.
8. Kuhl CK, Schrading S, Bieling HB, et al. MRI for diagnosis of pure ductal carcinoma in situ: a prospective observational study. *Lancet* 2007;370:485–492 doi: [https://doi.org/10.1016/S0140-6736\(07\)61232-X](https://doi.org/10.1016/S0140-6736(07)61232-X).
9. Kuhl CK, Strobil K, Bieling H, Leutner C, Schild HH, Schrading S. Supplemental Breast MR Imaging Screening of Women with Average Risk of Breast Cancer. *Radiology* 2017;283:361–370 doi: 10.1148/radiol.2016161444.
10. Saslow D, Boetes C, Burke W, et al. American Cancer Society guidelines for breast screening with MRI as an adjunct to mammography. *CA. Cancer J. Clin.* 2007;57:75–89 doi: 10.3322/canjclin.57.2.75.

11. Lee CH, Dershaw DD, Kopans D, et al. Breast cancer screening with imaging: recommendations from the Society of Breast Imaging and the ACR on the use of mammography, breast MRI, breast ultrasound, and other technologies for the detection of clinically occult breast cancer. *J. Am. Coll. Radiol.* 2010;7:18–27 doi: 10.1016/j.jacr.2009.09.022.
12. Mainiero MB, Lourenco A, Mahoney MC, et al. ACR Appropriateness Criteria Breast Cancer Screening. *J. Am. Coll. Radiol.* 2017;13:R45–R49 doi: 10.1016/j.jacr.2016.09.021.
13. Senkus E, Kyriakides S, Ohno S, et al. Primary breast cancer: ESMO Clinical Practice Guidelines for diagnosis, treatment and follow-up. *Ann. Oncol.* 2015;26:v8–v30.
14. Sardanelli F, Giuseppetti GM, Panizza P, et al. Sensitivity of MRI Versus Mammography for Detecting Foci of Multifocal, Multicentric Breast Cancer in Fatty and Dense Breasts Using the Whole-Breast Pathologic Examination as a Gold Standard. *Am. J. Roentgenol.* 2004;183:1149–1157 doi: 10.2214/ajr.183.4.1831149.
15. Checka CM, Chun JE, Schnabel FR, Lee J, Toth H. The Relationship of Mammographic Density and Age: Implications for Breast Cancer Screening. *Am. J. Roentgenol.* 2012;198:W292–W295 doi: 10.2214/AJR.10.6049.
16. Radiology AC of. American College of Radiology breast imaging reporting and data system. 2013.
17. Korteweg MA, Veldhuis WB, Visser F, et al. Feasibility of 7 Tesla breast magnetic resonance imaging determination of intrinsic sensitivity and high-resolution magnetic resonance imaging, diffusion-weighted imaging, and ¹H-magnetic resonance spectroscopy of breast cancer patients receiving neoadjuv. *Invest. Radiol.* 2011;46:370–376 doi: 10.1097/RLI.0b013e31820df706.
18. van de Bank BL, Voogt IJ, Italiaander M, et al. Ultra high spatial and temporal resolution breast imaging at 7T. *NMR Biomed* 2013;26:367–375 doi: 10.1002/nbm.2868.
19. Gruber S, Pinker K, Zaric O, et al. Dynamic contrast-enhanced magnetic resonance imaging of breast tumors at 3 and 7 T: a comparison. *Invest. Radiol.* 2014;49:354–362 doi: 10.1097/RLI.0000000000000034.
20. Center for Devices and Radiological Health. Criteria for Significant Risk Investigations of Magnetic Resonance Diagnostic Devices - Guidance for Industry and Food and Drug Administration Staff. Rockv. Dep. Heal. Hum. Serv. (US); 2014;Report No.

21. Technical committee 62 (Electrical equipment in medical practice), subcommittee 62B (Diagnostic imaging equipment). Medical electrical equipment-Part 2-33: Particular requirements for the basic safety and essential performance of magnetic resonance equipm.
22. Metzger GJ, Snyder C, Akgun C, Vaughan T, Ugurbil K, Van De Moortele PF. Local B1+ shimming for prostate imaging with transceiver arrays at 7T based on subject-dependent transmit phase measurements. *Magn. Reson. Med.* 2008;59:396–409 doi: 10.1002/mrm.21476.
23. Oezerdem C, Winter L, Graessl A, et al. 16-channel bow tie antenna transceiver array for cardiac MR at 7.0 tesla. *Magn. Reson. Med.* 2016 doi: 10.1002/mrm.25840.
24. Schmitter S, Schnell S, Uğurbil K, Markl M, Van de Moortele PF. Towards high-resolution 4D flow MRI in the human aorta using kt-GRAPPA and B1+ shimming at 7T. *J. Magn. Reson. Imaging* 2016 doi: 10.1002/jmri.25164.
25. Padormo F, Beqiri A, Hajnal J V., Malik SJ. Parallel transmission for ultrahigh-field imaging. *NMR Biomed.* 2016;29:1145–1161 doi: 10.1002/nbm.3313.
26. Guérin B, Gebhardt M, Serano P, et al. Comparison of simulated parallel transmit body arrays at 3 T using excitation uniformity, global SAR, local SAR, and power efficiency metrics. *Magn. Reson. Med.* 2015;73:1137–1150 doi: 10.1002/mrm.25243.
27. Adriany G, Van De Moortele PF, Ritter J, et al. A geometrically adjustable 16-channel transmit/receive transmission line array for improved RF efficiency and parallel imaging performance at 7 Tesla. *Magn. Reson. Med.* 2008 doi: 10.1002/mrm.21488.
28. Kozlov M, Turner R. Fast MRI coil analysis based on 3-D electromagnetic and RF circuit co-simulation. *J Magn Reson* 2009;200:147–152 doi: 10.1016/j.jmr.2009.06.005.
29. Zhang R, Xing Y, Nistler J, Wang J. Field and S-Parameter Simulation of Arbitrary Antenna Structure with Variable Lumped Elements. *Proc. ISMRM* 2009;17:3040.
30. Lemdiasov RA, Obi AA, Ludwig R. A numerical postprocessing procedure for analyzing radio frequency MRI coils. *Concepts Magn. Reson. Part A* 38A:133–147 doi: 10.1002/cmr.a.20217.
31. Beqiri A, Hand JW, Hajnal J V, Malik SJ. Comparison between simulated decoupling regimes for specific absorption rate prediction in parallel transmit MRI. *Magn Reson Med* 2015;74:1423–1434 doi: 10.1002/mrm.25504.

32. Restivo M, Raaijmakers A, van den Berg C, Luijten P, Hoogduin H. Improving peak local SAR prediction in parallel transmit using in situ S-matrix measurements. *Magn Reson Med* 2017;77:2040–2047 doi: 10.1002/mrm.26261.
33. Sadeghi-Tarakameh A, DelaBarre L, Lagore RL, et al. In vivo human head MRI at 10.5T: A radiofrequency safety study and preliminary imaging results. *Magn. Reson. Med.* 2019 doi: 10.1002/mrm.28093.
34. Teeuwisse WM, Brink WM, Haines KN, Webb AG. Simulations of high permittivity materials for 7 T neuroimaging and evaluation of a new barium titanate-based dielectric. *Magn. Reson. Med.* 2012 doi: 10.1002/mrm.24176.
35. van Gemert J, Brink W, Webb A, Remis R. High-permittivity pad design tool for 7T neuroimaging and 3T body imaging. *Magn. Reson. Med.* 2019 doi: 10.1002/mrm.27629.
36. Sica CT, Rupprecht S, Hou RJ, et al. Toward whole-cortex enhancement with an ultrahigh dielectric constant helmet at 3T. *Magn. Reson. Med.* 2020 doi: 10.1002/mrm.27962.
37. Liu W. RF Field Modeling for Double-Tuned Volume Coils. *eMagRes* doi: 10.1002/9780470034590.emrstm1159.
38. McDougall MP, Cheshkov S, Rispoli J, Malloy C, Dimitrov I, Wright SM. Quadrature transmit coil for breast imaging at 7 tesla using forced current excitation for improved homogeneity. *J Magn Reson Imaging* 2014;40:1165–1173 doi: 10.1002/jmri.24473.
39. Ibrahim TS, Tang L. Insight into RF power requirements and B1 field homogeneity for human MRI via rigorous FDTD approach. *J Magn Reson Imaging* 2007;25:1235–1247 doi: 10.1002/jmri.20919.
40. Chen C-N, Hoult DI. *Biomedical Magnetic Resonance Technology*.; 1989. doi: 10.1017/CBO9781107415324.004.
41. Shen J, Lowe I. RF Coil Design for NMR Imaging. . *Proc SMRM* p 1117-1118. 1985.
42. G. McKinnon ZW. Direct Capacitor Determination in FDTD Modeling of RF Coils. *ISMRM Proc.* 2003.
43. Taflove A, Hagness SC. *Computational electrodynamics: the finite-difference time-domain method*. Artech house; 2005.
44. Pozar DM. *Microwave engineering*. John Wiley & Sons; 2009.

45. Avdievich NI, Pan JW, Hetherington HP. Resonant inductive decoupling (RID) for transceiver arrays to compensate for both reactive and resistive components of the mutual impedance. *NMR Biomed* 2013;26:1547–1554 doi: 10.1002/nbm.2989.
46. Mainiero MB, Lourenco A, Mahoney MC, et al. ACR Appropriateness Criteria Breast Cancer Screening. *J Am Coll Radiol* 2013;10:11–14 doi: 10.1016/j.jacr.2012.09.036.
47. Senkus E, Kyriakides S, Ohno S, et al. Primary breast cancer: ESMO Clinical Practice Guidelines for diagnosis, treatment and follow-up. *Ann. Oncol.* 2015;26:v8–v30 doi: 10.1093/annonc/mdv298.
48. Morris EA, Lee CH, et al CCE. ACR BI-RADS® Magnetic Resonance Imaging. In: ACR BI-RADS® Atlas, Breast Imaging Reporting and Data System. Reston (VA): American College of Radiology. 2013;p.129;p.129.
49. Magnetic Resonance Section. Characterization of the Specific Absorption Rate (SAR) for Magnetic Resonance Imaging Systems. Rosslyn (VA): National Electrical Manufacturers Association; 2016. Report No. MS 8-2016.
50. Dimbylow PJ. FDTD calculations of the whole-body averaged SAR in an anatomically realistic voxel model of the human body from 1 MHz to 1 GHz. *Phys Med Biol* 1997;42:479–490 doi: <https://doi.org/10.1088/0031-9155/42/3/003>.
51. Collins CM, Smith MB. Calculations of B1 distribution, SNR, and SAR for a surface coil adjacent to an anatomically-accurate human body model. *Magn. Reson. Med.* 2001 doi: 10.1002/mrm.1092.
52. Hand JW. Modelling the interaction of electromagnetic fields (10 MHz-10 GHz) with the human body: methods and applications. *Phys Med Biol* 2008;53:R243-86 doi: 10.1088/0031-9155/53/16/r01.
53. Nyenhuis J. RF Device Safety and Compatibility. *eMagRes* 2010.
54. Wolf S, Diehl D, Gebhardt M, Mallow J, Speck O. SAR simulations for high-field MRI: how much detail, effort, and accuracy is needed? *Magn Reson Med* 2013;69:1157–1168 doi: 10.1002/mrm.24329.
55. Nagaoka T, Watanabe S, Sakurai K, et al. Development of realistic high-resolution whole-body voxel models of Japanese adult males and females of average height and weight, and application of models to radio-frequency electromagnetic-field dosimetry. *Phys. Med. Biol.* 2004;49:1–15 doi: 10.1088/0031-9155/49/1/001.

56. Dimbylow P. Resonance behaviour of whole-body averaged specific energy absorption rate (SAR) in the female voxel model, NAOMI. *Phys Med Biol* 2005;50:4053–4063 doi: 10.1088/0031-9155/50/17/009.
57. Liu W, Collins CM, Smith MB. Calculations of B1 Distribution, Specific Energy Absorption Rate, and Intrinsic Signal-to-Noise Ratio for a Body-Size Birdcage Coil Loaded with Different Human Subjects at 64 and 128 MHz. *Appl Magn Reson* 2005;29:5–18 doi: 10.1007/bf03166953.
58. Christ A, Kainz W, Hahn EG, et al. The Virtual Family--development of surface-based anatomical models of two adults and two children for dosimetric simulations. *Phys Med Biol* 2010;55:N23-38 doi: 10.1088/0031-9155/55/2/n01.
59. Khalkhali I, Mena I, Diggles L. Review of imaging techniques for the diagnosis of breast cancer: a new role of prone scintimammography using technetium-99m sestamibi. *Eur. J. Nucl. Med.* 1994;21:357–362 doi: 10.1007/bf00947973.
60. Hylton NM, Frankel SD. Imaging techniques for breast MR imaging. *Magn. Reson. Imaging Clin. N. Am.* 1994;2:511–525.
61. Orel SG, Schnall MD. MR imaging of the breast for the detection, diagnosis, and staging of breast cancer. *Radiology* 2001;220:13–30 doi: 10.1148/radiology.220.1.r01j13113.
62. Siegler P, Holloway CMB, Causer P, Thevathasan G, Plewes DB. Supine breast MRI. *J. Magn. Reson. Imaging* 2011;34:1212–1217 doi: 10.1002/jmri.22605.
63. Kim J, Krishnamurthy N, Santini T, et al. Experimental and numerical analysis of B1(+) field and SAR with a new transmit array design for 7T breast MRI. *J Magn Reson* 2016;269:55–64 doi: 10.1016/j.jmr.2016.04.012.
64. van der Velden TA, Italiaander M, van der Kemp WJM, et al. Radiofrequency configuration to facilitate bilateral breast 31P MR spectroscopic imaging and high-resolution MRI at 7 Tesla. *Magn. Reson. Med.* 2015;74:1803–1810 doi: 10.1002/mrm.25573.
65. Zhao H-K, Osher S, Fedkiw R. Fast surface reconstruction using the level set method. In: *Proceedings IEEE Workshop on Variational and Level Set Methods in Computer Vision*, Vancouver, BC, Canada. Vol. 21:330-338. ; 2001. pp. 194–201. doi: 10.1145/566654.566585.

66. Museth K, Breen DE, Whitaker RT, Barr AH. Level set surface editing operators. In: ACM Transactions on Graphics (TOG). Vol. 21. ACM; 2002. pp. 330–338. doi: 10.1145/566654.566585.
67. Osher S, Fedkiw R. Level set methods and dynamic implicit surfaces. Springer Science & Business Media; 2006.
68. Klomp DWJ, van de Bank BL, Raaijmakers A, et al. 31P MRSI and 1H MRS at 7 T: initial results in human breast cancer. NMR Biomed. 2011;24:1337–1342 doi: 10.1002/nbm.1696.
69. Cui J, Bosshard JC, Rispoli J V, et al. A Switched-Mode Breast Coil for 7 T MRI Using Forced-Current Excitation. IEEE Trans. Biomed. Eng. 2015;62:1777–1783 doi: 10.1109/TBME.2015.2403850.
70. Rispoli J V, Dimitrov IE, Cheshkov S, Malloy C, Wright SM, McDougall MP. Trap design and construction for high-power multinuclear magnetic resonance experiments. Concepts Magn. Reson. Part B Magn. Reson. Eng. 2016;46B:162–168 doi: 10.1002/cmr.b.21345.
71. Burfeindt MJ, Colgan TJ, Mays RO, et al. MRI-derived 3-D-printed breast phantom for microwave breast imaging validation. IEEE Antennas Wirel. Propag. Lett. 2012;11:1610–1613.
72. Erickson DW, Wells JR, Sturgeon GM, et al. Population of 224 realistic human subject-based computational breast phantoms. Med Phys 2016;43:23 doi: 10.1118/1.4937597.
73. Hasgall P, Neufeld E, Gosselin M, Klingensböck A, Kuster N. IT'IS Database for thermal and electromagnetic parameters of biological tissues. Version 2.4, July 30th, 2013. Zurich, Switz. IT'IS Found. [www. itis. ethz. ch/database](http://www.itis.ethz.ch/database) [Last accessed January 9, 2015] 2013.
74. Zastrow E, Davis SK, Lazebnik M, Kelcz F, Van Veen BD, Hagness SC. Development of anatomically realistic numerical breast phantoms with accurate dielectric properties for modeling microwave interactions with the human breast. IEEE Trans Biomed Eng 2008;55:2792–2800 doi: 10.1109/tbme.2008.2002130.
75. Soille P. Morphological image analysis: principles and applications. Springer Science & Business Media; 2013.
76. Li X, Mao X, Talavage T, Rispoli J. Bilateral Breast Phantoms for Fusion to Human Voxel Models for Specific Absorption Rate (SAR) Simulations. Proc. Intl. Soc. Mag. Reson. Med.:2643.

77. Li X, Rispoli J. Thermal and Specific Absorption Rate Simulation of Heterogeneous Breast Models in The Prone Position Fused with Two Human Whole-Body Models. ISMRM Work. Ensuring RF Saf. MRI, McLean, VA, 2017.
78. Goldman R. Curvature formulas for implicit curves and surfaces. *Comput. Aided Geom. Des.* 2005;22:632–658 doi: 10.1016/j.cagd.2005.06.005.
79. Jurgens TG, Taflove A, Umashankar K, Moore TG. Finite-difference time-domain modeling of curved surfaces (EM scattering). *IEEE Trans. Antennas Propag.* 1992;40:357–366 doi: 10.1109/8.138836.
80. IEEE International Committee on Electromagnetic Safety (Standards Coordinating Committee 28 on Non-Ionizing Radiation). C95.3-2002(R2008) - IEEE Recommended Practice for Measurements and Computations of Radio Frequency Electromagnetic Fields With Respect . 2008 doi: 10.1109/IEEESTD.2002.94226.
81. Pennes HH. Analysis of tissue and arterial blood temperatures in the resting human forearm. *J Appl Physiol* 1948;1:93–122 doi: 10.1152/jappl.1948.1.2.93.
82. Collins CM, Liu W, Wang J, et al. Temperature and SAR calculations for a human head within volume and surface coils at 64 and 300 MHz. *J. Magn. Reson. Imaging* 2004;19:650–656 doi: 10.1002/jmri.20041.
83. Vaughan JT, Griffiths JR. RF coils for MRI. John Wiley & Sons; 2012.
84. Hu L, Gupta A, Gore JP, Xu LX. Effect of forced convection on the skin thermal expression of breast cancer. *Trans. Soc. Mech. Eng. J. Biomech. Eng.* 2004;126:204–211 doi: 10.1115/1.1688779.
85. Li X, Rispoli J. Breast MRI Safety: Simulation of RF Coils with Breast Phantoms Fused to a Human Model. *Proc. 2017 BMES/FDA Front. Med. Devices Conf. Park. Maryland*, 2017.
86. Chen X, Li X, Kara D, et al. Improving breast imaging B1+ homogeneity with B1 shimming at 1.5T: a modeling study. *Proc. Int. Soc. Mag. Reson Med.(Annu. Meet. Abstr.)* 2018;1300.
87. Lee J, Chen S, Reece GP, Crosby MA, Beahm EK, Markey MK. A novel quantitative measure of breast curvature based on catenary. *IEEE Trans. Biomed. Eng.* 2012;59:1115–1124 doi: 10.1109/TBME.2012.2184541.
88. Kawale MM, Reece GP, Crosby MA, et al. Automated identification of fiducial points on 3D Torso images. *Biomed. Eng. Comput. Biol.* 2013;5:57 doi: <https://doi.org/10.4137/BECB.S11800>.

89. Sun CS, Markey MK, Merchant FA, Ravi-Chandar K, Fingeret MC, Reece GP. Biomedical Optics & Medical Imaging 3D computer technology addresses body-image issues of breast reconstruction. SPIE Newsroom 2013 doi: 10.1117/2.1201307.005016.
90. Vaughan JT, Snyder CJ, Delabarre LJ, et al. Whole-body imaging at 7T: Preliminary results. *Magn. Reson. Med.* 2009;61:244–248 doi: 10.1002/mrm.21751.
91. Barry RL, Vannesjo SJ, By S, Gore JC, Smith SA. Spinal cord MRI at 7T. *Neuroimage* 2018 doi: 10.1016/j.neuroimage.2017.07.003.
92. Rivera D, Kalleveen I, Laarhoven H Van, Klomp D, Kemp W Van Der. Inherently decoupled 1 H antennas and 31 P loops for metabolic imaging of liver metastasis at 7 T. 2020:1–10 doi: 10.1002/nbm.4221.
93. Vaughan JT, Hetherington HP, Otu JO, Pan JW, Pohost GM. High frequency volume coils for clinical NMR imaging and spectroscopy. *Magn. Reson. Med.* 1994;32:206–218 doi: 10.1002/mrm.1910320209.
94. Collins CM, Li S, Smith MB. SAR and B1 field distributions in a heterogeneous human head model within a birdcage coil. *Magn. Reson. Med.* 1998 doi: 10.1002/mrm.1910400610.
95. Mikhail Kozlov Nikolai Avdievich RT. Investigation of the decoupling between MRI array elements. *Proc. 43rd Eur. Microw. Conf.*
96. Gabriel C, Gabriel S, Corthout E. The dielectric properties of biological tissues: I. Literature survey. *Phys. Med. Biol.* 1996 doi: 10.1088/0031-9155/41/11/001.
97. Epstein BR, Foster KR. Anisotropy in the dielectric properties of skeletal muscle. *Med. Biol. Eng. Comput.* 1983 doi: 10.1007/BF02446406.
98. Schmitter S, Wu X, Adriany G, Auerbach EJ, Ugurbil K, Van De Moortele PF. Cerebral TOF angiography at 7T: Impact of B1+ shimming with a 16-channel transceiver array. *Magn. Reson. Med.* 2014;71:966–977 doi: 10.1002/mrm.24749.
99. Ibrahim TS, Lee R, Baertlein BA, Abduljalil AM, Zhu H, Robitaille PML. Effect of RF coil excitation on field inhomogeneity at ultra high fields: A field optimized TEM resonator. *Magn. Reson. Imaging* 2001;19:1339–1347 doi: 10.1016/S0730-725X(01)00404-0.
100. Avdievich NI, Oh S, Hetherington HP, Collins CM. Improved homogeneity of the transmit field by simultaneous transmission with phased array and volume coil. *J. Magn. Reson. Imaging* 2010 doi: 10.1002/jmri.22257.

101. Adriany G, Radder J, Tavaf N, et al. Evaluation of a 16-channel transmitter for head imaging at 10.5T. In: Proceedings of the 2019 21st International Conference on Electromagnetics in Advanced Applications, ICEAA 2019. ; 2019. doi: 10.1109/ICEAA.2019.8879131.
102. Hoffmann J, Shajan G, Scheffler K, Pohmann R. Numerical and experimental evaluation of RF shimming in the human brain at 9.4 T using a dual-row transmit array. *Magn. Reson. Mater. Physics, Biol. Med.* 2014 doi: 10.1007/s10334-013-0419-y.
103. Avdievich NI, Ruhm L, Dorst J, Scheffler K, Korzowski A, Henning A. Double-tuned 31P/1H human head array with high performance at both frequencies for spectroscopic imaging at 9.4T. *Magn. Reson. Med.* 2020 doi: 10.1002/mrm.28176.
104. HP Hetherington JW Pan NIA. Multiplexed RF Transmission for Transceiver Arrays at 7T. 19th ISMRM Proc. 2011.
105. NI Avdievich HP Hetherington JWP. Improved Longitudinal Coverage for Human Brain at 7T: A 16 Element Transceiver Array. 19th ISMRM proceedings 2011;page 328.
106. Avdievich NI. Transceiver-phased arrays for human brain studies at 7 T. *Appl. Magn. Reson.* 2011;41:483–506.
107. Alt S, Müller M, Umathum R, et al. Coaxial waveguide MRI. *Magn. Reson. Med.* 2012 doi: 10.1002/mrm.23069.
108. Nagaoka T, Watanabe S, Sakurai K, et al. Development of realistic high-resolution whole-body voxel models of Japanese adult males and females of average height and weight, and application of models to radio-frequency electromagnetic-field dosimetry. *Phys Med Biol* 2004;49:1–15 doi: <https://doi.org/10.1088/0031-9155/49/1/001>.
109. Christ A, Kainz W, Hahn EG, et al. The Virtual Family--development of surface-based anatomical models of two adults and two children for dosimetric simulations. *Phys Med Biol* 2010;55:N23-38 doi: 10.1088/0031-9155/55/2/n01.
110. Gosselin M-C, Neufeld E, Moser H, et al. Development of a new generation of high-resolution anatomical models for medical device evaluation: the Virtual Population 3.0. *Phys. Med. Biol.* 2014;59:5287.
111. Zelinka I. SOMA—Self-organizing Migrating Algorithm. In: *Studies in Computational Intelligence.* ; 2016. doi: 10.1007/978-3-319-28161-2_1.
112. Bouman CA. Model Based Image Processing. 2019 [Online] Available:<https://engineering.purdue.edu/~bouman/publications/pdf/MBIP-book.pdf>.

113. Mao W, Smith MB, Collins CM. Exploring the limits of RF shimming for high-field MRI of the human head. *Magn. Reson. Med.* 2006;56:918–922 doi: 10.1002/mrm.21013.
114. Ullmann P, Junge S, Wick M, Seifert F, Ruhm W, Hennig J. Experimental analysis of parallel excitation using dedicated coil setups and simultaneous RF transmission on multiple channels. *Magn. Reson. Med.* 2005;54:994–1001 doi: 10.1002/mrm.20646.
115. Saekho S, Boada FE, Noll DC, Stenger VA. Small tip angle three-dimensional tailored radiofrequency slab-select pulse for reduced B1 inhomogeneity at 3 T. *Magn. Reson. Med.* 2005;53:479–484 doi: 10.1002/mrm.20358.
116. Grissom W, Yip CY, Zhang Z, Stenger VA, Fessler JA, Noll DC. Spatial domain method for the design of RF pulses in multicoil parallel excitation. *Magn Reson Med* 2006;56:620–629 doi: 10.1002/mrm.20978.
117. Eichfelder G, Gebhardt M. Local specific absorption rate control for parallel transmission by virtual observation points. *Magn Reson Med* 2011;66:1468–1476 doi: 10.1002/mrm.22927.
118. Homann H, Graesslin I, Eggers H, et al. Local SAR management by RF shimming: a simulation study with multiple human body models. *MAGMA* 2012;25:193–204 doi: 10.1007/s10334-011-0281-8.
119. Zhu Y, Alon L, Deniz CM, Brown R, Sodickson DK. System and SAR characterization in parallel RF transmission. *Magn. Reson. Med.* 2012 doi: 10.1002/mrm.23126.